

**Best Available  
Copy  
for all Pictures**

AD-768 794

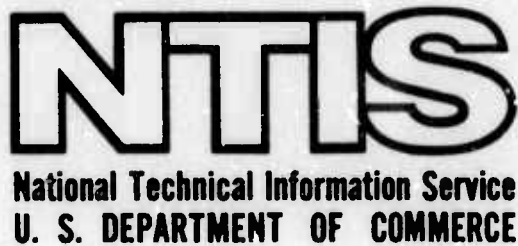
NEW METHODS OF SYNTHESIS OF MATERIALS. (I)  
THE PROPERTIES OF RARE EARTH METALS AND ALLOYS. (II)

CALIFORNIA UNIVERSITY

PREPARED FOR  
ADVANCED RESEARCH PROJECTS AGENCY

SEPTEMBER 1973

DISTRIBUTED BY:



AD-768794  
CONFIDENTIAL

DOCUMENT CONTROL DATA - R & D

Security classification of title, body of abstract and indexing annotation must be entered when the overall report is cl. classified)

1. ORIGINATING ACTIVITY (Corporate author) <b>School of Engineering &amp; Applied Science University of California at Los Angeles Los Angeles, California 90024</b>		2a. REPORT SECURITY CLASSIFICATION <b>Unclassified</b>
2b. GROUP		
3. REPORT TITLE <b>I. NEW METHODS OF SYNTHESIS OF MATERIALS II. THE PROPERTIES OF RARE EARTH METALS AND ALLOYS</b>		
4. DESCRIPTIVE NOTES (Type of report and inclusive dates) <b>Semi-Annual Technical Report,</b>		
5. AUTHOR(S) (First name, middle initial, last name) <b>I. R. F. Bunshah II. D. L. Douglass</b>		
6. REPORT DATE <b>March 1972</b>	7a. TOTAL NO. OF PAGES <b>102</b>	7b. NO. OF REFS
8. CONTRACT OR GRANT NO. <b>AO #1643</b>	9a. ORIGINATOR'S REPORT NUMBER(S)	
b. PROJECT NO.  c.  d.	9b. OTHER REPORT NO(S) (Any other numbers that may be assigned this report)	
10. DISTRIBUTION STATEMENT <b>Distribution of this document is unlimited</b>		
11. SUPPLEMENTARY NOTES	12. SPONSORING MILITARY ACTIVITY	
13. ABSTRACT Two major areas of effort are encompassed: I. New Techniques for the Synthesis of Metals and Alloys The high rate physical vapor deposition (HRPVD) process is to be used for the following: 1. Preparation and characterization of Ni and Ni-20Cr alloy sheet. 2. Synthesis of compounds $Y_2O_3$ , TiC, $Si_3N_4$ by reactive evaporation and their characterization. 3. Dispersion strengthened alloys. Ni-20Cr- $Y_2O_3$ , Ni-20Cr-TiC and Ti- $Y_2O_3$ . This report describes: 1. The evaporation of a Ni-20Cr alloy from a single rod fed electron beam source. 2. The effect of substrate temperature on the structure and properties of TiC prepared by Activated Reactive Evaporation.  II. The Properties of Rare Earth Metals and Alloys The oxidation behavior of $Ni_3Al$ and $Ni_3Al-0.5Y$ has been studied at $1200^{\circ}C$ in air by thermogravimetric and x-ray analyses. The presence of yttrium has little effect on the oxidation kinetics but markedly reduces spalling of the film during cooling. The effect of preoxidation has also been studied.		

Reproduced by  
**NATIONAL TECHNICAL  
INFORMATION SERVICE**  
U.S. Department of Commerce  
Springfield VA 22151

KEY WORDS	LINK A		LINK B		LINK C	
	ROLE	WT	ROLE	WT	ROLE	WT
Activated reactive evaporation Argon Carbides Condensation Deposit Evaporation Evaporation variables Gadolinium Gas scattering evaporation High Rate Physical Vapor Deposition Process Lanthanum Lattice parameter Microhardness Nichrome Nickel Nitrides Oxidation Oxides Oxidation mechanism Rare-earth additions Reactive evaporation Refractory carbides Scale formation Silicon nitride-Si <sub>3</sub> N <sub>4</sub> Substrate Synthesis of Materials Thickness distribution Titanium carbide Yttria-Y <sub>2</sub> O <sub>3</sub> Yttrium						

SEMI-ANNUAL TECHNICAL REPORT NO. 6

I. New Techniques for the Synthesis of Metals and Alloys  
(Principal Investigator - Professor R.F. Bunshah)

II. The Properties of Rare Earth Metals and Alloys  
(Principal Investigator - Professor D.L. Douglass)  
The Oxidation Mechanism of Ni<sub>3</sub>Al Containing Yttrium  
(John D. Kuenzly)

Sponsor: The Advanced Research Projects Agency

Grant No.: DAHC 15-70-G-15

ARPA Order No.: AO 1643

Effective Date: July 1, 1970

Contract Expiration Date: June 30, 1973

Amount of Contract: \$298,398

Classification: Un-classified

This research was sponsored by the Advanced Research Projects Agency  
of the Department of Defense under Contract No. DAHC 15-70G-15

Materials Department  
School of Engineering and Applied Science  
University of California  
Los Angeles, California

•••  
///

## TABLE OF CONTENTS

	Page
INTRODUCTION . . . . .	1
PART I	
New Techniques for the Synthesis of Metals and Alloys (Tasks I, II, III)	
I. Background . . . . .	2
II. Scope of Work and Progress . . . . .	4
III. Future Work . . . . .	8
IV. Personnel . . . . .	9
APPENDIX I . . . . .	13

## PART II

### Properties of Rare-Earth Metals and Alloys (Task IV)

I. Introduction . . . . .	37
II. Experimental Procedure . . . . .	37
III. Results . . . . .	40
IV. Discussion . . . . .	67
V. Conclusions . . . . .	89

## INTRODUCTION

This report describes research activities on ARPA Grant No. AO 1643.

The scope of the work is divided into two major areas of effort and further subdivided into four tasks as shown below:

1. New Techniques for the Synthesis of Metals and Alloys - Tasks I, II, and III. (Professor R.F. Bunshah - Principal Investigator)
2. The Properties of Rare Earth Metals and Alloys - Task IV  
(Professor D. L. Douglass - Principal Investigator)

In the following, progress on Tasks I, II and III is reported.

Task IV has been completed and the final report is published in Part II of this report.

PART I

NEW TECHNIQUES FOR THE SYNTHESIS OF METALS AND ALLOYS  
(TASKS I, II, AND III)

R. F. Bunshah

## ABSTRACT

### I. New Techniques for the Synthesis of Metals and Alloys

The high rate physical vapor deposition (HRPVD) process is to be used for the following:

1. Preparation and characterization of Ni and Ni-20Cr alloy sheet.
2. Synthesis of compounds  $Y_2O_3$ , TiC,  $Si_3N_4$  by reactive evaporation and their characterization.
3. Dispersion strengthened alloys, Ni-20Cr- $Y_2O_3$ , Ni20Cr-TiC and Ti- $Y_2O_3$ .

This report describes:

- (1) Preparation of Nickel foil by HRPVD techniques and evaluation of its properties.
- (2) Experiments on high rate deposition of  $Y_2O_3$ , TiC,  $Si_3N_4$  by direct evaporation and of  $Y_2O_3$  and  $Si_3N_4$  by reactive evaporation and activated reactive evaporation.

## I. Background

High rate physical vapor deposition (HRPVD) techniques<sup>(1-8)</sup> are to be used to prepare metallic alloys, ceramics, and metal-ceramic mixtures (dispersion strengthened alloys). The method consists of evaporation of metals, alloys and ceramics contained in water cooled crucibles using high power electron beams. The process is carried out in a high vacuum environment. The use of high power electron beams makes it possible to produce very high evaporation rates. The vapors are collected on heated metallic substrates to produce full density deposits at high deposition rates.

There are three tasks in this section:

Task I: The preparation and characterization of nickel and Ni-20Cr alloy sheet by the high rate physical vapor deposition process.

Task II: Synthesis and characterization of compounds by Reactive Evaporation. The compounds to be prepared are  $Y_2O_3$ , TiC and  $Si_3N_4$ .

Task III: Dispersion strengthened alloys produced by HRPVD Process, and their characterization. The specific alloys to be studied are:

- A. Ni-20Cr- $Y_2O_3$
- B. Ni-20Cr-TiC
- C. Ti- $Y_2O_3$

Single source and two source evaporation methods will be used to produce these alloys.

The HRPVD process has several attractive features:

- A. Simple, full density shapes (sheet, foil, tubing) can be produced at high deposition rates, 0.001" per minute thickness increment thus making it an economically viable process.
- B. Metals and alloys of high purity can be produced.

C. Very fine grain sizes ( $1\mu$  grain diameter or smaller) can be produced by controlling substrate temperature. Grain size refinement is produced by lowering the condensation temperature.

D. An alloy deposit may be produced from a single rod fed source. This occurs because the molten pool at the top of the rod is about  $1/4"$  deep only. The vapor composition is the same as that of the solid rod being fed into the molten pool. At equilibrium, the composition of the molten pool differs from that of the vapor or the solid feed. It is richer in those components having a low vapor pressure. The composition of the vapor is the product of the vapor pressure times the mole fraction of the component. For example, a Ti-6Al-4V alloy deposit where the differences in vapor pressure of Al and V are a factor of 5,000 at  $1600^{\circ}\text{C}$  can be produced by evaporation from a single source. The feed-rod is Ti-6Al-4V and the molten pool is much richer in V than in Al.

E. Two or more sources can be used to simultaneously deposit on the same substrate thus conferring the ability to produce complex alloys. For example, an alloy with a 2 or 3 component solid solution matrix may be evaporated from one source and another metal or ceramic for the dispersed phase from another source. The dispersion size and spacing should be very fine since the deposition is occurring from the vapor phase.

The unique feature of this process is that all of the above benefits can be obtained simultaneously.

It should be noted that the condensation temperature is a very important process variable. Bunshah and Juntz<sup>(8)</sup> found that for titanium, as the deposition temperature is lowered the grain size of the fully dense deposit becomes finer. At very low temperatures ( $\sim 25\%$  of the melting point) the deposit has less than full density. Since a fine grain sized

microstructure represents an optimum condition of strength and toughness in a material, the importance of control over the deposition temperature becomes obvious.

II. Scope of Work and Progress in Reporting Period (September 1, 1972 - February 28, 1973)

The main tasks on this contract are the preparation and testing of the various alloys, ceramics and dispersion strengthened alloys as outlined in Section I above. Very essential to the preparation of suitable test specimens are two other factors:

- A. Design of the apparatus for high rate physical vapor deposition.
- B. Theoretical calculation of the thickness distribution and temperature distribution of the deposited material which is in this case in the form of a sheet.

Both of these tasks are essential preliminaries to the main scope of work. They were completed and described in semi-annual technical report No. 1. (9)

Two papers based on item B above have been published. (10,11)

A NEW process for the synthesis and high rate deposition of compounds was developed. (12) The process is called Activated Reactive Evaporation and two papers (13,14) have been presented and accepted for publication.

During this period several activities were carried out. They are described below.

1. Experimental Variables in the Gas Scattering Plating Process

The evaporation process is a line-of-sight process since the mean free path of the vapor atoms is longer than the source to substrate distance. In many cases, it is desirable to deposit materials on all sides of the object. This becomes possible if the mean-free path of the vapor

atoms is made very small (a few mm) by carrying out the evaporation process in a relatively high pressure (1 to 100 microns) on an inert or reactive gas. This is called the Gas Scattering Process. The object of this part of the investigation was to explore the effect of Experimental Variables in the Gas Scattering Process. This study consists of two parts. The first part was concerned with the efficiency of the HRPVD process in the presence of a gas and was presented as a paper at the International Vacuum Metallurgy Conference, Tokyo, June 1973. It is included as Appendix I to Part I of this report. The second part, now in progress, is concerned with the effect of the gas on the morphology of the deposits. This will be reported in detail in the next report.

## 2. Deposition of Ni-20Cr Alloy

This work is almost complete and the results are excellent. Table I gives the deposit morphology as a function of deposition temperature. It is seen that the Ni-20Cr deposits display all the three morphologies and the transition temperature agrees with the proposed model advanced by Movchan and Demchishin<sup>(15)</sup> and previously confirmed for Ni, Ti, W, Al<sub>2</sub>O<sub>3</sub>, ZrO<sub>2</sub>, TiC.<sup>(16)</sup> Table II lists the tensile data for the deposited alloy. It is seen that the alloy exhibits good strength and ductility. Furthermore, the yield strength increases markedly with decreasing grain size and a plot of yield strength vs. (grain size)<sup>-1/2</sup> is linear, thus obeying the Hall-Petch relationship. From all of this data, it may be concluded that deposits of Ni-20Cr alloy produced by HRPVD techniques are indeed engineering materials. A comparison with cast, rolled and annealed material is being carried out and a full statement on this work will be issued with the next report.

Table INi-20Cr Tensile Properties

Sample	Method of Preparation	Grain Size (d) x 10 <sup>-3</sup> inch	Yield Stress Ksi	UTS Ksi	% Elonga- tion	% Red in area	d <sup>-1/2</sup> * (in) <sup>-1/2</sup>	Substrate Temperature °F
B-17	Deposited	0.51	48.21	76.0	26.4	27.3	44.2	1740°F
B-18								
B-13	Deposited	0.102	82.12	110.2	21.3	26.1	99.5	1400
B-14								
B-15	Deposited	0.0725	107.12	124.3	18.7	19.5	117.0	1200
B-16								
B-19	Deposited	0.020	171.45	174.7	6.25	8.0	222.0	800
B-20								

\* d is grain diameter

\*\* from Mechanical Properties of Metals and Alloys, circular C47, U.S. Department of Commerce 1943.

Table II  
Deposit Morphology as a Function of Temperature

Sample	Deposition Temperature °F	Deposition Temperature °K	Morphology
B-17	1740	1223	Equiaxed
B-18			Zone 3
B-13	1400	1033	Equiaxed
B-14			Zone 3
B-15	1200	928	In transition
B-16			between Zone 2 and Zone 3
B-19	800	698	Columnar
B-20			Zone 2

Morphology Zone Boundary Temperatures.

(Zone 1 - domed structure, Zone 2 - columnar, Zone 3 - Equiaxed)

$$\begin{aligned} \text{Melting Point of Ni-Cr} &= 1400^\circ\text{C} \\ &= 1673^\circ\text{K} \end{aligned}$$

$$\begin{aligned} \text{Zone 1} \rightarrow \text{Zone 2 at } T_1 &= 0.3 T_m \text{ (calculated)*} \\ &= 0.3 \times 1673 = \underline{\underline{502^\circ\text{K}}} \end{aligned}$$

$$\begin{aligned} \text{Zone 2} \rightarrow \text{Zone 3 at } T_2 &= 0.45 T_m \text{ (calculated)*} \\ &= 0.45 \times 1673 = \underline{\underline{750^\circ\text{K}}} \end{aligned}$$

\* Ref. B. Movchan and M. Demchishin, Phys. Metal. Metallov. 28, #4, 653 (1969).

### 3. Basic Study of the Activated Reactive Evaporation Process

The Activated Reactive Evaporation Process was developed in 1971 on this contract (Semi-Annual Progress Report No. 2). The process as well as the results of the work on TiC deposition were published earlier.<sup>13,14</sup> Additional work has been undertaken to attempt to understand the detailed mechanisms occurring during the process, using Langmuir probe measurements to supplement earlier X-ray and metallographic studies. The experimental work is nearly finished and a full statement will be made in the next semi-annual report.

### 4. Synthesis of Compounds

#### a) Effect of Impurities on the Lattice Parameter and Microhardness of TiC

This study is currently in progress. Its results will be relevant to other compounds synthesized and studied on this contract.

#### b) $\text{Y}_2\text{O}_3$ Synthesis

In the previous Semi-Annual Progress Report No. 5 (UCLA Eng-7328, March 1973), the data on the synthesis of  $\text{Y}_2\text{O}_3$  did not show a consistent pattern with change in experimental variables. Quite often the presence of Y in  $\text{Y}_2\text{O}_3$  was noticed from the X-ray diffraction analysis of the deposit. Microstructural examination was carried out and revealed gross areas of Y in these  $\text{Y}_2\text{O}_3$  deposits. It appears that "spitting" from the pool transfers minute droplets of Y to the  $\text{Y}_2\text{O}_3$  deposit and obviates the fear that the reaction  $2\text{Y} + \frac{3}{2}\text{O}_2 \rightarrow \text{Y}_2\text{O}_3$  was incomplete. Further work on synthesis and mechanical property determination of  $\text{Y}_2\text{O}_3$  deposits is now in progress.

## III. Future Work

In the next half-year period, the following work is scoped.

- A. Completion of the work on deposition of Ni and Ni-20Cr alloy sheets and a study of their structure and properties.

- B. Continuation of the work on the synthesis and testing of  $Y_2O_3$ , TiC and  $Si_3N_4$  by reactive evaporation and activated reactive evaporation.
- C. Initiation of the work on production of Ni-20Cr alloys containing dispersed phases by HRPVD processes from two evaporation sources.
- D. Completion of the work on basic study of the ARE process.

#### IV. Personnel

The following personnel have been working on this project in this reporting period.

Principal Investigator - Professor R. F. Bunshah

Post Doctoral Fellow: Dr. Harry A. Beale

Graduate Students: Mr. Rao Nimmagadda, Mr. Neil Kane and Mr. N. Agarwal

Technician: Mr. Fred Weiler

## REFERENCES

1. Bunshah, R.F., "Superpurification of Metals by Vacuum Distillation: A Theoretical Study," Trans. Vac. Met. Conf., 1963, AVS, 121.
2. Bunshah, R.F., and Juntz, R.S., "Purification of Beryllium by Crucible Free Melting and Distillation Process," in *Beryllium Technology*, Gordon and Breach, 1964, 1.
3. Bunshah, R.F., "Impurity Removal by Distillation of Beryllium from the Solid State," *Proceedings, Int'l. Conf. on Beryllium*, Grenoble, France, 1965, Presses Universitaires de France, 108 Blvd. St. Germain, Paris, 6, 63.
4. Bunshah, R.F., and Juntz, R.S., "The Purification of Beryllium by Vacuum Melting followed by Vacuum Distillation in an Electron Beam Furnace with Simultaneous deposition of Sheet," Trans. Vac. Met. Conf., 1966, AVS, 209.
5. Bunshah, R.F., "The Effect of Purification on Some Mechanical Properties of Beryllium," *Metals Engineering Quarterly*, Nov. 1964, 8.
6. Bunshah, R.F., and Juntz, R.S., "Electron Beam Distillation Furnace for Reactive Metals: Design Considerations and Operating Experience," Trans. Vac. Met. Conf., 1965, AVS, 200.
7. Bunshah, R.F. and Juntz, R.S., "Design Considerations for the Production of Massive Deposits of Alloys by Evaporation from Multiple Electron Beam Heated Sources," Trans. Vac. Met. Conf., 1967, AVS, 799.
8. Bunshah, R.F., and Juntz, R.S., "Influence of Condensation Temperature on Microstructure and Mechanical Properties of Titanium Sheet," Met. Trans., 4, 21 (1973).
9. Bunshah, R.F., and Douglass, D.L., Technical Report - UCLA-ENG-7112, March, 1971.
10. Nimmagadda, R. and Bunshah, R.F., J. Vac. Sci. and Tech., 8, VM85 (1971).
11. Chow, R., and Bunshah, R.F., J. Vac. Sci. and Tech., 8, VM73 (1971).
12. Bunshah, R.F. and Douglass, D.L., Technical Report - UCLA-ENG-7227, April 1972.
13. Bunshah, R.F. and Raghuram, A.C., "The Activated Reactive Evaporation Process," J. Vac. Sci. and Tech., 9, 1335 (1972).
14. Raghuram, A.C. and Bunshah, R.F., "The Influence of Substrate Temperature on the Structure of Titanium Carbide produced by Activated Reactive Evaporation," J. Vac. Sci. and Tech., 9, 1389 (1972).

15. Movchan B.A. and Demchishin, A.V., Fiz. Metal. Metalloved. 28, #4, 653 (1969).
16. Bunshah, R.F., "Physical Vapor Deposition of Metals, Alloys and Compounds," to be published, Proc. Fourth International Conference on Vacuum Metallurgy, Iron & Steel Institute of Japan, 1973.

APPENDIX I

**Evaporation Variables in Gas Scattering  
Plating Processes**

H.A. Beale - Postdoctoral Fellow

F. Weiler - Engineering Technician

R.F. Bunshah - Professor of Engineering

Materials Department  
6532 Boelter Hall  
University of California  
Los Angeles, California USA

### Synopsis

The effect of the presence of a gas during physical vapor deposition experiments using an electron beam heated source was studied. Some of the parameters studied are reactive vs. non-reactive gases (including varying the process to include activated reactive evaporation; gas pressure; condensation rate vs. evaporation; the efficiency of plating on the back side of the substrate, i.e., non-line-of-sight from the evaporant source; and deviations from the cosine law distribution vs. gas type and pressure. The results show greater plating efficiencies with reactive gases than non-reactive gases at similar pressures. As expected, when the pressure is increased to high values ( $> 50\mu$ ), the process efficiencies decrease. The efficiency for non-line-of-sight plating was found to depend primarily upon the atomic mass of the gas and secondly upon the gas pressure.

There appears to be very little information presented in the literature concerning the effects of gas scattering during physical vapor deposition (PVD).<sup>(1)</sup> The benefit of gas scattering during ion-plating has been noted,<sup>(2)</sup> but the credit for non-line-of-sight coating during ion-plating is usually attributed to the presence of the strong electric field required for the ion-plating process per se.<sup>(3-4)</sup> Other investigators have taken advantage of the principle of gas scattering of particles of atomic dimensions to obtain spit-free deposits.<sup>(5)</sup> It is the purpose of this investigation to study the experimental variables in gas scattering in a more complete manner than previously studied.

To observe just the effects of gas scattering, it was necessary to eliminate the ion-plating and sputtering processes from the study, since, in these processes, the gas is being acted upon by a strong electric field. This investigation was therefore limited to studying those PVD processes in which the gas is not acted upon at all by an electric field or only by a weak electric field. The processes involved in this study are:

1. Gas scattering evaporation (GSE). In this process the act of evaporation occurs in the presence of an inert gas. The composition of the deposit is essentially the same as the evaporant source.
2. Reactive evaporation (RE). In the simplest form of

There appears to be very little information presented in the literature concerning the effects of gas scattering during physical vapor deposition (PVD).<sup>(1)</sup> The benefit of gas scattering during ion-plating has been noted,<sup>(2)</sup> but the credit for non-line-of-sight coating during ion-plating is usually attributed to the presence of the strong electric field required for the ion-plating process per se.<sup>(3-4)</sup> Other investigators have taken advantage of the principle of gas scattering of particles of atomic dimensions to obtain spit-free deposits.<sup>(5)</sup> It is the purpose of this investigation to study the experimental variables in gas scattering in a more complete manner than previously studied.

To observe just the effects of gas scattering, it was necessary to eliminate the ion-plating and sputtering processes from the study, since, in these processes, the gas is being acted upon by a strong electric field. This investigation was therefore limited to studying those PVD processes in which the gas is not acted upon at all by an electric field or only by a weak electric field. The processes involved in this study are:

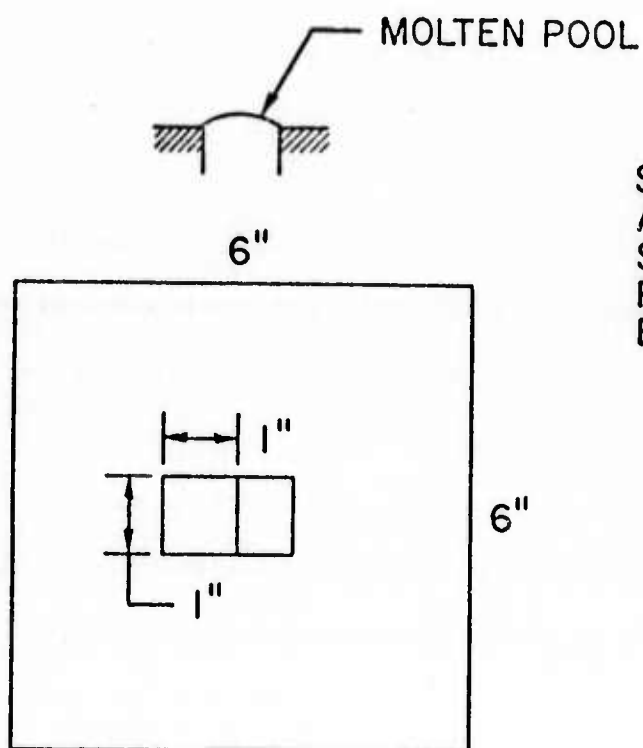
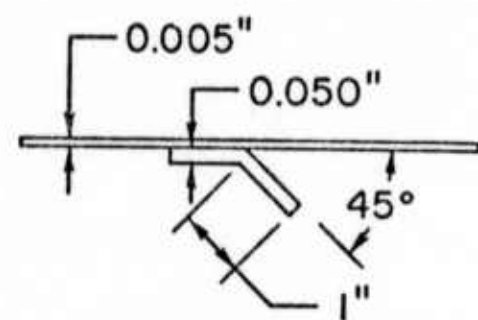
1. Gas scattering evaporation (GSE). In this process the act of evaporation occurs in the presence of an inert gas. The composition of the deposit is essentially the same as the evaporant source.
2. Reactive evaporation (RE). In the simplest form of

this process, an element is evaporated in the presence of a reactive elemental gas. The deposit is a compound formed between the two species.

3. Activated reactive evaporation (ARE).<sup>(6)</sup> This process is similar to the RE process except that here one or both of the reactants are activated, i.e., ionized to form a plasma.

The obvious distinction between GSE and RE occurs when the only gas present, other than the evaporant flux, is an inert gas. It is also possible to employ the ARE process configuration with only an inert gas present, or with no gas, other than the evaporant flux.

The experiments were performed using an electron beam heated, 1.0 in. diameter rod fed source. The electron gun was a standard 10 kv, 270° deflected beam type. The beam current used to melt the commercial grade titanium A-40 evaporant was always maintained at 0.3 amp. Since  $5 \times 10^{-4}$  torr is the highest pressure in which a thermionic emission type electron gun can be conveniently operated, a pressure barrier was built to make evaporation at higher pressures possible. Other macro-details of the experimental apparatus have been published previously.<sup>(6)</sup> The substrate geometry is shown in Fig. 1. The relationship between a shadowing tab and the evaporant source is also displayed. The surface on the back



SUBSTRATE DETAILS  
AND POSITION OF  
SHADOWING TAB WITH  
RESPECT TO THE  
EVAPORANT SOURCE

Fig. 1 Substrate and relevant system geometry

side of the 45° tab and the region on the large flat substrate behind the tab are effectively removed from line-of-sight deposition from the source. The substrates were preheated to and then maintained at 550°C by a low voltage (20 v a.c.) incandescent tungsten wire heater.

The experimental variables were:

1. Type of gas -- $C_2H_2$ ,  $C_2H_4$ ,  $O_2$ , or Ar.
2. Nominal gas pressure --  $5 \times 10^{-4}$ ,  $5 \times 10^{-3}$ , or  $2.5 \times 10^{-2}$  torr.
3. Ionization or no ionization, i.e., GSE, RE, or ARE.
4. Source to substrate distance -- 4 1/4" or 6".

The results of the parameter variations were evaluated in terms of:

1. Deposition efficiency.
2. Deposit thickness profile.
3. Composition of deposit, viz. Ti, Ti + TiC, TiC, or  $TiO_2$ .
4. Plating in a shadow, i.e., in a region not in a direct line-of-sight from the evaporant source to the substrate.

#### Efficiencies

The deposition efficiency of any of the evaporation processes is defined to be the rate of deposition of titanium onto a 6"x6" substrate at a specified source to substrate distance divided by

the rate of evaporation from a 1.0 in. diameter molten pool being heated by an electron beam current of 0.3 amp. When the deposit was TiC, the efficiency is based upon the amount of titanium in the deposit, combined and free, as determined by x-ray analysis of lattice parameters and the data of Storms. (7)

When Ar was admitted into the system, there was negligible difference between the efficiency of the GSE process and the ARE process. The efficiency of both processes decreased 18% when the pressure of Ar was increased from  $5 \times 10^{-4}$  to  $5 \times 10^{-3}$  torr.

When  $C_2H_2$  was admitted, the efficiencies were constant over the same pressure interval, with the RE process being 8% more efficient than the ARE process. For  $C_2H_4$ , the efficiency of the ARE process decreased by 9% when the pressure was increased from  $5 \times 10^{-3}$  to  $2.5 \times 10^{-2}$  torr. Efficiencies were not computed for the RE process using  $C_2H_4$  since no TiC was formed. The results of all the experiments show that the efficiency of the ARE process in general is the same or slightly less than the RE or GSE processes.

#### Profiles

The deposit thickness profiles were always measured along the same diagonal across the square substrates, in the same direction, and plotted accordingly. Figs. 2-4 present typical profiles. The dotted center section of each curve is where the tab was

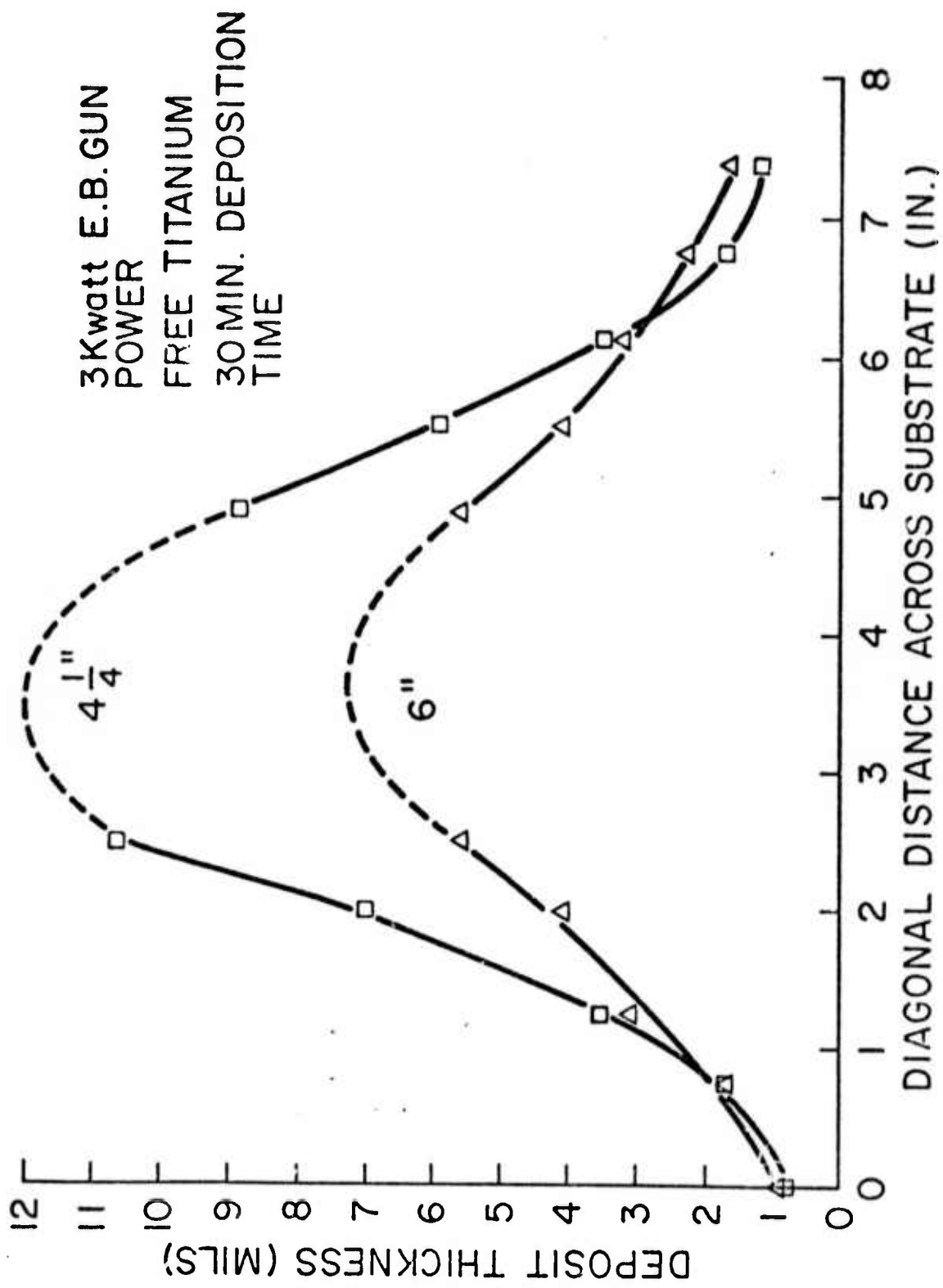


Fig. 2 Typical deposit thickness profiles for different source to substrate distances.

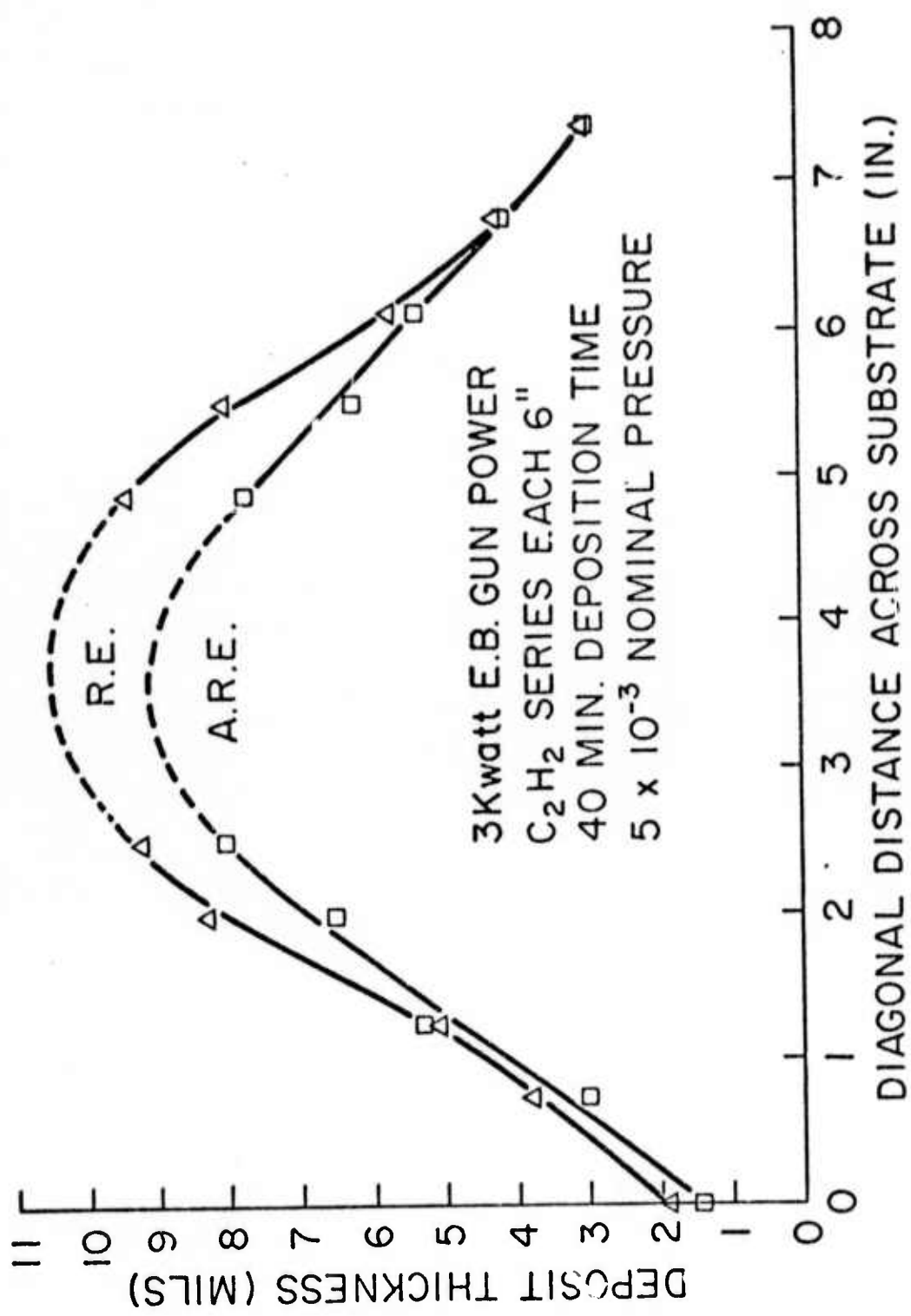


Fig. 3 Typical deposit thickness profiles for different evaporation processes at a 6" source to substrate distance.

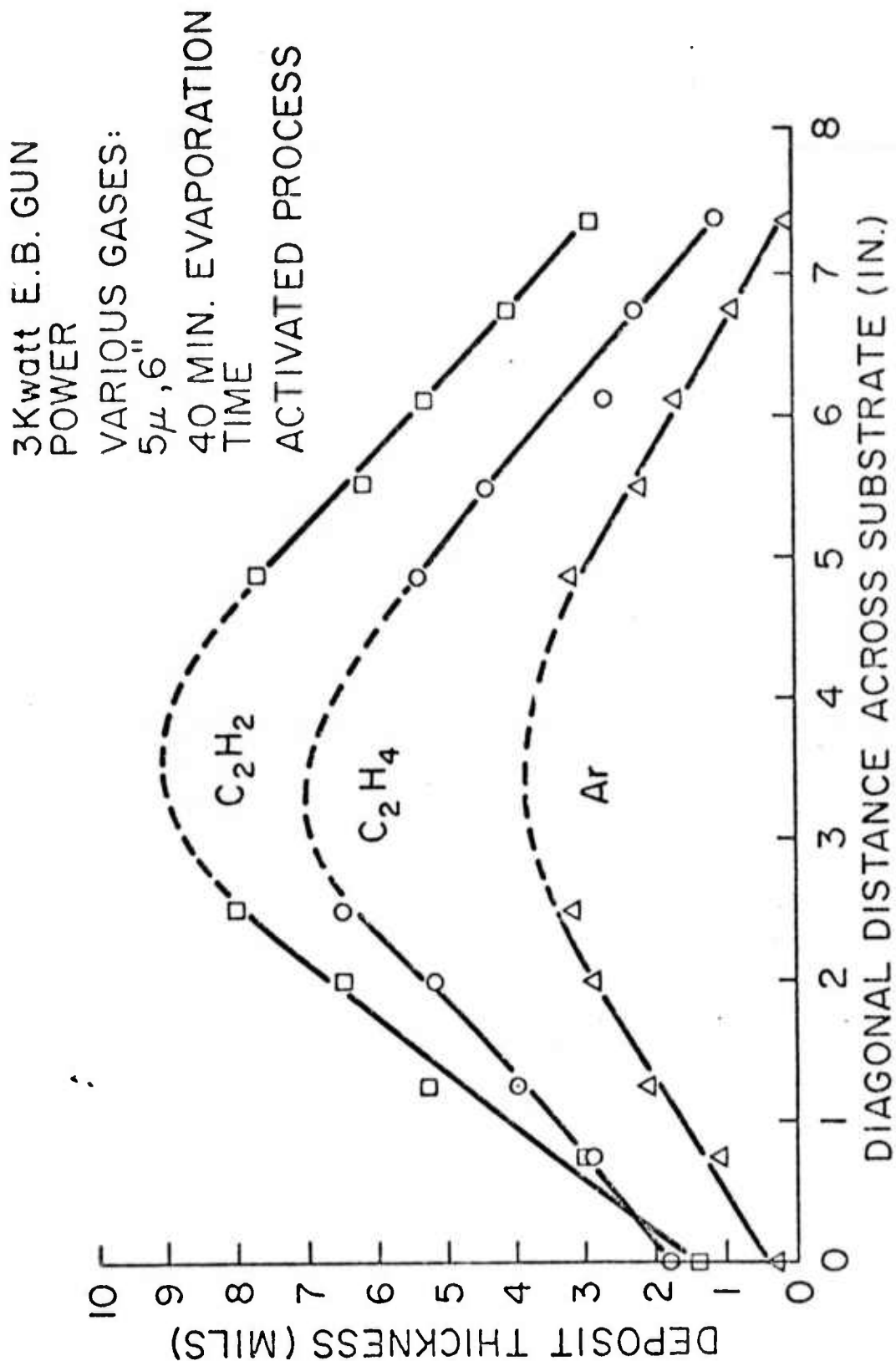


Fig. 4 Deposit thickness profiles for different gases employed in the ARE process. Source to substrate distance is 6" and pressure is  $5 \times 10^{-3}$  torr.

located. The effect of source to substrate distance on the deposit profile is shown in Fig. 2. These deposit thickness profiles deviate from the ideal cosine law distribution. The deviation is exhibited by the reversal of curvature toward the edges of the profile. The points of inflection are typically 2 in. away from center, on either side, along the diagonal of measurement. This deviation phenomenon is not due to any apparent geometrical constraint of the experimental apparatus. Fig. 3 shows profiles which are typical of the difference between the RE and the ARE processes. For the RE and GSE (not shown) processes, the deviation from the ideal cosine law distribution is still exhibited by the reversal in curvature in directions away from center. However, when the ARE configuration is employed with a gas present, reactive or non-reactive, the profile exhibits a single curvature, as shown in Figs. 3 and 4. Fig. 3 also indicates the slightly lower efficiency of the ARE process compared to the RE process. The differences in deposit profiles in Fig. 4 are partially due to the complete formation of TiC when  $C_2H_2$  is used, partial formation, i.e., a mixture of Ti and TiC, when  $C_2H_4$  is used, and only Ti when Ar is used. Therefore the volume or thickness of the deposits should increase in the manner shown when the carbonaceous gases are used, since the deposit represents more than just the evaporated material from the source.

Figs. 5 and 6 present the profile data from several experiments in a more concise form to allow direct comparison. The data points were determined by measuring the total thickness deposited during the run at a specified point on the deposit divided by the rate of evaporation. Consequently the data is independent of time. When no gas is present and the ARE configuration is employed, a Ti plasma exists above the molten pool and forms a cone which extends up to the substrate. The increase in the thickness of the deposit toward the center of the substrate is a demonstration of the confining property of the plasma cone and is shown by a larger separation of the two curves. Ar is shown to be a very effective gas scatterer in either the GSE or ARE mode, as indicated by the decrease in the curves. However, the profile is smoother for the ARE configuration, i.e., does not deviate from a single curvature as discussed above. The latter point is indicated by the decreased separation between the two curves for the ARE experiment. The thickness is greater when  $C_2H_2$  is employed due to the formation of TiC and again the profile is smoother for the ARE process. The saturated plasma experiments were performed by increasing the activating voltage in the ARE experimental configuration. This increases the density of the plasma by ionizing a greater portion of the evaporant flux. The deposit profiles are smoother, but the process efficiencies have also decreased. Fig. 6 shows that a similar

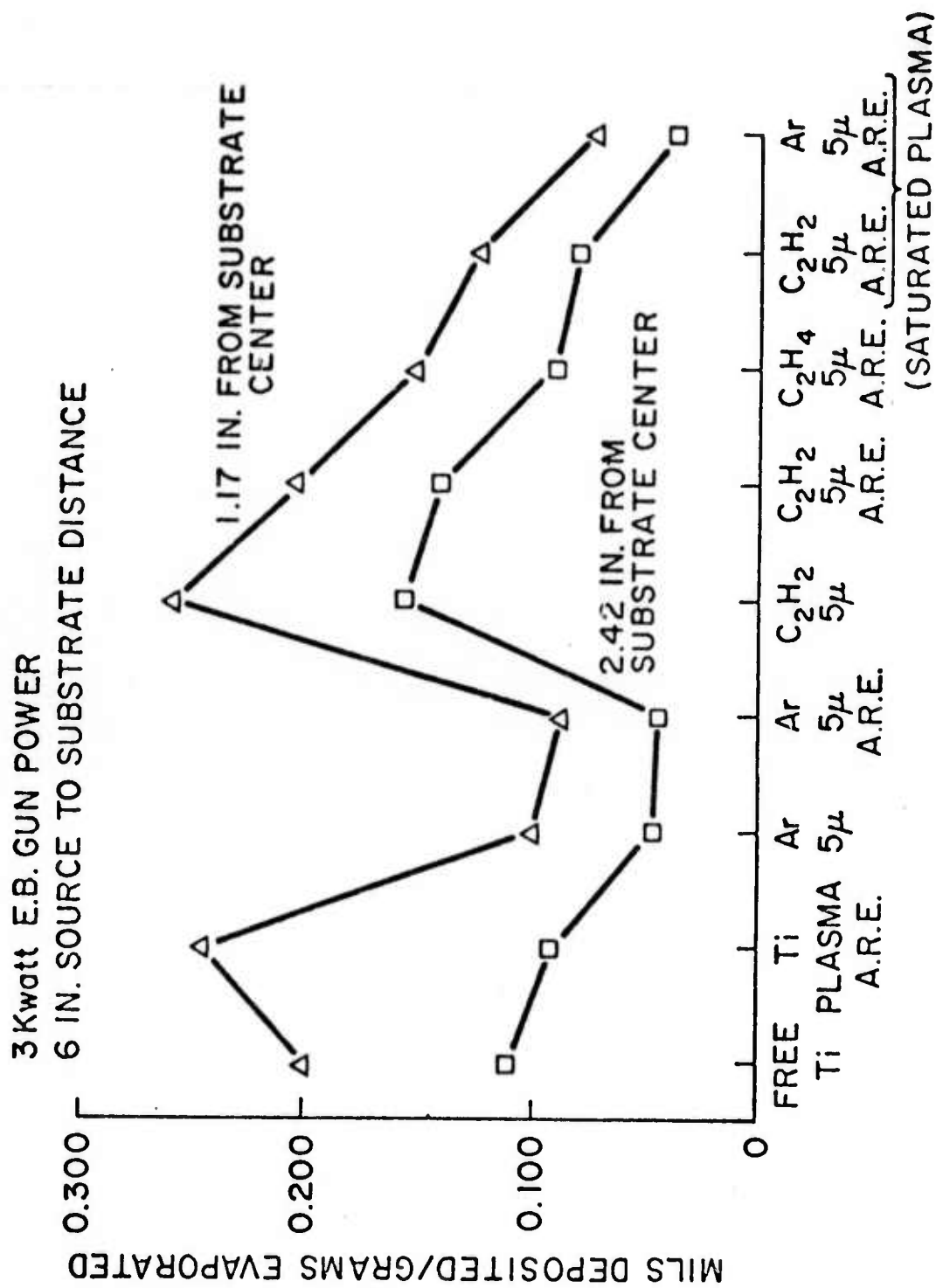


Fig. 5 Profile - efficiency data for various gases used in various evaporation processes at a 6" source to substrate distance.

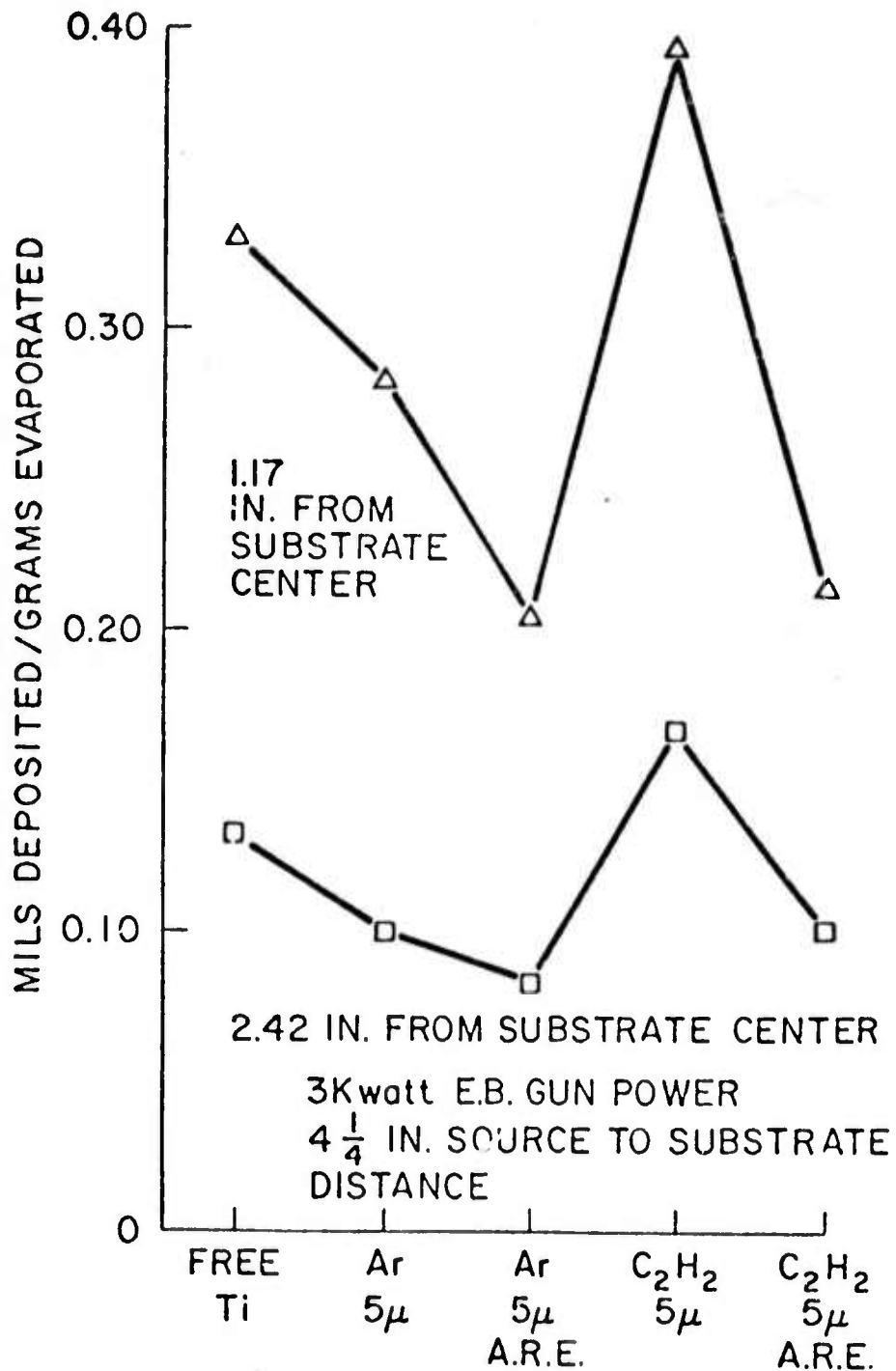


Fig. 6 Profile - efficiency data for various gases used in various evaporation processes at a 4 1/4" source to substrate distance.

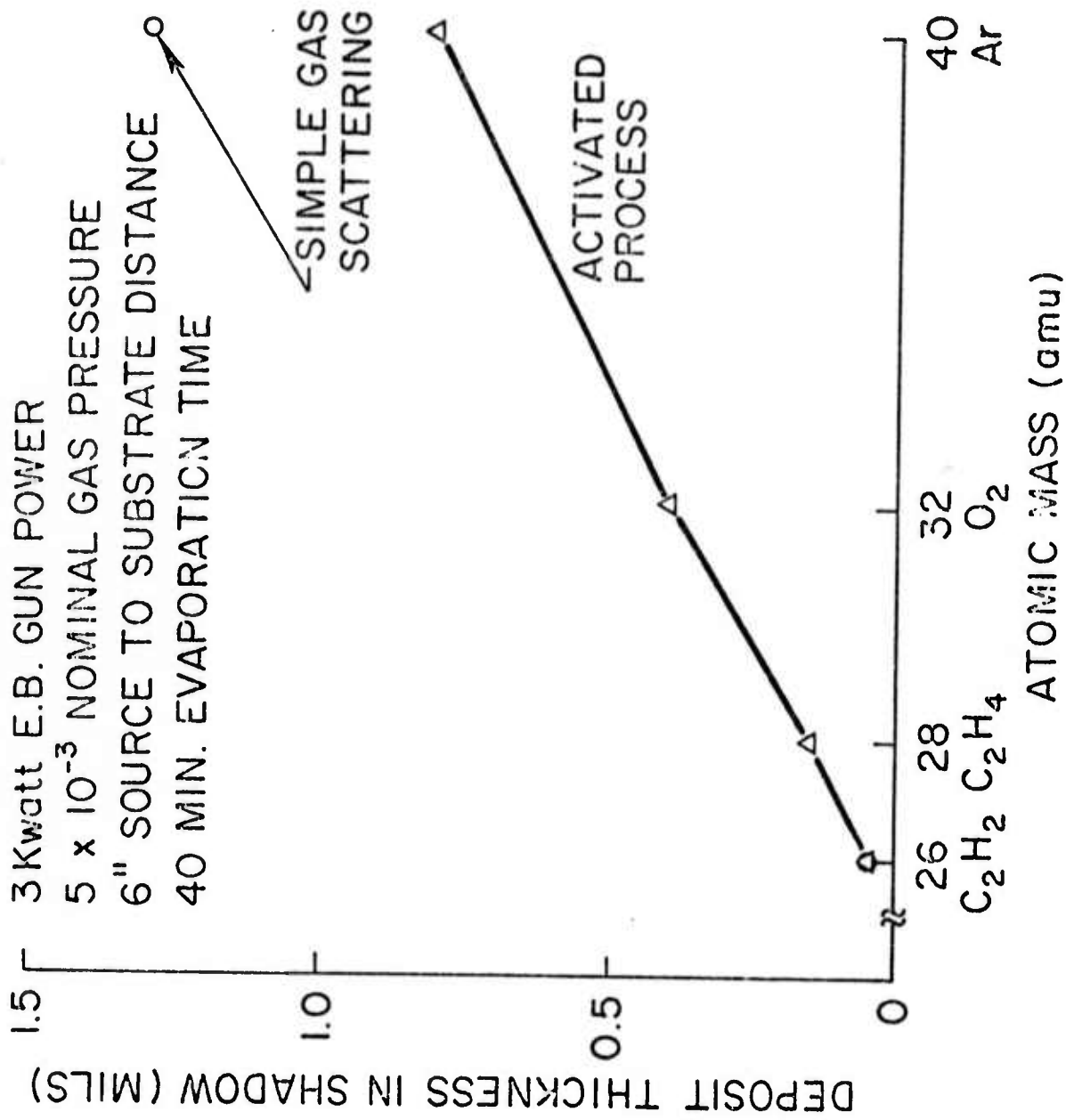


Fig. 7 Effective scattering abilities of various gases when used with a titanium evaporant.

analysis applies for a shorter source to substrate distance.

As expected for a shorter distance, Fig. 6 also indicates greater deposition efficiencies.

#### Composition

As indicated earlier, TiC was always formed when  $C_2H_2$  was employed in the ARE mode while the formation was incomplete in the RE mode. TiC was only formed when  $C_2H_4$  was employed in the ARE mode.  $TiO_2$  was always formed when  $O_2$  was used in either the RE or ARE mode.

#### Shadowing Effects

Fig. 7 displays the results of the scattering abilities of the various gases. The scattering process becomes much more efficient as the mass of the gas molecule approaches that of the evaporant (Ti ~ at. wt. = 47.9 a.m.u.). There is a gradient in the profile of the deposit in the region on the large flat substrate which is located behind the 45° tab. The deposit gets thinner as the apex of the 45° angle is approached. The deposit thicknesses were measured half-way between the apex and the forward edge of the shadowed region. The presence of the gradient in the deposit is largely due to the height gradient presented by the tab being positioned at a 45° angle with respect to the large flat substrate.

After the mass of the gas, the next most important variable was the pressure of the gas. The thickness of the deposit in the shadow doubled when the pressure of  $C_2H_4$  was increased from  $5 \times 10^{-3}$  to  $2.5 \times 10^{-2}$  torr. With Ar, plating in the shadow occurred at pressures as low as  $5 \times 10^{-4}$  torr, with thickness of the deposit increasing with pressure.

#### Conclusions

From the study, it is clear that non-line-of-sight coating by evaporation is made feasible by utilizing gas scattering.

For this purpose, ion-plating, which is a more complicated process, is not necessary.

This investigation indicates that non-line-of-sight plating is primarily influenced by the mass of the gas chosen for the scattering phenomenon. The choice is dictated on a simple momentum exchange principle. The second contributing factor is the pressure of the gas. This choice is dictated by the amount of gas required to accomplish the desired degree of scattering.

References

1. K.D. Kennedy, G.R. Scheuermann, and H.R. Smith, Jr.: R and D mag., Nov. (1971), 40.
2. R.C. Krutenat: U.S. Patent No. 3, 639, 151.
3. D.M. Mattox: J. Vac. Sci. Technol., 10 (1973), 47.
4. C.T. Wan, D.L. Chambers, and D.C. Carmichael: Proceedings of the 1971 Vacuum Metallurgy Conference, (1971) VM99 American Vacuum Society, New York.
5. M.C. Paul and P.E. Oberg: U.S. Patent No. 3,373,050.
6. R.F. Bunshah and A.C. Raghavan: J. Vac. Sci. Technol., 9 (1972), 1385.
7. E.K. Storms: Refractory Metal Carbides, (1967) 8 Academic Press, New York.
8. L. Holland: Vacuum Deposition of Thin Films, (1966) 21 Chapman and Hall, London.

PART II

THE PROPERTIES OF RARE EARTH METALS AND ALLOYS

TASK IV

THE OXIDATION MECHANISM OF  $\text{Ni}_3\text{Al}$  CONTAINING YTTRIUM

by

D. L. Douglass and J. D. Kuenzly

Materials Department  
School of Engineering and Applied Science  
University of California  
Los Angeles

32

## ABSTRACT

The high-temperature oxidation behavior of  $\text{Ni}_3\text{Al}$  (Ni-13.2 w/o Al) with and without additions of 0.5 w/o yttrium has been studied over the range of 900 to 1200°C in air. None of the commonly accepted rate laws were followed by the kinetics. Although the weight gains of samples containing yttrium were consistently 10 to 20% greater than those without yttrium, the steady-state scaling rates were identical.

A quantitative X-ray diffraction technique was used to determine the kinetics of growth of the protective alpha-alumina layer (one of several oxides formed). The alumina growth followed the parabolic rate law under all conditions studied. The rate-controlling transport process in alumina was the enhanced diffusion of oxygen down grain boundaries.

The presence of yttrium as nickel-rich intermetallics promoted the formation of nickel aluminate (spinel). A marked increase in scale adherence was observed for short times. At longer times, however, the outer layer of spinel and unreacted nickel oxide spalled off along with some of the inner alumina layer. Loss of adherence was caused by a complex yttrium-aluminum oxide which formed by the solid-state reaction of yttria and alumina.

The poor scale adherence on  $\text{Ni}_3\text{Al}$  was due to the formation of voids at the alloy/oxide interface. These voids concentrated the athermal stresses above the oxide-to-metal adherence strength. The voids were produced as a result of the selective oxidation of aluminum resulting from a "Kirkendall" effect in the substrate. During the selective oxidation process, a vacancy flux directed from the matrix to the metal/oxide interface resulted in a supersaturation of vacancies. Equilibrium was maintained by the condensation of excess vacancies. The presence of yttrium as either nickel-rich intermetallics or internal oxide prevented the voids from forming. The yttrium-rich particles relieved the matrix of vacancy supersaturation by providing vacancy sinks.

The chemical nature of the particles does not seem important. A necessary and sufficient condition for an effective vacancy sink appears to be the presence of an incoherent boundary between particle and matrix.

## LIST OF FIGURES

1. Parabolic Plot of the Isothermal Oxidation Kinetics for Ni<sub>3</sub>Al in One Atm. Air from 900-1200°C.
2. Parabolic Plot of the Isothermal Oxidation Kinetics for Ni<sub>3</sub>Al-0.5Y in One Atm. Air from 900-1200°C.
3. Arrhenius Plot Showing Temperature Dependence of Steady-State Oxidation Rates.
4. X-Ray Diffractometer Traces of Scales Formed on Alloys Oxidized 11 Days at 900°C.
5. X-Ray Diffractometer Traces of Scales Formed on Alloys Oxidized Seven Days at 1200°C.
6. X-Ray Diffractometer Traces of Scales Formed on Ni<sub>3</sub>Al-0.5Y After Subsequent Oxidation Following Spalling at 1200°C.
7. X-Ray Diffractometer Traces of the Scale Development on Ni<sub>3</sub>Al-0.5Y during the Transient Periods at 1200°C.
8. X-Ray Diffraction Intensities of Oxides Formed on Ni<sub>3</sub>Al-0.5Y during the Transient Periods at 1200°C.
9. Isothermal Oxidation Kinetics of α-Al<sub>2</sub>O<sub>3</sub> on Ni<sub>3</sub>Al-0.5Y from 900 to 1200°C as Measured by X-Ray Diffraction Intensities.
10. Temperature Dependence of α-Al<sub>2</sub>O<sub>3</sub> Formation on Ni<sub>3</sub>Al-0.5Y from 900 to 1200°C.
11. Spalled Oxides on Ni<sub>3</sub>Al after 2 Days Oxidation in Air at 1000°C.  
(a) Oxides, 200X, (b) Substrate, 2000X. Surface Tilted 35° from Electron Beam.
12. Failure of Alumina Film on Ni<sub>3</sub>Al After 10 min. Oxidation at 1200°C.  
(a) 500X, (b) 2000X. Surface Tilted 35° from Electron Beam.
13. Typical Morphologies of the Spalled Alumina Film Formed on Ni<sub>3</sub>Al after Seven Days Oxidation at 1200°C in Air. (a) Al<sub>2</sub>O<sub>3</sub>/Gas Interface, 5000X,  
(b) Al<sub>2</sub>O<sub>3</sub>/Substrate Interface, 1850X. 30° Tilt from Beam.
14. Cross-section of the Fractured Al<sub>2</sub>O<sub>3</sub> Film Formed Seven Days on Ni<sub>3</sub>Al at 1200°C in Air. 1900X.
15. Outer Edge of the Cross-section Appearing in Figure 14. 5000X.
16. Adherent Scale Formed on Ni<sub>3</sub>Al-0.5%Y after Two Days Oxidation at 1000°C in Air. (a) 400X, (b) Grain Boundary Oxide, 2000X.

17. Concentration Profiles Across the Grain Boundary Area of Fig. 16 (b).
18. Plan View of the Adherent Oxides Formed on Ni<sub>3</sub>Al-0.5%Y Oxidized Two Days at 1100°C in Air. 400X.
19. Localized Scale Failure on Ni<sub>3</sub>Al-0.5%Y Following Oxidation at 1200°C for Four Hours in Air. 2000X. 35° Tilt from Beam.
20. Concentration Profiles Through the Spalled Area of Fig. 19.
21. Typical Particle Protruding from the Spalled Surface of Ni<sub>3</sub>Al-0.5%Y after Seven Days Oxidation at 1200°C in Air. 2000X.
22. Concentration Profiles Through the Particle of Fig. 21.
23. Substrate Topography on Ni<sub>3</sub>Al-0.5%Y after Scale Failure. 10,000X.
24. Substrate Topography on Ni<sub>3</sub>Al-0.5%Y after Scale Failure. 10,000X.
24. Composite Scale Formed on Ni<sub>3</sub>Al-0.5%Y Oxidized for Seven Days at 1200°C in Air. 1900X.
25. Concentration Profiles Through the Area Indicated in Fig. 24.
26. Scale Morphology of the Scale Formed on Ni<sub>3</sub>Al-0.5%Y after Seven Days Oxidation at 1200°C in Air. 3000X.
27. Temperature Dependence of Diffusional Processes in Al<sub>2</sub>O<sub>3</sub>.
28. Arrhenius Plot Comparing the Oxidation Kinetics of Ni<sub>3</sub>Al with the Results of Pettit.(12)
29. Diffusional Characteristics in Ni<sub>3</sub>Al During the Selective Oxidation of Aluminum.
30. Mechanism of Void Production in Ni<sub>3</sub>Al at Lower Temperatures.
31. Void Formation in the Substrates of Alloys Oxidized for 12 Hours at 1200°C. (a) Ni<sub>3</sub>Al, 500X, (b) Aluminized Ni<sub>3</sub>Al, 2000X.
32. Schematic Development of Oxides on Ni<sub>3</sub>Al-0.5%Y.
33. X-ray Diffractometer Sample Geometry.

#### LIST OF TABLES

1. Miscellaneous Mechanical and Thermal Property Data.

## 1. INTRODUCTION

The oxidation rates of nickel-base alloys forming protective  $\alpha\text{-Al}_2\text{O}_3$ \* oxides are lower than the rates of alloys forming other scales, e.g., NiO or  $\text{Cr}_2\text{O}_3$ . The practical application of these alloys has been limited to 1000°C by poor creep resistance and film spallation during thermal cycling. A new class of oxide-dispersion-strengthened alloys has elevated the useful strength capabilities to 1200°C. Submicron thoria, yttria, and ceria dispersions are commonly used. The oxidation resistance of alloys forming protective  $\text{Cr}_2\text{O}_3$  scales is markedly improved, whereas, the rates of alloys forming protective  $\text{Al}_2\text{O}_3$  films are unaffected. However, the resistance to film spallation is dramatically improved in the dispersion-containing alloys. The effect is also enhanced<sup>(1)</sup> by the addition of minute amounts of rare earth or reactive metals to the more conventional alloys, but the responsible mechanism(s) have not been clarified.

The concluding program has defined the mechanisms of scale adherence and spallation, and has characterized the oxidation behavior of certain alloys containing rare earth additions.

## 2. EXPERIMENTAL PROCEDURE

### 2.1 Sample Preparation

High-purity nickel (99.99%) and aluminum (99.99%) were used for the base alloy; 0.5% yttrium (99.9%) was added to the base alloy. One-hundred gram buttons were prepared by arc-melting on a water-cooled copper hearth in an inert argon atmosphere. The buttons were turned and remelted six times. Gettering of residual oxygen and nitrogen was accomplished by premelting a titanium button.

Coupons were cut from the as-melted buttons and given a 24-hour homogenization vacuum anneal at 1200°C. Final sample preparation consisted of sanding through 4/o SiC paper and spark-erosion cutting a 1.5mm hole for suspending the coupons in the thermogravimetric apparatus. A final vacuum anneal for 20 minutes at 900°C was performed to remove any work-hardening introduced by the polishing process.

---

\* All subsequent entries of  $\text{Al}_2\text{O}_3$  are implied to mean the alpha-alumina or corundum structure.

The base alloy was single-phase  $\text{Ni}_3\text{Al}(\gamma')$ . The aluminum composition varied between 12.9 and 13.2%. The matrix of the yttrium-doped alloy was single-phase  $\text{Ni}_3\text{Al}(\gamma')$ . X-ray diffraction techniques revealed the presence of  $\text{Ni}_9\text{Y}$  and  $\text{Ni}_7\text{Y}_2$  intermetallics in the surface layers. A very weak  $\text{Y}_2\text{O}_3$  reflection was observed. It appeared that some yttrium was converted to  $\text{Y}_2\text{O}_3$  during fabrication and/or annealing.

## 2.2 Oxidation Tests

Isothermal oxidation was performed in one atm. air over the temperature range of 900-1200°C. A Harrop Thermogravimetric Analyzer (TGA) using a high sensitivity (0.05mg) electro-balance was used to produce continuous weight-gain/time curves for tests of two days' duration. Sample surface areas varied between 4 and 9  $\text{cm}^2$ . Tests of longer or shorter duration were performed in a 4-inch diameter, vertically mounted Marshall furnace. Samples tested with this arrangement were intermittently removed and weighed. Scale adherence during thermal cycling was effectively monitored by this method. Initial and final weights were determined on a Mettler Fl6 analytical balance having an accuracy of 0.05mg. All samples were suspended by Pt-13%Rh thermocouple wire.

Problems existed initially with the Harrop unit as there were no internal provisions for lowering the specimen from a protected cold zone directly into the hot test medium. Consequently, a specimen placed in the furnace undergoes a non-isothermal, transient oxidation period that completely alters the scaling mode. Heat-up time to 1200°C was about 30 minutes. The overall effect is to form copious amounts of  $\text{NiO}$  during heat-up, thereby altering the aluminum concentration at the alloy/oxide interface. A comparision of the isothermal oxidation kinetics with literature values would be invalid. Heating the sample in vacuum or in an inert gas to the desired test temperature, and then admitting the reactive environment, results in the selective oxidation of aluminum.

Accurate balance zero points were also difficult to determine due to transient convection effects. These problems were circumvented by pre-oxidizing the samples containing yttrium ( $\text{Ni}_3\text{Al}-0.5\%\text{Y}$ ) for one hour in the Marshall furnace. The sample was then removed, weighed, immediately placed into the Harrop unit at about 300°C, and elevated to the desired test temperature. No spalling was observed with  $\text{Ni}_3\text{Al}-0.5\%\text{Y}$  after the

one hour pre-oxidation. Samples of the base alloy, Ni<sub>3</sub>Al, spalled when the one-hour pre-oxidation was attempted at 1100 and 1200°C. A crude but usable technique was developed to allow direct sample immersion into the Harrop hot zone already at temperature. Samples were dropped onto the hanging hook by an additional Pt-13%Rh wire while the suspension assembly was rigidly secured by a third wire. Balance zeros were achieved within 30 to 40 seconds with this method. Weight gains during this interval were minimal as the samples themselves required 75 to 80 seconds to reach the test temperature. Additional samples of Ni<sub>3</sub>Al-0.5%Y were also oxidized in this manner. Excellent agreement was obtained with the samples that were pre-oxidized first.

### 2.3 Analysis of Oxide Films

X-ray diffractometer analyses were made on the "in-situ" scales and spalled oxides. A Phillips Norelco diffractometer was used with nickel-filtered copper radiation. The nickel filter was placed in the primary beam to reduce nickel fluorescence caused by CuK<sub>β</sub> radiation. The signal-to-noise ratio was considerably increased.

Certain samples of the alloy containing yttrium were intermittently oxidized and subjected to quantitative X-ray diffraction techniques. The scaling behavior during the transient periods was established as a function of time on the same sample.

The surface morphologies of the "in-situ" scales were examined in a Cambridge Scanning Electron Microscope (SEM). A Kevex solid-state energy spectrometer was used in conjunction with the SEM to determine the distribution of elements in the scales. The substrates were easily examined when the oxide had spalled. Substrates containing very adherent oxides were examined by the following method. The sample was quenched from high temperature into liquid nitrogen and followed by scraping with a diamond stylus, or sharp blows on the sample edge with a hammer to remove the oxide, if necessary. The underside of the adherent Al<sub>2</sub>O<sub>3</sub> films (that next to the alloy) was examined by dissolving the substrate in a 10% bromine-methanol solution. The oxide was collected, washed, dried and mounted for analysis.

All oxides prepared for examination in the SEM were vacuum-coated with silver to reduce the "charging" effects caused by secondary emission

coefficients less than unity. Lower accelerating voltages (5 to 10 KeV instead of 20 KeV) were tried, but resolution was poor, and the excited X-ray intensity was too low because of the high absorptivity of silver.

Some samples were prepared in cross-section and polished to  $0.05\mu$   $\text{Al}_2\text{O}_3$ , but this resulted in ambiguous polishing artifacts. Oxide had a tendency to "pull-out" and high resolution detail of the alloy/oxide interface was lost.

### 3. RESULTS

#### 3.1 Thermogravimetric Analysis

The isothermal oxidation curves from 900 to 1200°C for the two alloys,  $\text{Ni}_3\text{Al}$  and  $\text{Ni}_3\text{Al}-0.5\%Y$  are presented in Figs. 1 and 2 as parabolic plots. No isothermal spalling was observed with either alloy. The presence of yttrium increased the total weight gain by 10 to 20% at all temperatures.

Although neither alloy followed a strict parabolic time dependence, it was instructive to compare the temperature dependence of the steady-state scaling rates for both alloys. This temperature dependence of the steady-state scaling rate is shown as an Arrhenius plot in Fig. 3. The activation energy for both alloys was 46.8 Kcal/mole. The complex nature of the scales formed and the fact that the parabolic time law was not followed for the total weight gain over the complete time period precludes a detailed analysis of the Arrhenius plot. It is clear, however, that yttrium did not alter the steady-state scaling rate of  $\text{Ni}_3\text{Al}$ .

#### 3.2 X-Ray Diffraction

X-ray diffractometer traces comparing characteristic low (900°C) and high (1200°C) temperature scales are illustrated for the two alloys in Figs. 4 and 5, respectively. The low temperature scales consisted of an outer layer of  $\text{Ni}_3\text{Al}$ , an intermediate layer of  $\text{NiAl}_2\text{O}_4$  and an inner layer of  $\text{Al}_2\text{O}_3$ . Both alloys were intermittently weighed and reimmersed to the test temperature. No spalling was observed on  $\text{Ni}_3\text{Al}-0.5\%Y$ , however, at the end of 11 days, limited spalling occurred from  $\text{Ni}_3\text{Al}$ . The high-temperature scales on both alloys spalled during cooling. The oxide formed on  $\text{Ni}_3\text{Al}$  detached in large flakes, whereas that on  $\text{Ni}_3\text{Al}-0.5\%Y$

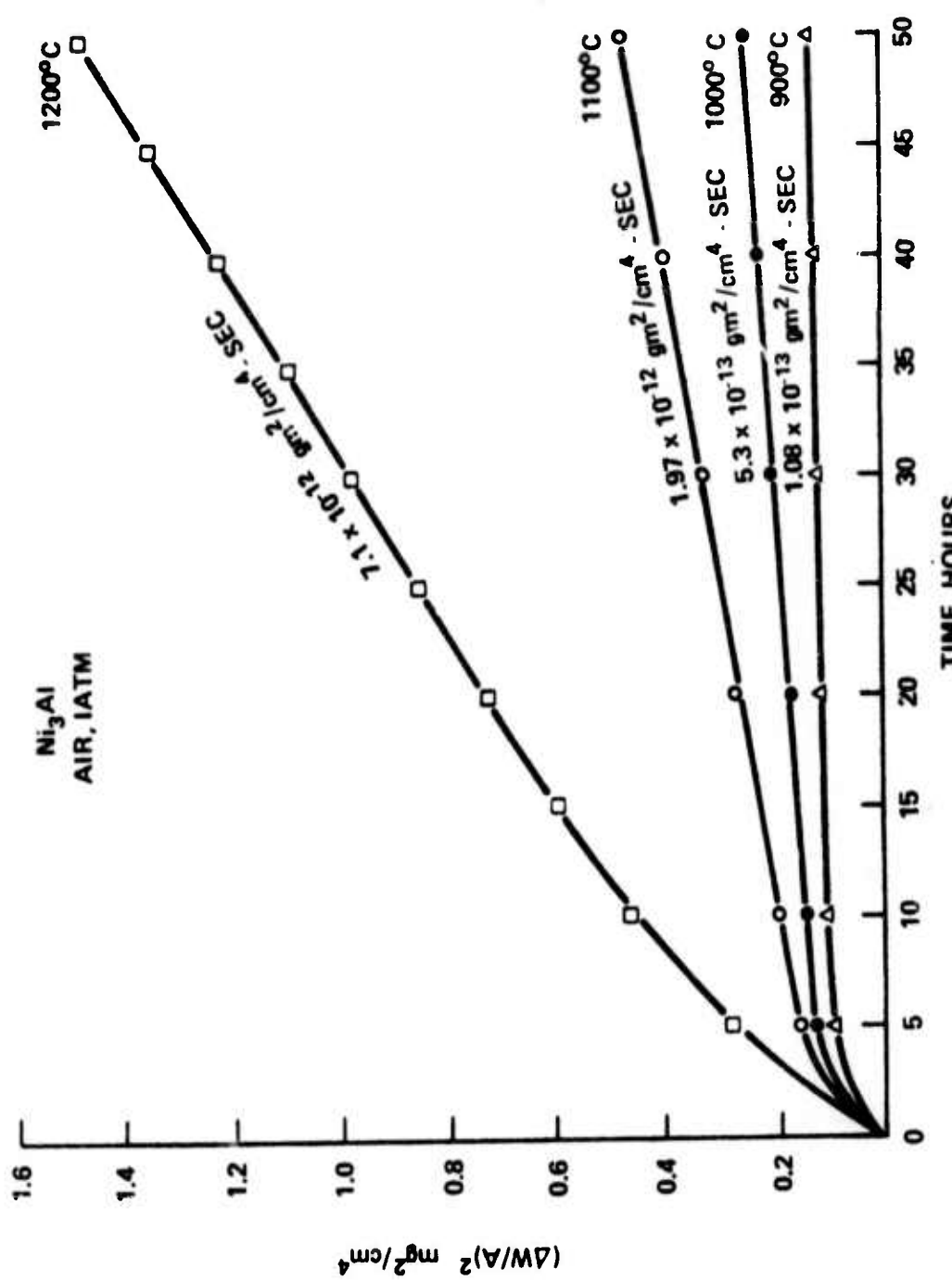


Figure 1 Parabolic Plot of the Isothermal Oxidation Kinetics for  $\text{Ni}_3\text{Al}$  in One Atmosphere from 900-1200°C.

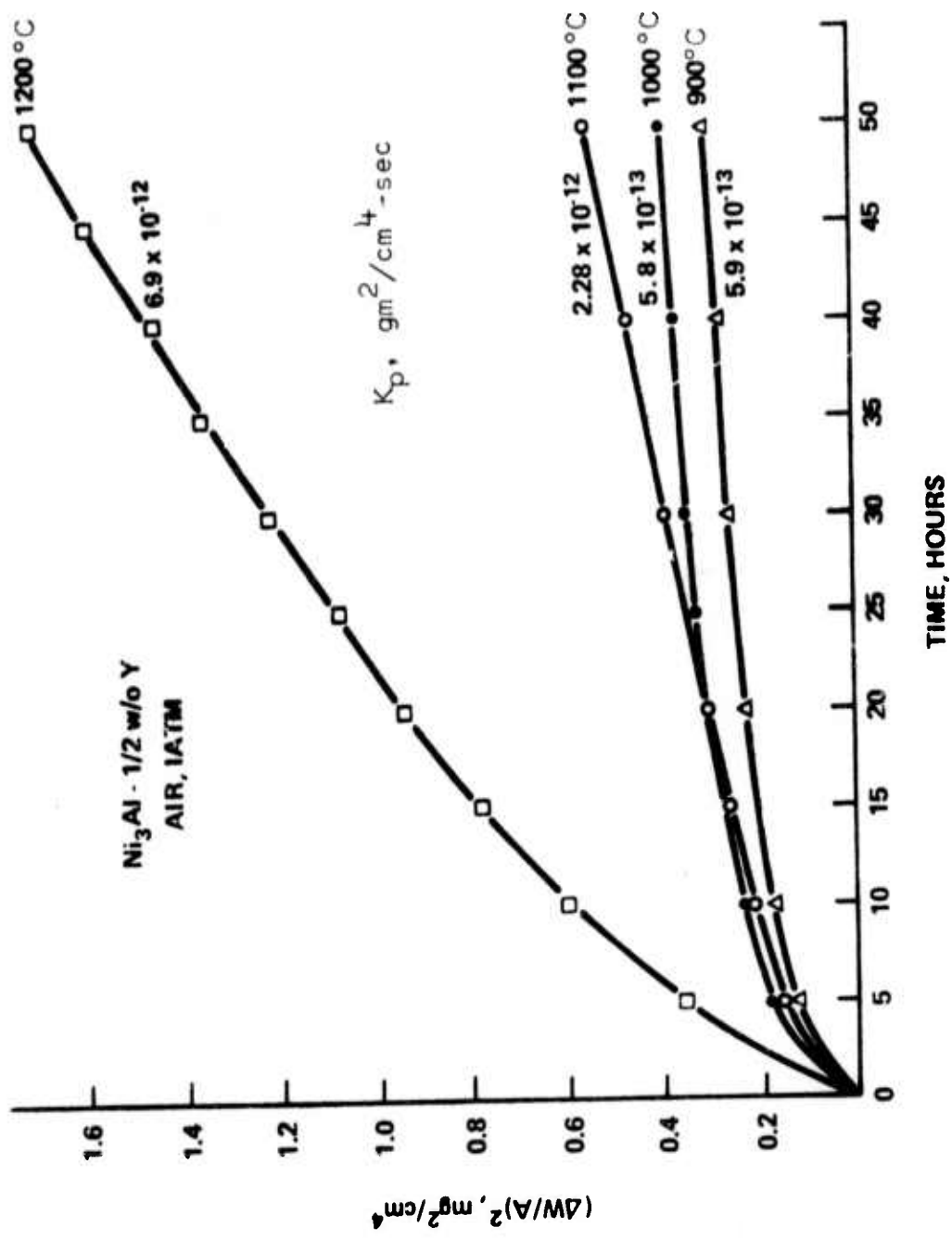


Figure 2 Parabolic Plot of the Isothermal Oxidation Kinetics for  $\text{Ni}_3\text{Al}-0.5\text{Y}$  in One Atm. Air from 900-1200°C.

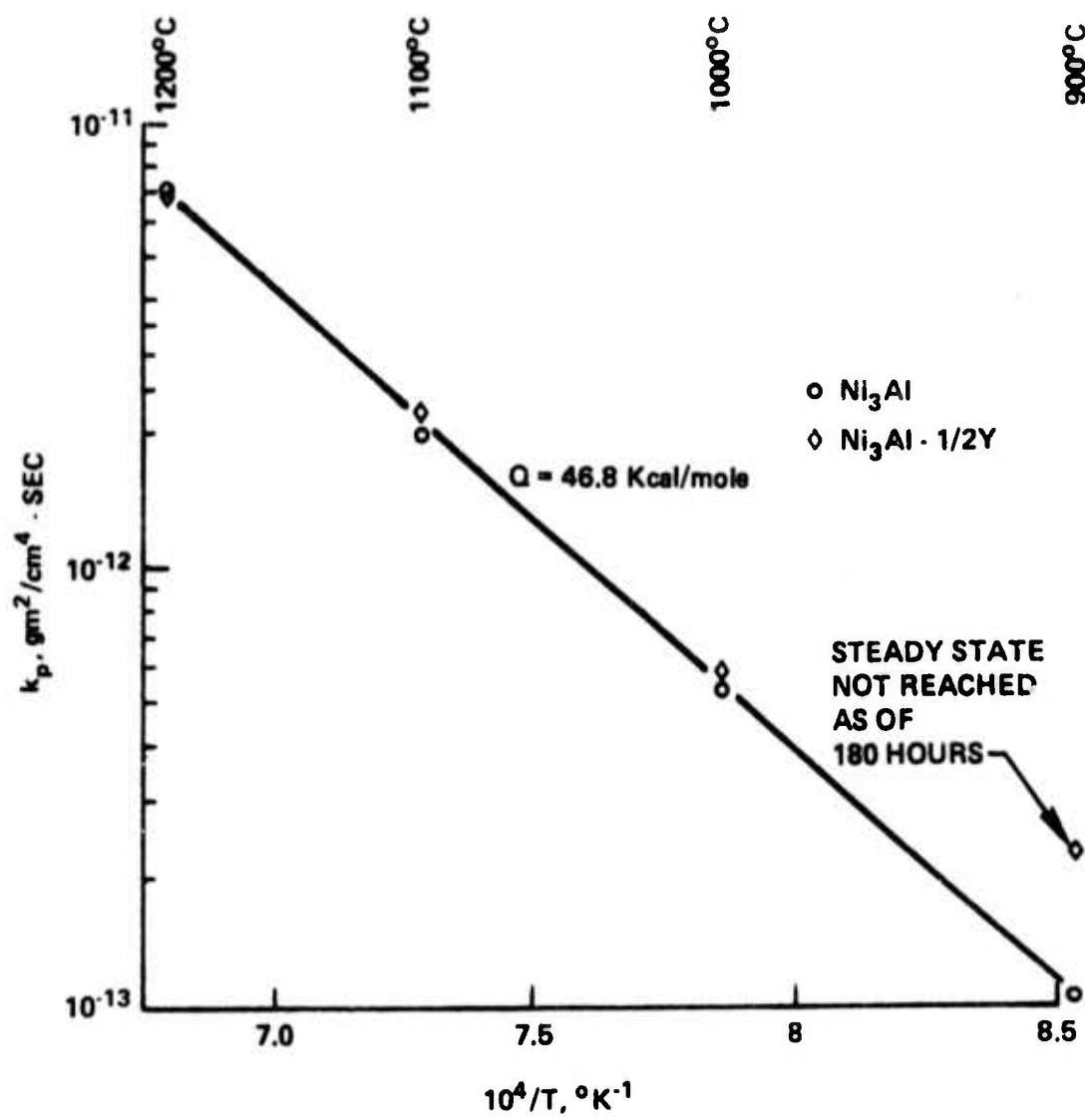


Figure 3 Arrhenius Plot Showing Temperature Dependence of Steady-State Oxidation Rates.

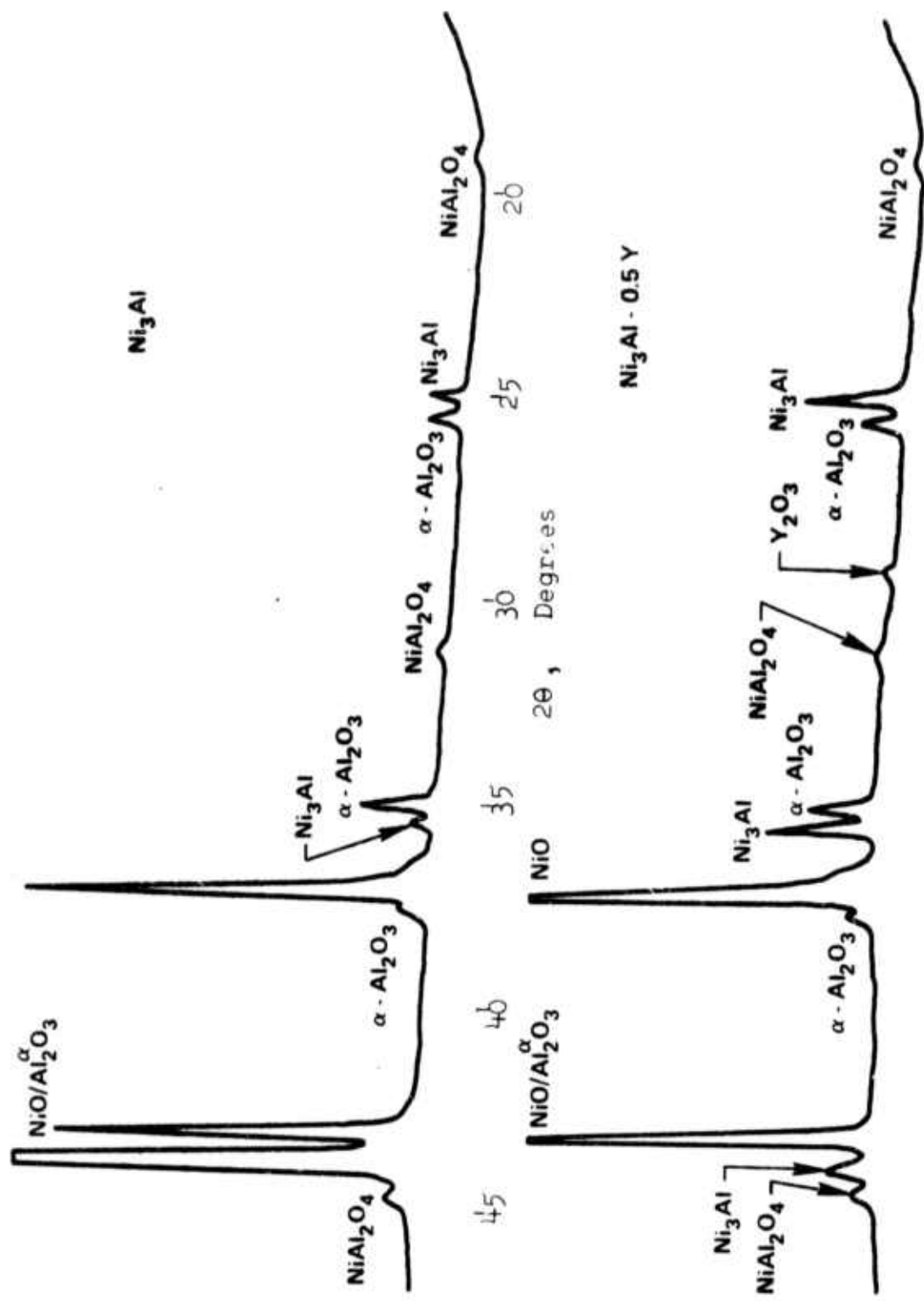


Figure 4 X-Ray Diffractometer Traces of Scales Formed on Alloys Oxidized 11 Days at 900°C.

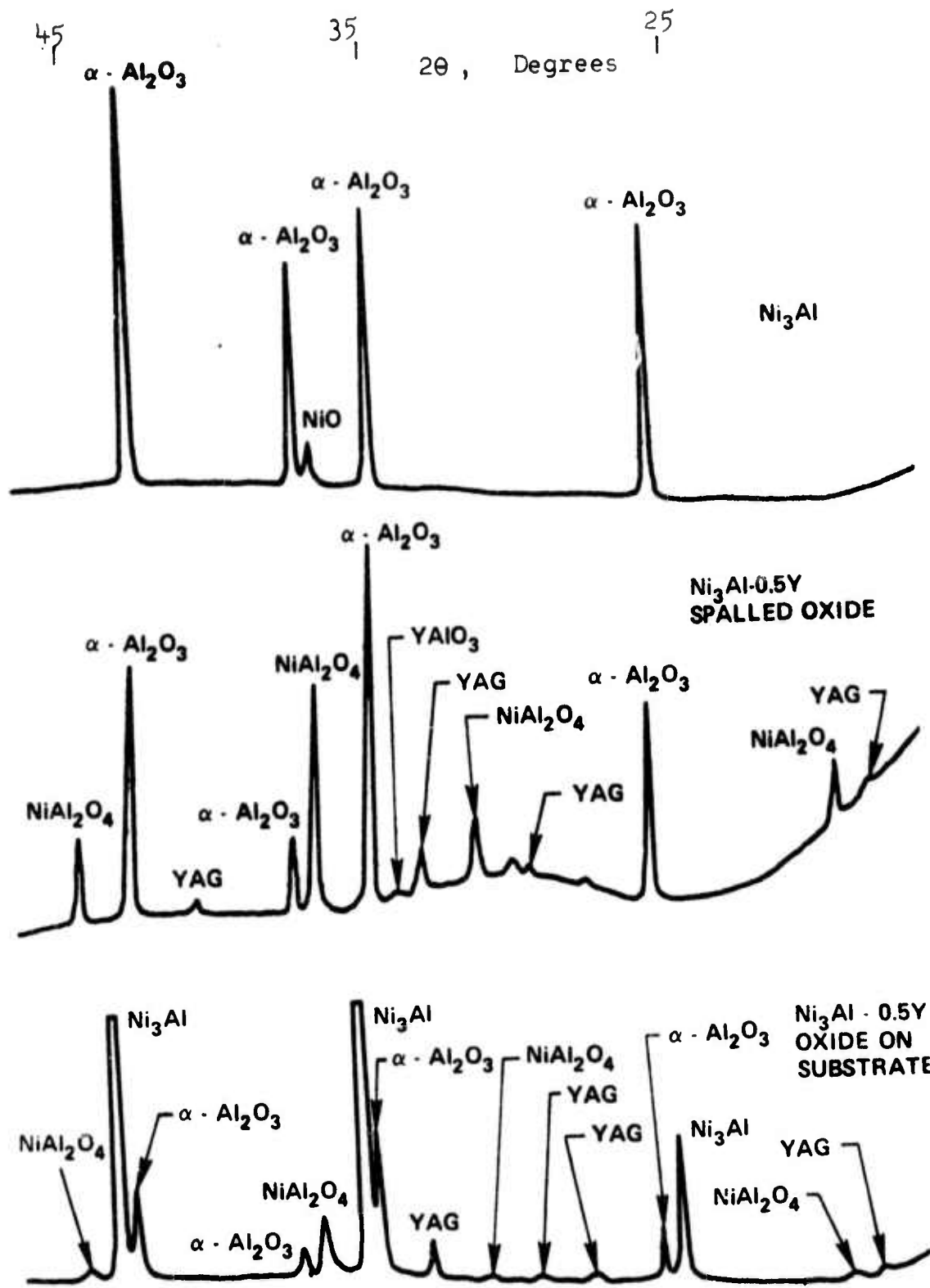


Figure 5 X-Ray Diffractometer Traces of Scales Formed on Alloys Oxidized Seven Days at 1200°C.

spalled in very small particles. Only  $\text{Al}_2\text{O}_3$  was formed on  $\text{Ni}_3\text{Al}$  at 1200°C. The weak NiO reflection was caused by its formation during cooling after the  $\text{Al}_2\text{O}_3$  layer had cracked. Contrasting the scaling behavior of  $\text{Ni}_3\text{Al}$ , where only  $\text{Al}_2\text{O}_3$  formed, was the appearance of a two-layered scale on  $\text{Ni}_3\text{Al}-0.5\text{Y}$ . All of the NiO which had formed during the initial stages was completely converted to  $\text{NiAl}_2\text{O}_4$ . Five diffraction peaks were observed for the yttrium-aluminum garnet,  $\text{Y}_3\text{Al}_5\text{O}_{12}$  (YAG). One weak peak from the distorted perovskite,  $\text{YAlO}_3$ , was detected. Slow scanning at 1/8°/min. revealed a very weak peak from  $\text{Y}_2\text{O}_3$  in the spalled outer oxide. Intensity measurements also indicated a larger percentage of YAG in the spalled oxide. This suggested that the YAG was present as discrete particles distributed throughout the  $\text{Al}_2\text{O}_3$  layer rather than as a partial or continuous layer at the  $\text{NiAl}_2\text{O}_4/\text{Al}_2\text{O}_3$  or  $\text{Al}_2\text{O}_3/\text{metal}$  interfaces.

On the basis of the spalling behavior of  $\text{Ni}_3\text{Al}-0.5\text{Y}$  at 1200°C, it was decided to determine if the remaining  $\text{Al}_2\text{O}_3$  would remain protective to further oxidation. A sample was immersed at 1200°C for two days, and an X-ray diffractometer trace was obtained from the oxides remaining intact on the substrate. The sample was reimmersed at 1200°C for an additional 200 minutes. The remaining oxides were again analyzed by diffraction methods. The diffractometer traces are illustrated in Fig. 6. The appearance of NiO after reimmersion revealed that the  $\text{Al}_2\text{O}_3$  layer was imperfect, and breaches in the film had occurred during the initial cooldown after two days.

The development of oxides on  $\text{Ni}_3\text{Al}-0.5\text{Y}$  at 900, 1100 and 1200°C was followed as a function of time using quantitative X-ray diffractometry. Fig. 7 shows the oxide development at 1200°C for periods up to four hours. The sample was used throughout the time period. It is clearly seen that almost all of the NiO was converted to spinel after four hours. The decrease in  $\text{Y}_2\text{O}_3$  intensity correlated with the appearance and increase in  $\text{YAlO}_3$  intensity. After four hours at 1200°C, a diffuse peak of YAG appeared. At the same time, it was noticed that very limited spalling of the outer spinel layer had taken place. An analysis of the diffracted intensities from the various oxides revealed that the  $\text{Al}_2\text{O}_3$  layer was increasing parabolically in thickness. Fig. 8 is a plot of log peak intensity vs. log time for the various oxides. The intensities were

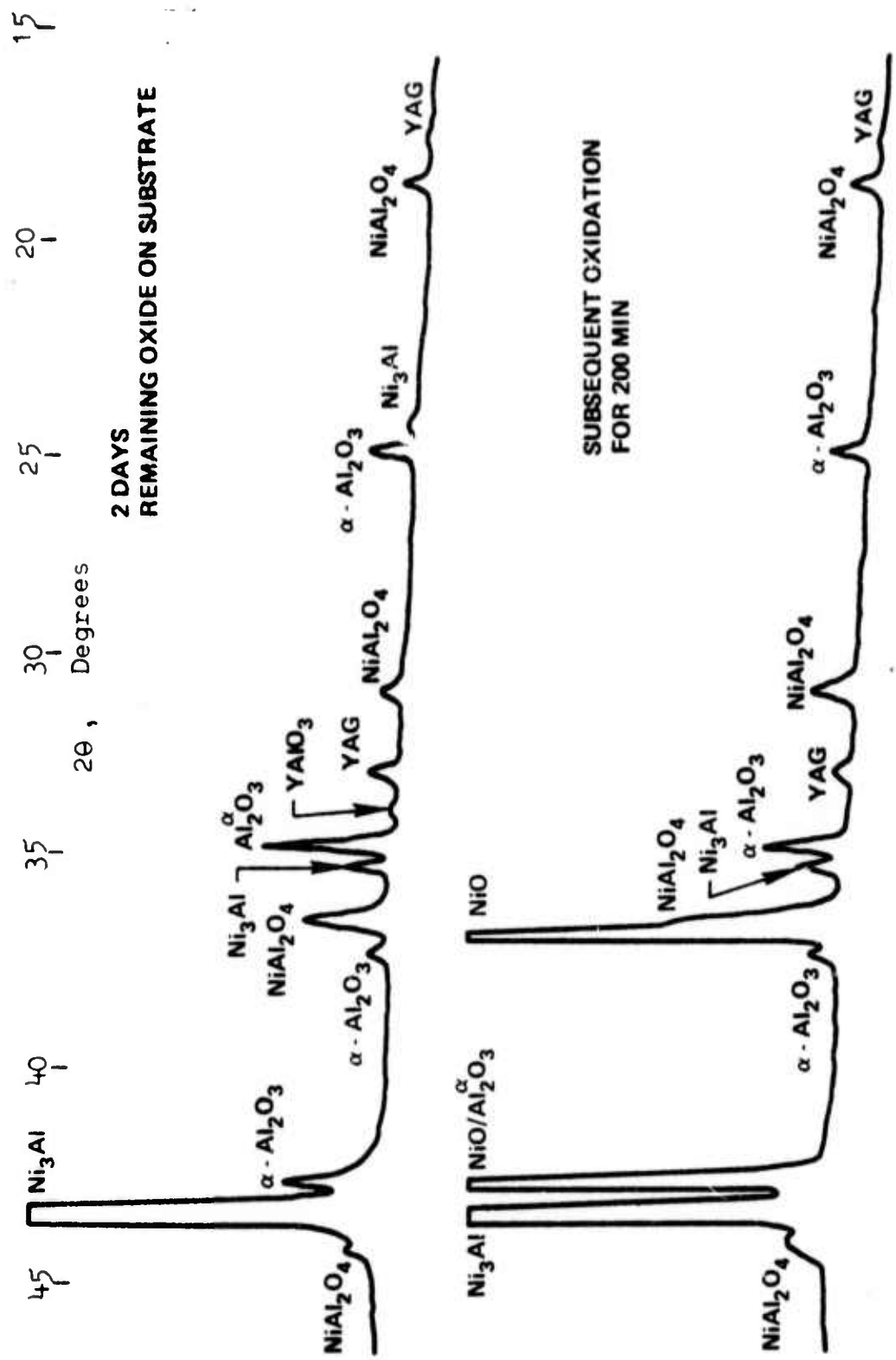


Figure 6 X-Ray Diffractometer Traces of Scales Formed on  $\text{Ni}_3\text{Al}-0.5\text{Y}$  After Subsequent Oxidation Following Spalling at  $1200^\circ\text{C}$ .

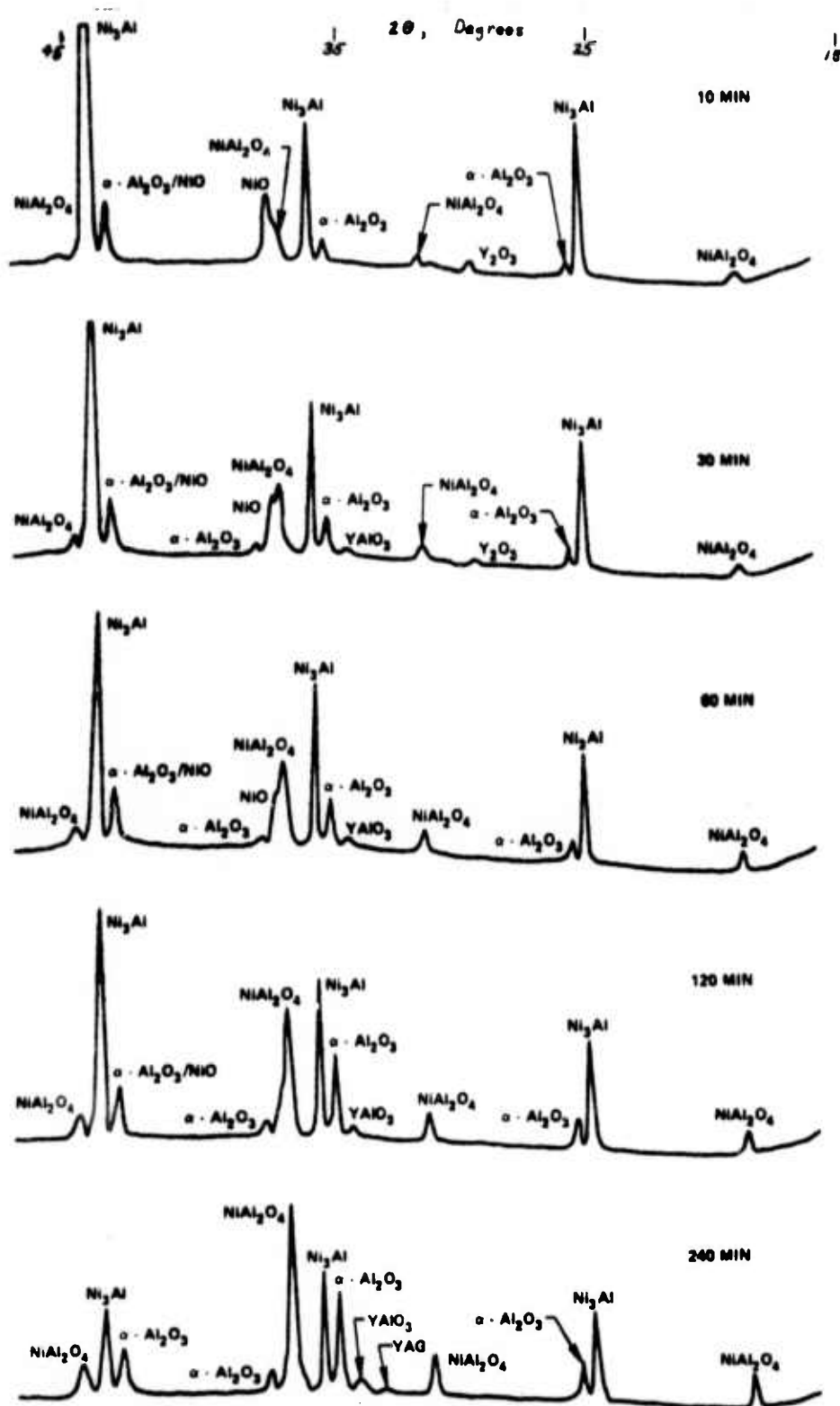


Figure 7 X-Ray Diffractometer Traces of the Scale Development on Ni<sub>3</sub>Al-0.5Y during the Transient Periods at 1200°C.

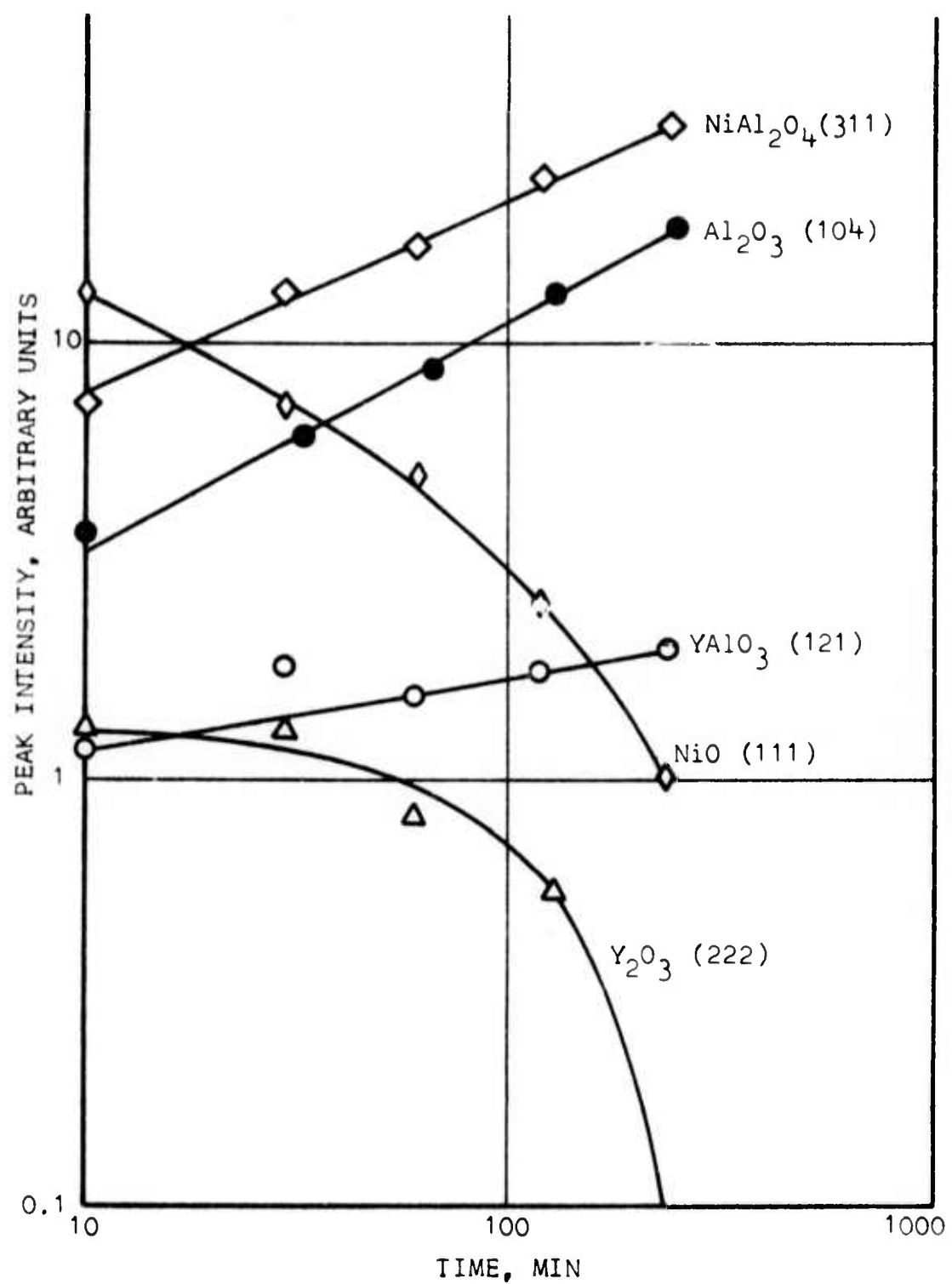


Figure 8 X-Ray Diffraction Intensities of Oxides  
Formed on  $\text{Ni}_3\text{Al}-0.5\text{Y}$  during the Transient  
Periods at  $1200^\circ\text{C}$ .

obtained by slow scanning at  $1/8^\circ/\text{min}$ . Similar measurements were performed on samples oxidized at 1100 and 900°C. Fig. 9 shows the behavior in  $\text{Al}_2\text{O}_3$  development at the lower temperatures. The intensities were converted to oxide thickness by calculating the ratio of diffracted intensity produced by a layer having thickness  $X$  to diffracted intensity of a layer having infinite thickness. Intensities were corrected for outer layer attenuation and angle of incidence of the primary X-ray beam. A summary of the procedure appears in the appendix.

The parabolic rate constants calculated from this method are compared to the steady-state rate constants obtained from the thermogravimetric data in the Arrhenius plot of Fig. 10. An activation energy of 60.6 Kcal/mole was obtained for the development of  $\text{Al}_2\text{O}_3$  scales on  $\text{Ni}_3\text{Al}-0.5\%Y$ .

### 3.1 Scanning Electron Microscopy and Electronprobe Microanalysis

#### 3.3.1 $\text{Ni}_3\text{Al}$ Base Alloy

The oxides formed on  $\text{Ni}_3\text{Al}$  at all temperatures spalled in large flakes during cooling. Oxides formed at 1200°C would readily spall after minutes of exposure, whereas, several hours at 1100°C or 1000°C or days at 900°C were required to produce the same effects. Fig. 11(a) illustrates the spalled oxide flakes remaining on the  $\text{Ni}_3\text{Al}$  substrate oxidized for two days at 1100°C. The light contrast effects on the flakes is due to varying NiO thicknesses. Regions appearing dark were analyzed as  $\text{NiAl}_2\text{O}_4$ . Small voids can be observed in the substrate. Fig. 11(b) is a higher magnification view of the highly irregular substrate appearance. The effect of large compressive stresses is noticed in Fig. 12(a), where flaking had occurred on  $\text{Ni}_3\text{Al}$  oxidized 10 minutes at 1200°C. Void formation at the alloy/oxide interface is clearly illustrated in Fig. 12(b).  $\text{Al}_2\text{O}_3$  was the only oxide detected. Higher resolution micrographs indicated that the grain size at the  $\text{Al}_2\text{O}_3/\text{gas}$  interface varied between 0.2 and  $0.4\mu$ .

A spalled flake of alumina formed on  $\text{Ni}_3\text{Al}$  for seven days at 1200°C was lifted from the substrate and fractured. Figs. 13(a) and 13(b) show the oxide surfaces at the  $\text{Al}_2\text{O}_3/\text{gas}$  and metal/ $\text{Al}_2\text{O}_3$  interfaces, respectively. The filamentary protrusions in Fig. 13(a) were analyzed as  $\text{Al}_2\text{O}_3$ . The outer surface grain diameter was approximately  $0.6\mu$ . The underside of the film, Fig. 13(b), illustrates numerous voids. The grain diameters (2 to  $4\mu$ ) at this interface were considerably larger than those of Fig. 13(a).

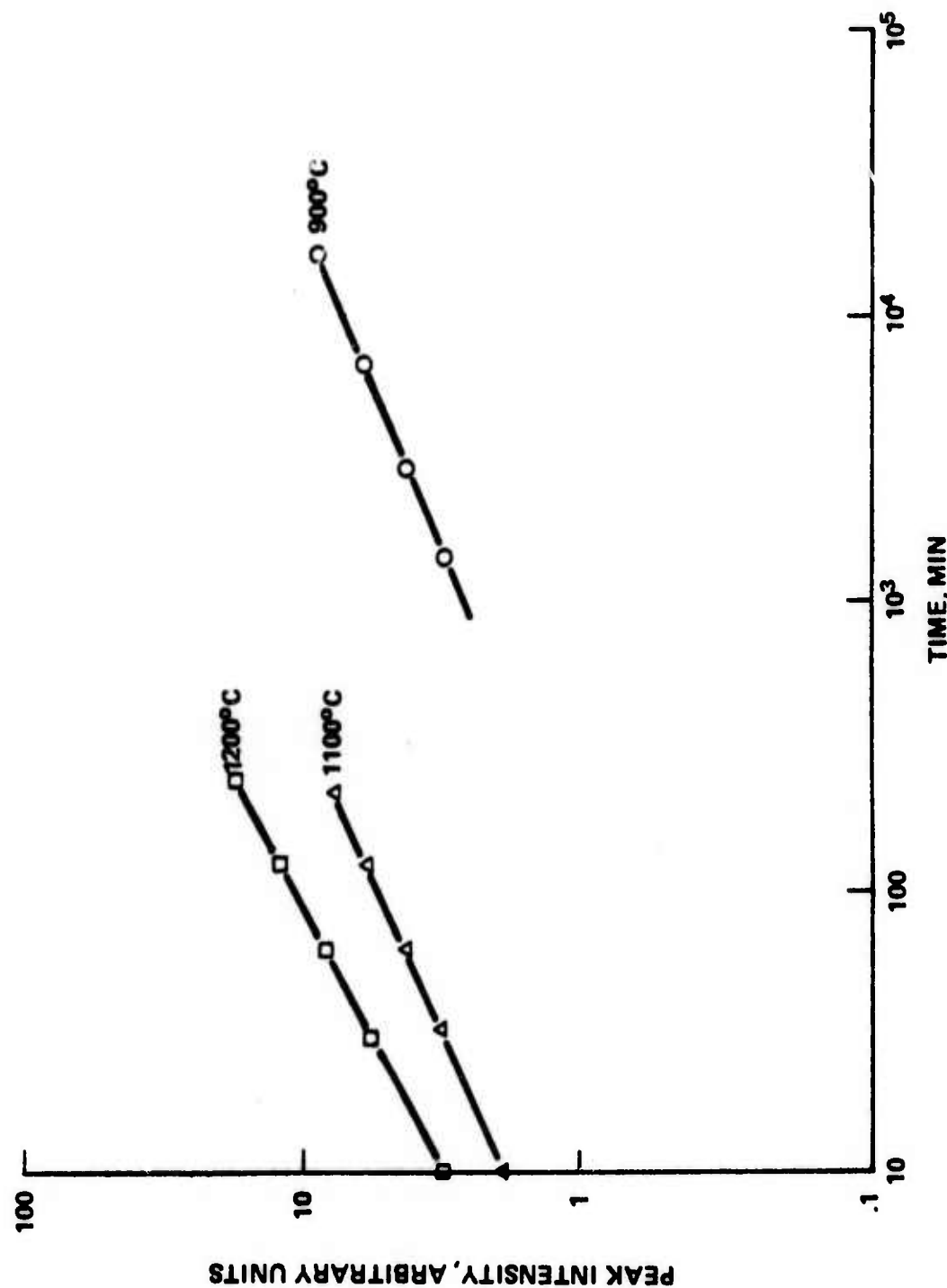


Figure 9 Isothermal Oxidation Kinetics of  $\alpha$ - $\text{Al}_2\text{O}_3$  on  $\text{Ni}_3\text{Al}-0.5\text{Y}$  from 900 to 1200°C as Measured by X-Ray Diffraction Intensities.

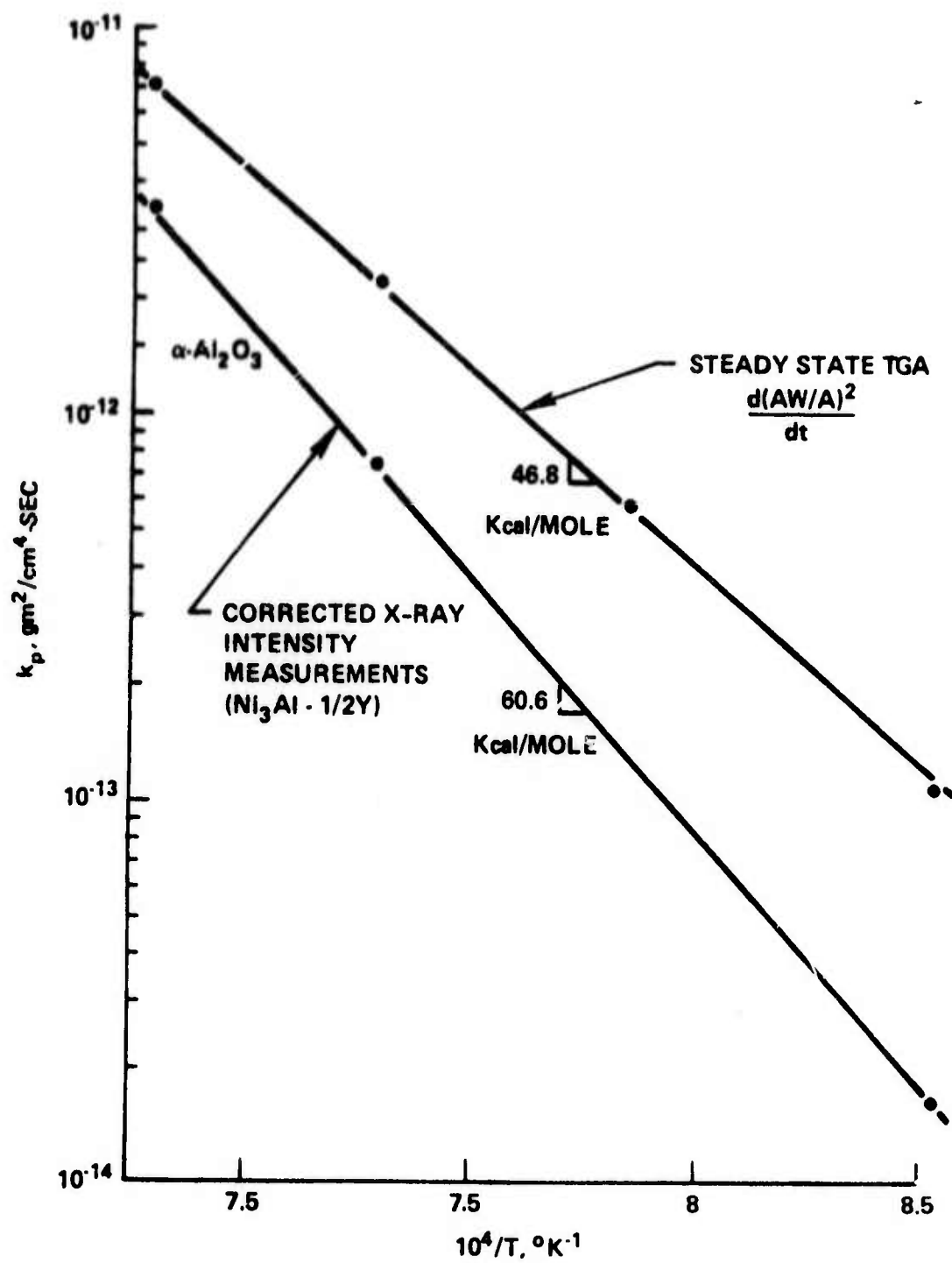
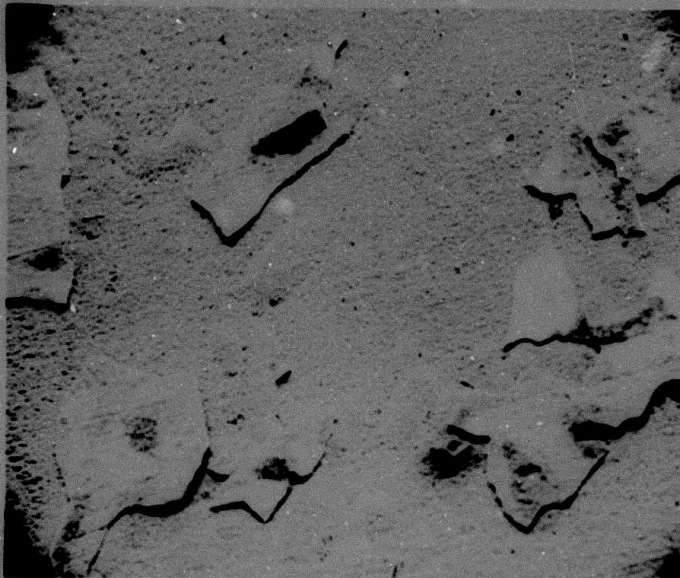
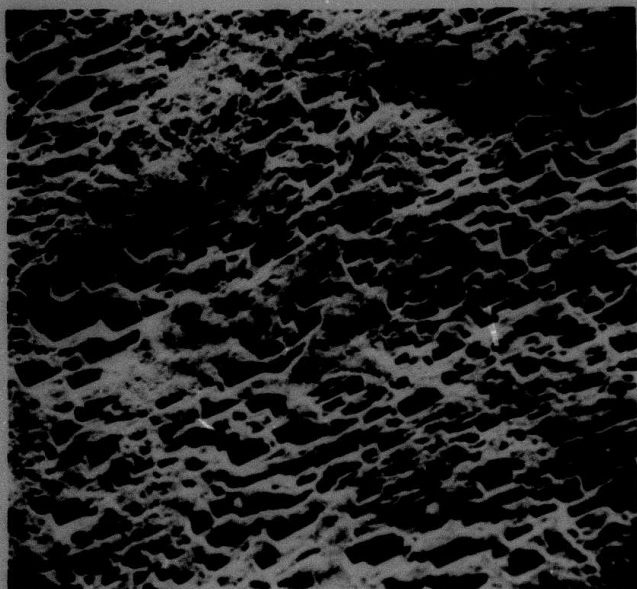


Figure 10 Temperature Dependence of  $\alpha\text{-Al}_2\text{O}_3$  Formation on  $\text{Ni}_3\text{Al}-0.5\text{Y}$  from 900 to 1200°C.



(a)



(b)

Figure 11 Spalled Oxides on Ni<sub>3</sub>Al after 2 Days  
Oxidation in Air at 1000°C.  
(a) Oxides, 200X, (b) Substrate, 2000X.  
Surface Tilted 35° from Electron Beam.

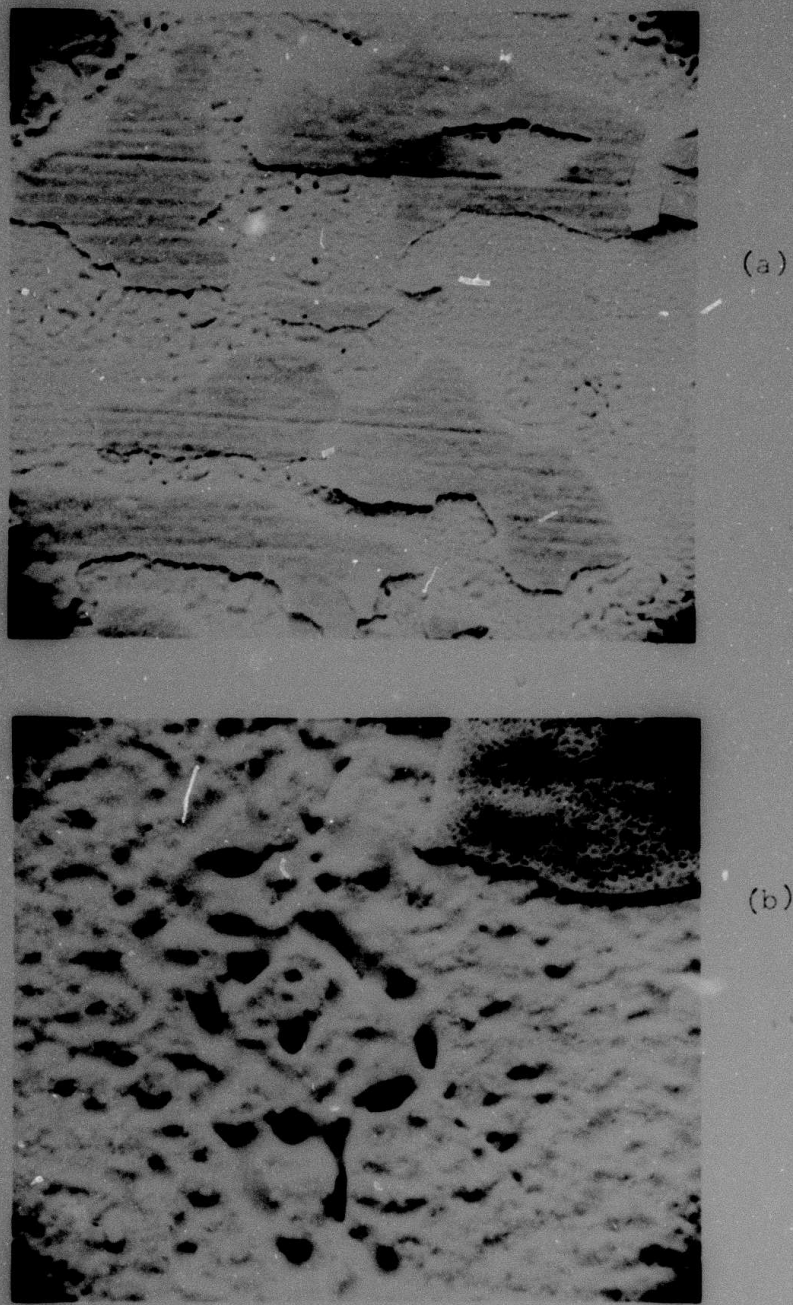


Figure 12 Failure of Alumina Film on Ni<sub>3</sub>Al After 10 Min. Oxidation at 1200°C. (a) 500X, (b) 2000X. Surface Tilted 35° from Electron Beam.

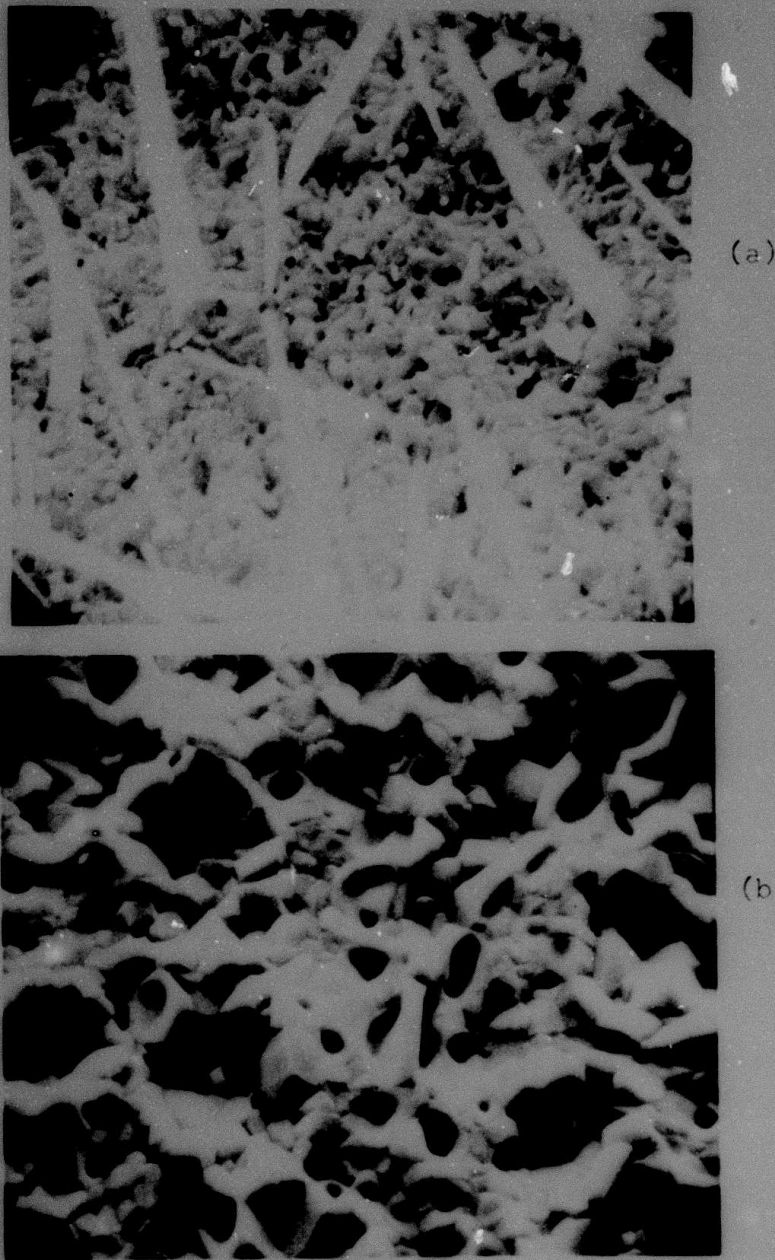


Figure 13. Typical Morphologies of the Spalled Alumina Film Formed on  $\text{Ni}_3\text{Al}$  after 7 Days Oxidation at  $1200^\circ\text{C}$  in Air. (a)  $\text{Al}_2\text{O}_3$ /Gas Interface, 5000X, (b)  $\text{Al}_2\text{O}_3$ /Substrate Interface, 1850X.  $30^\circ$  Tilt from Beam.

A cross-section of the fractured oxide appears in Fig. 14. A higher resolution micrograph of the cross-section shows the filament's base and small voids within the  $\text{Al}_2\text{O}_3$  film, Fig. 15.

### 3.3.2 $\text{Ni}_3\text{Al}$ Containing 0.5% Yttrium

The adherent scale formed on  $\text{Ni}_3\text{Al}-0.5\%\text{Y}$  after two days' oxidation at  $1000^\circ\text{C}$  appears in Fig. 16. The grain boundaries of the underlying substrate are delineated by oxide that appears to protrude from the surface. Concentration profiles across the grain boundary oxide of Fig. 16(b) are shown in Fig. 17. The oxide above the grain boundary was  $\text{NiAl}_2\text{O}_4$ , whereas the adjacent surface oxide was composed of small  $\text{NiO}$  crystallites. Significant concentrations of yttrium were not observed on the outer scale surfaces. A plan view of the adherent scale formed on  $\text{Ni}_3\text{Al}-0.5\%\text{Y}$  oxidized two days at  $1100^\circ\text{C}$ , Fig. 18, was similar to that formed at  $1000^\circ\text{C}$ , Fig. 16(a). A larger fraction of  $\text{NiO}$  had been converted to  $\text{NiAl}_2\text{O}_4$ .

During the study of oxide development on  $\text{Ni}_3\text{Al}-0.5\%\text{Y}$ , it was mentioned earlier (Section 3.2) that localized spalling occurred after four hours exposure at  $1200^\circ\text{C}$ . The surface of the sample used for diffraction analysis was examined in the SEM to determine the nature of spalling. The regions of scale failure would lie within a circular area having a  $50\mu$  diameter. The region in Fig. 19 was typical. Concentration profiles through the area, Fig. 20, revealed yttrium and aluminum enrichment in the particle and stringer. The surface oxide next to the spalled region was predominately spinel with some unconverted  $\text{NiO}$  present. An analysis of the X-ray intensity emitted when the electron beam was positioned directly on the particle and stringer indicated they were primarily YAG. The adjacent substrate area, although somewhat irregular, did not show evidence of void formation.

Extensive spalling was observed after a sample of  $\text{Ni}_3\text{Al}-0.5\%\text{Y}$  had been oxidized for seven days at  $1200^\circ\text{C}$ . Numerous particles protruded from the substrate. Fig. 21 illustrates one such particle. Energy line scans indicated the particle was YAG, Fig. 22. Void formation in the substrate was absent. The substrate topography in Fig. 23 reveals only the oxide imprints after the scale detached. The small ( $< 1000\text{\AA}$ ) particulate matter was most likely due to contamination effects.

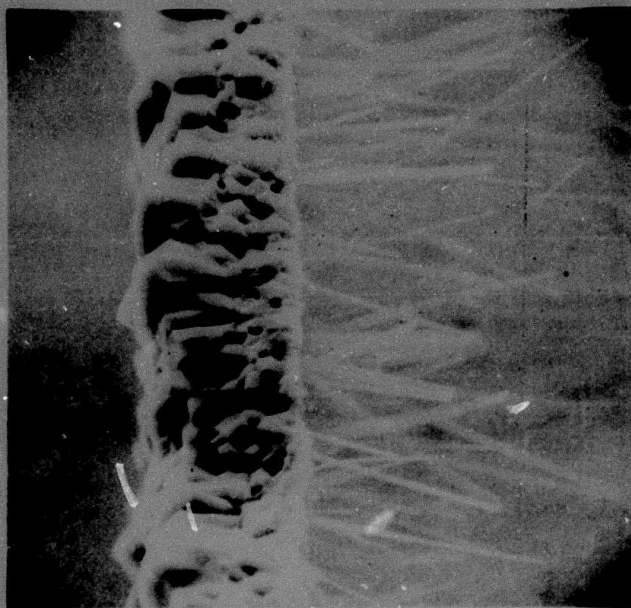


Figure 14. Cross-section of the Fractured  $\text{Al}_2\text{O}_3$  Film  
Formed for 7 days on  $\text{Ni}_3\text{Al}$  at  $1200^\circ\text{C}$  in Air.  
1900X.

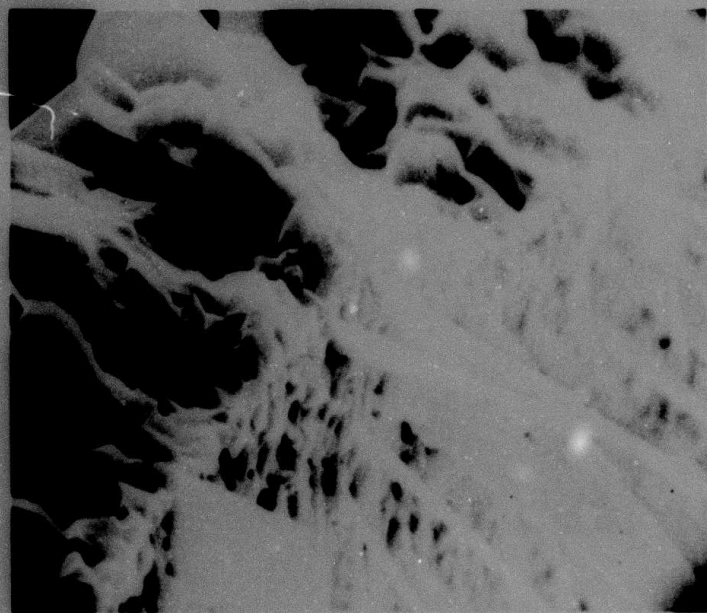
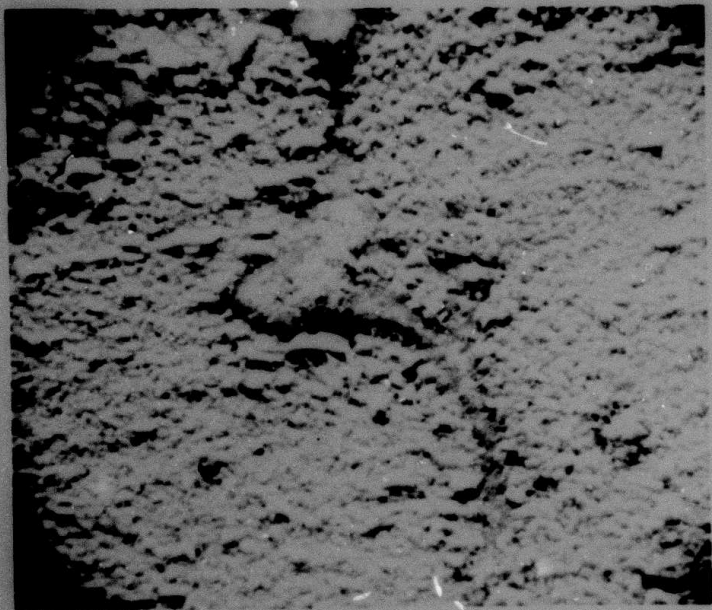


Figure 15 Outer Edge of the Cross-section Appearing  
in Figure 19. 5000X.



(a)



(b)

Figure 16. Adherent Scale Formed on  $\text{Ni}_3\text{Al}-0.5\%\text{Y}$  after  
2 Days Oxidation at  $1000^\circ\text{C}$  in Air.  
(a) 400X, (b) Grain Boundary Oxide, 2000X.

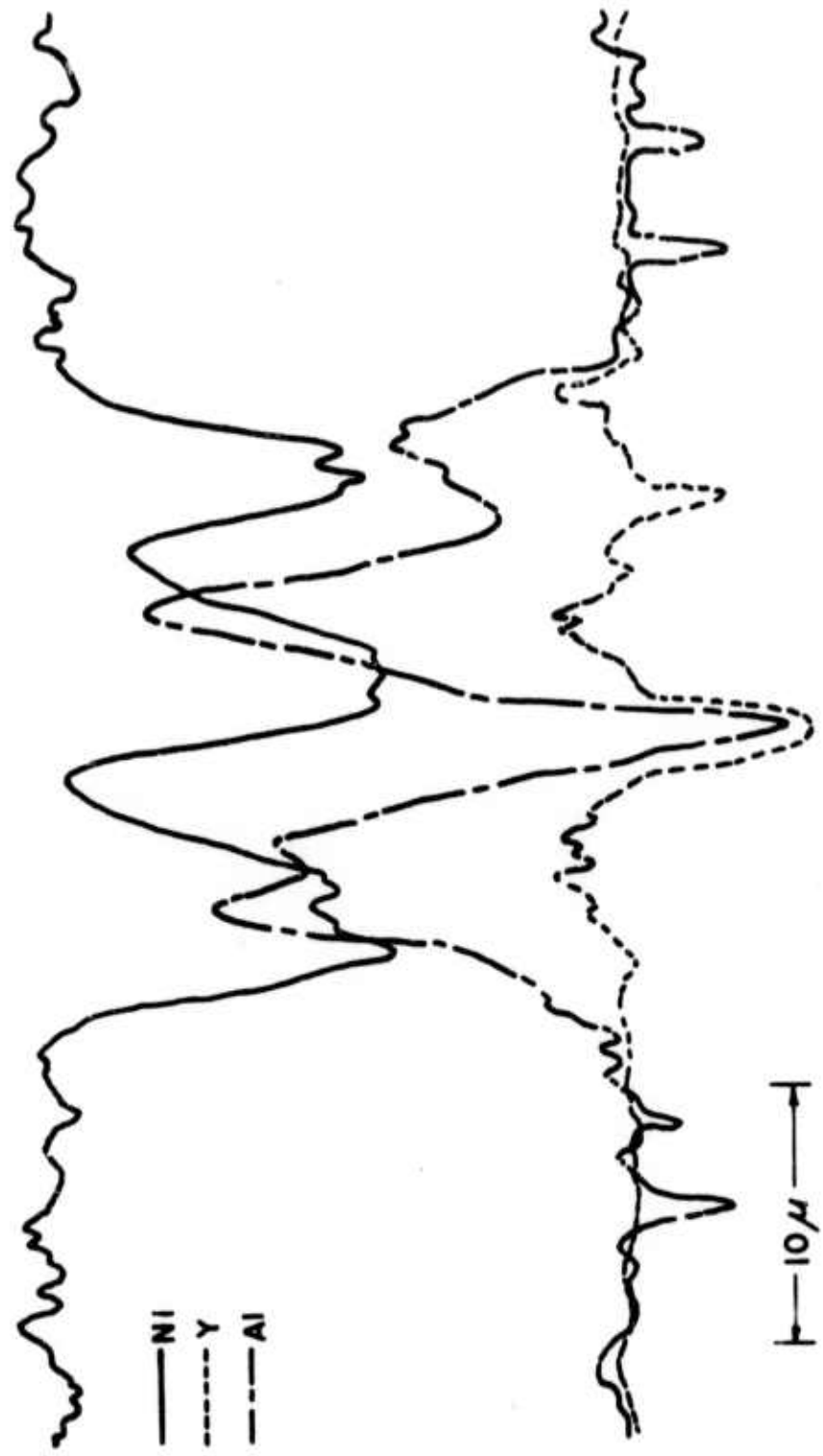


Figure 17 Concentration Profiles Across the Grain Boundary Area of Figure 21 (b).

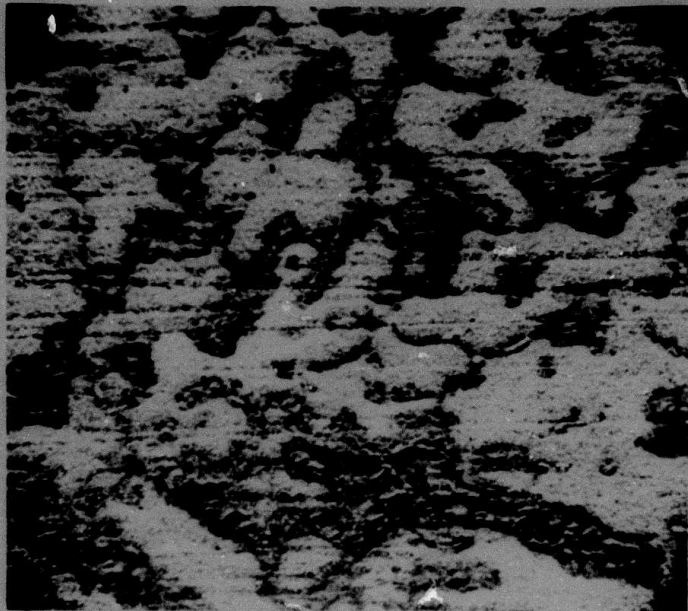


Figure 18 Plan View of the Adherent Oxides Formed on  
Ni<sub>3</sub>Al-0.5%Y Oxidized 2 Days at 1100°C in Air.  
400X.

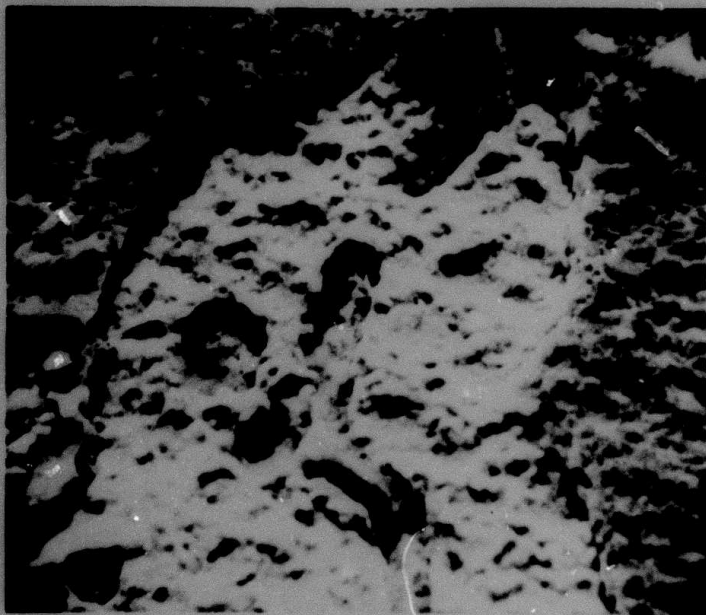


Figure 19 Localized Scale Failure on Ni<sub>3</sub>Al-0.5%Y  
Following Oxidation at 1200°C for 4 Hours  
in Air. 2000X. 35° Tilt from Beam.

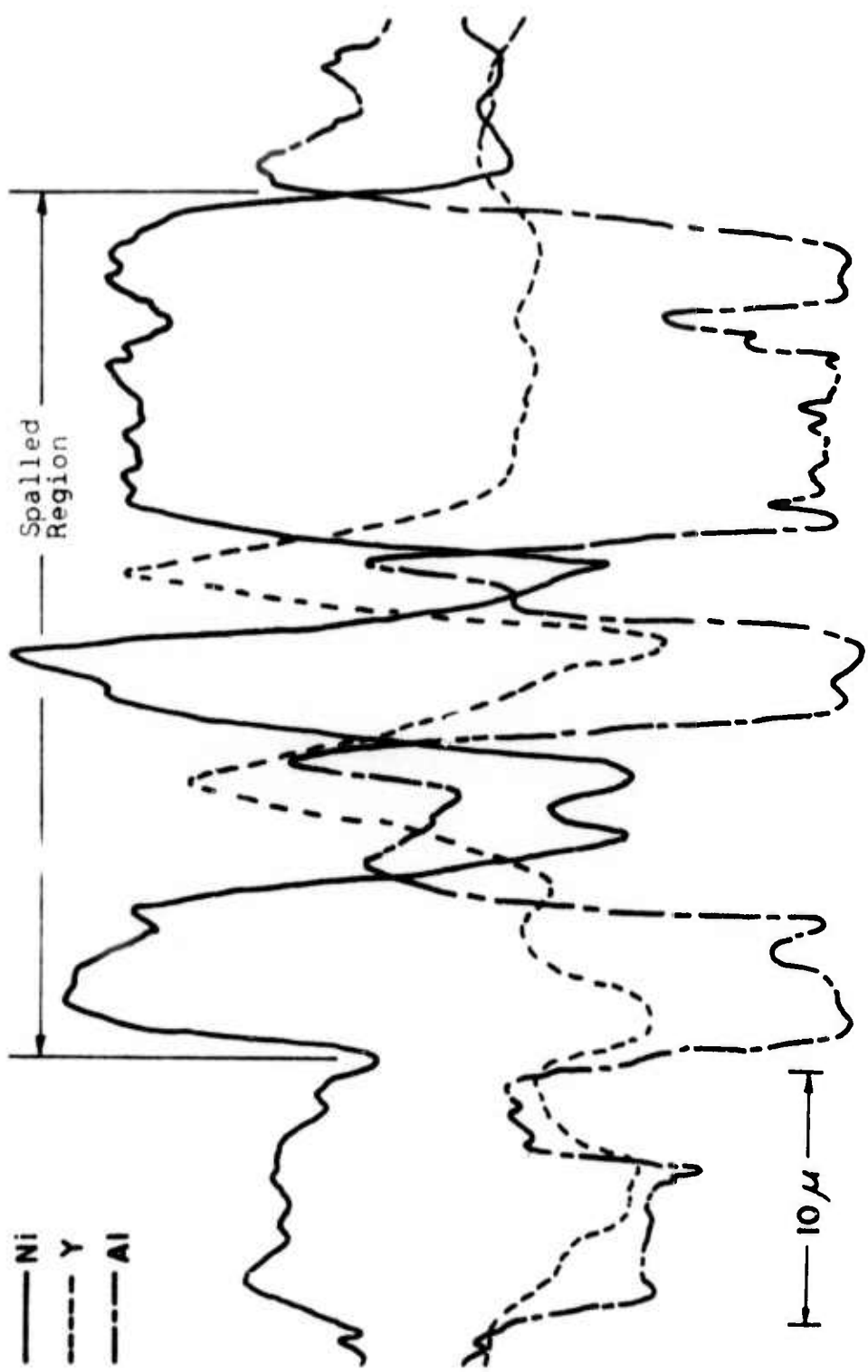


Figure 20 Concentration profiles through the Spalled Area of Figure 24.

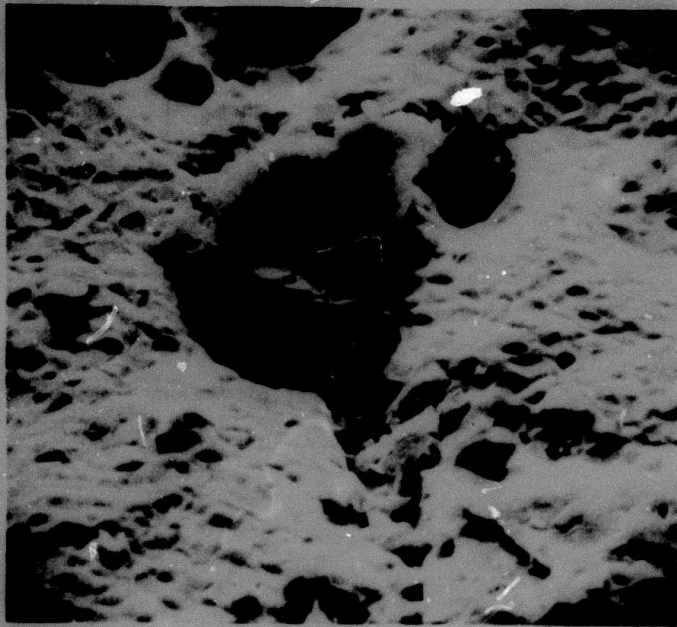


Figure 21 Typical Particle Protruding from the Spalled Surface of Ni<sub>3</sub>Al-0.5%Y after 7 Days Oxidation at 1200°C in Air. 2000X.

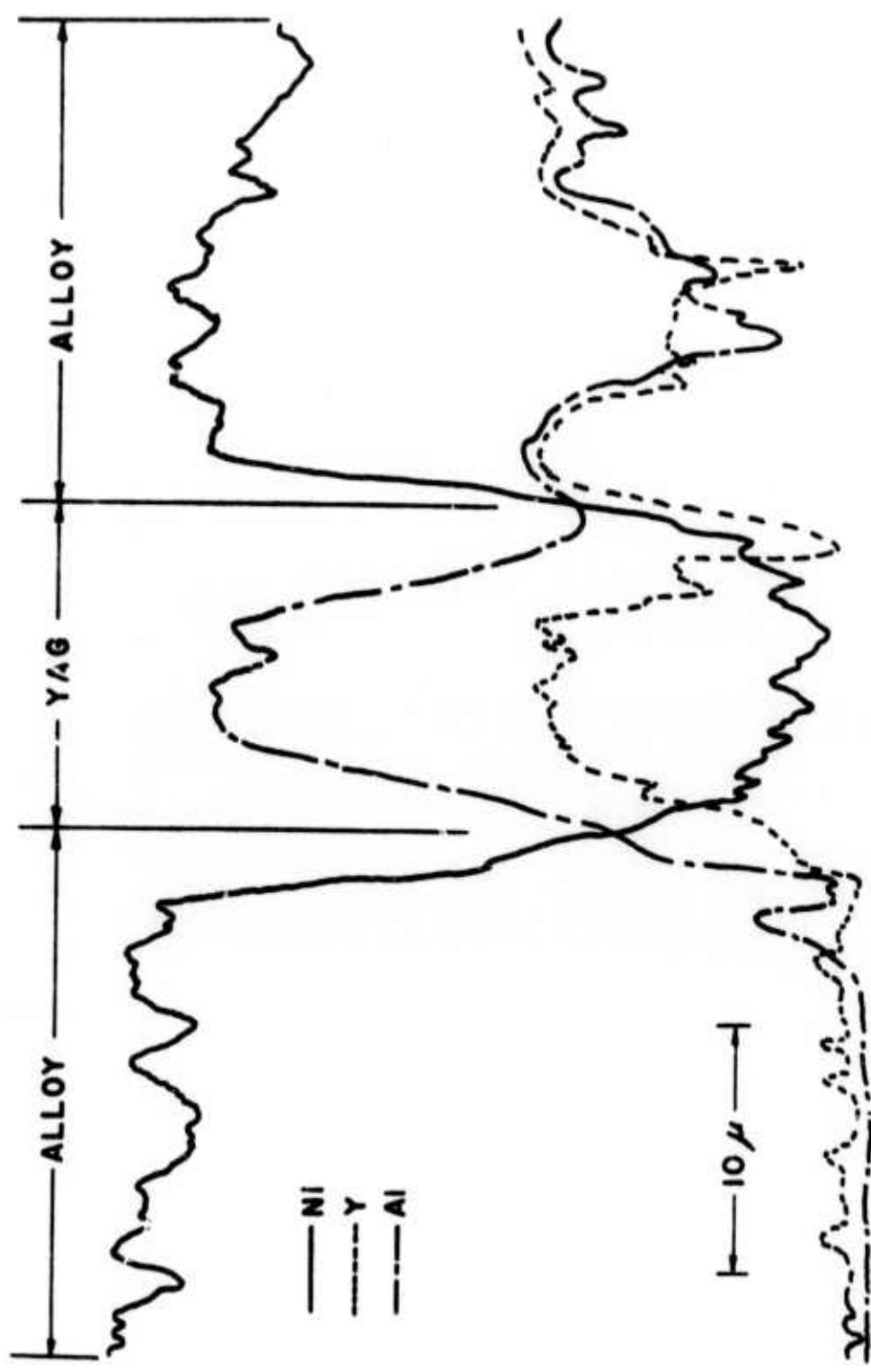


Figure 22 Concentration Profiles Through the Particle of Figure 26.

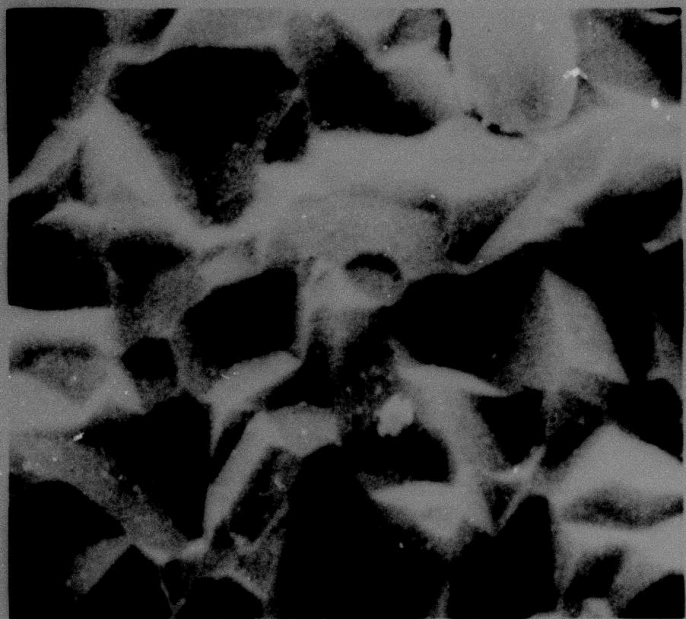


Figure 23 Substrate Topography on  $\text{Ni}_3\text{Al}-0.5\%\text{Y}$  after Scale Failure. 10,000X.

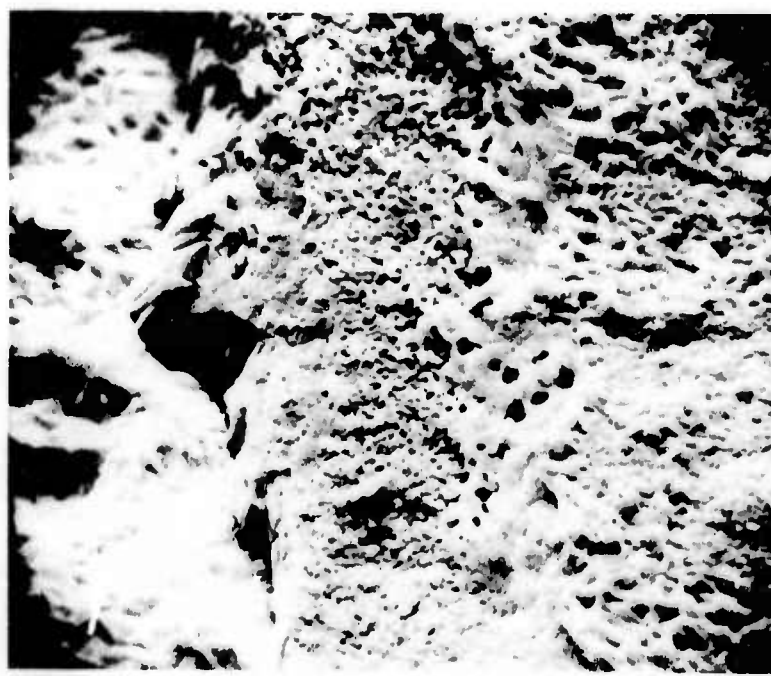


Figure 24 Composite Scale Formed on Ni<sub>3</sub>Al-0.5%Y Oxidized for 7 Days at 1200°C in Air. 1900X.

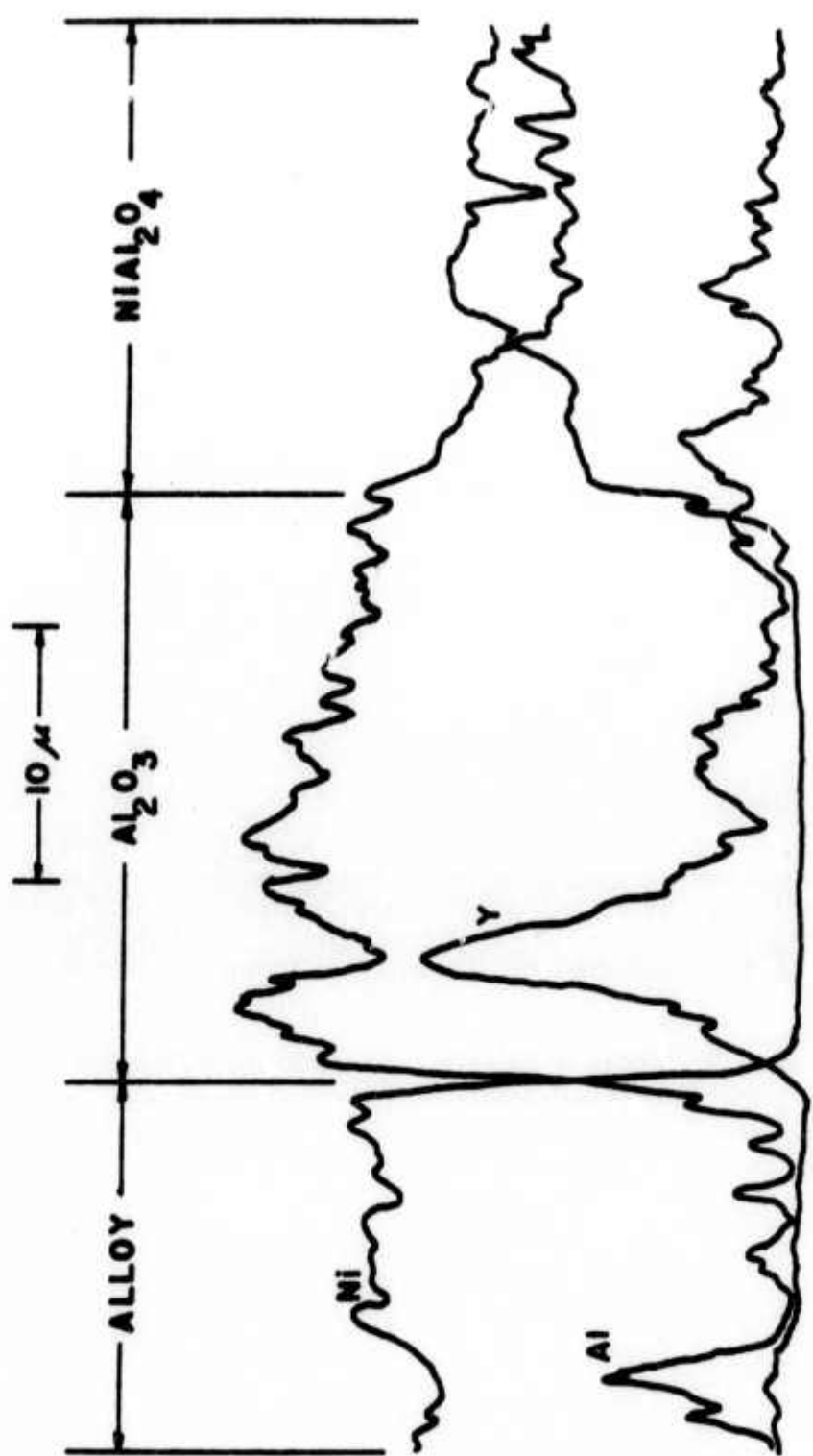


Figure 25 Concentration Profiles Through the Area Indicated in Figure 24.

Concentration profiles (Fig. 25) were obtained through an area of composite scale that remained on the substrate (Fig. 24). The two-layered scale consisting of an inner  $\text{Al}_2\text{O}_3$  and outer  $\text{NiAl}_2\text{O}_4$  layer is indicated. An area rich in yttrium was revealed within the  $\text{Al}_2\text{O}_3$  layer. The fine-grained outer surface of  $\text{Al}_2\text{O}_3$  is evident.

The substrate of a similar sample ( $1200^\circ\text{C}$ , seven days) was dissolved in a 10% bromine-methanol solution. An intact portion of the composite oxide scale was examined for structural detail. Fig. 26 reveals the composite scale morphology of a fractured section. The columnar  $\text{Al}_2\text{O}_3$  grains are clearly illustrated as is the fine-grain structure apparent at the  $\text{Al}_2\text{O}_3/\text{NiAl}_2\text{O}_4$  interface. No voids were observable in the  $\text{Al}_2\text{O}_3$  layer at higher resolution although some cavity formation is evident in the spinel layer.

#### 4. DISCUSSION

##### 4.1 Effect of Yttrium on the Scaling Behavior of $\text{Ni}_3\text{Al}$

The addition of 0.5%Y to  $\text{Ni}_3\text{Al}$  did not significantly alter the oxidation kinetics. Although weight gains 10 to 20% higher were observed, the steady-state scaling rates were identical. A comparison of scales formed on the two alloys oxidized at  $1200^\circ\text{C}$  for seven days offers an explanation for the higher weight gains (Figs. 14 and 24). Only  $\text{Al}_2\text{O}_3$  was formed on  $\text{Ni}_3\text{Al}$ . A composite  $\text{Al}_2\text{O}_3/\text{NiAl}_2\text{O}_4$  scale on  $\text{Ni}_3\text{Al}-0.5\%$ Y resulted from the solid-state reaction of  $\text{NiO}$  and  $\text{Al}_2\text{O}_3$ . Nickel enrichment in the surface layers was caused by Ni-Y intermetallic decomposition during the early stages of oxidation. The aluminum content at the surface was effectively lowered below that required for exclusive selective oxidation, but greater than that required for internal oxidation. The aluminum content of the base alloy,  $\text{Ni}_3\text{Al}$ , was greater than that required for exclusive selective oxidation. The effect of yttrium in the enhancement of spinel formation has not been conclusively demonstrated in past investigations.

It has been variously reported that spinel layers are beneficial<sup>(2)</sup> ( $\text{NiCr}_2\text{O}_4$  on Ni-Cr alloys), and that they are detrimental<sup>(3)</sup> ( $\text{CoCr}_2\text{O}_4$  on Co-Cr alloys). The presence of  $\text{NiAl}_2\text{O}_4$  on  $\text{Ni}_3\text{Al}$  did not alter the oxidation rate. The similar oxidation rate constants for both alloys indicated the rate-controlling transport mode was diffusion through  $\text{Al}_2\text{O}_3$ . Tien and

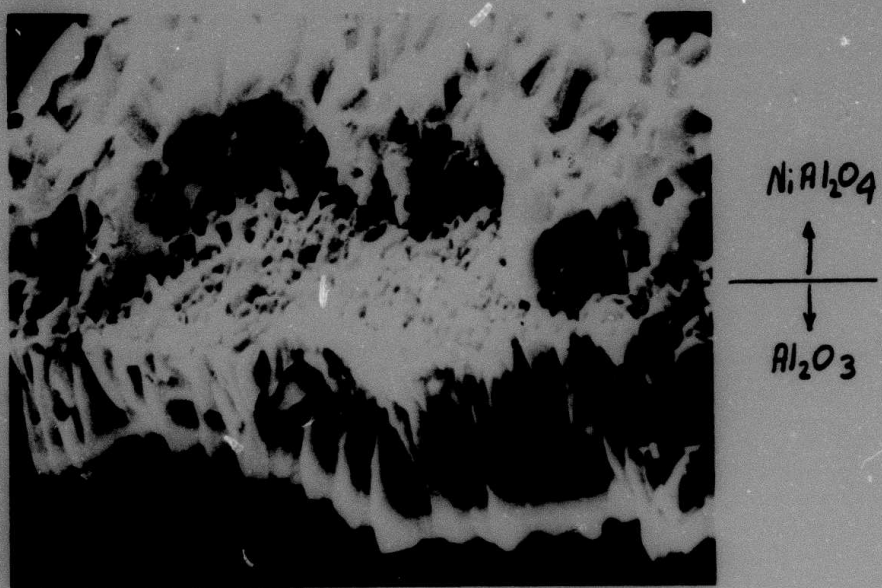


Figure 26 Scale Morphology of the Scale Formed on  $\text{Ni}_3\text{Al}-0.5\%\text{Y}$  after 7 Days Oxidation at  $1200^\circ\text{C}$  in Air. 3000X.

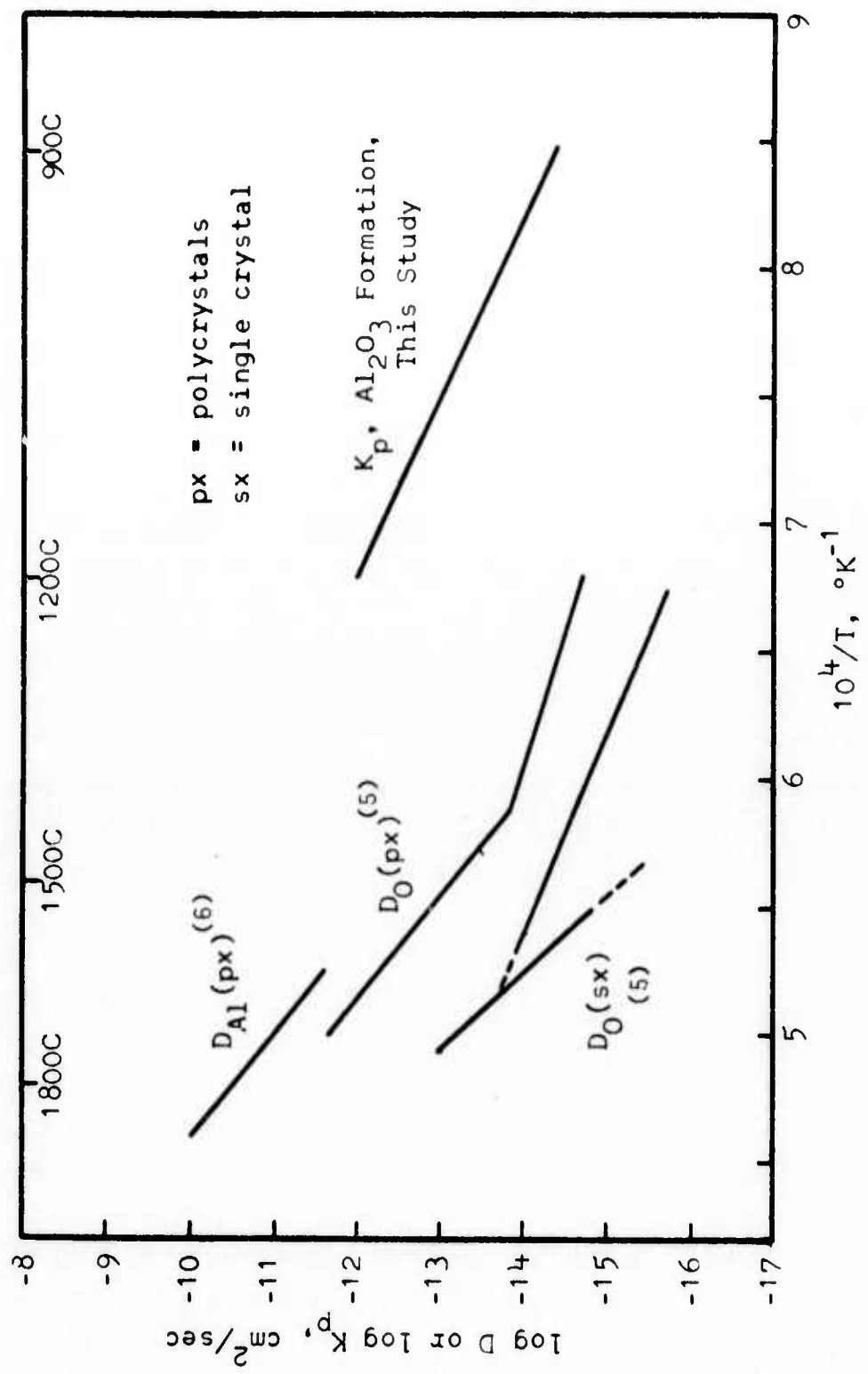


Figure 27 Temperature Dependence of Diffusional Processes in  $\text{Al}_2\text{O}_3$ .

Pettit<sup>(4)</sup> have indicated that alumina formed on FeCrAlY alloys by inward anion diffusion. Inert platinum markers placed on the alloy surface prior to oxidation were found at the oxide/gas interface after exposure. Tien and Pettit<sup>(4)</sup> assumed oxygen diffused along the  $\text{Al}_2\text{O}_3$  grain boundaries.

The yttrium-rich particles protruding from the substrate of  $\text{Ni}_3\text{Al}-0.5\% \text{Y}$  oxidized seven days at 1200°C offer direct evidence of inward oxygen diffusion (Fig. 21). The anomalous behavior of artificial markers is circumvented by observing the positions of natural markers such as the yttrium-rich particles. If aluminum cation diffusion were rate-controlling, the particles should have been located at the alloy/oxide interface. The measured parabolic growth of  $\text{Al}_2\text{O}_3$  on  $\text{Ni}_3\text{Al}-0.5\% \text{Y}$  allows a mechanistic interpretation of the transport mechanism. Fig. 27 compares the oxidation rate constants for alumina formation of this study with the measured oxygen and aluminum ion self-diffusion coefficients in  $\text{Al}_2\text{O}_3$ . It is clearly seen that extrapolation of the high temperature data will result in erroneous conclusions. Oishi and Kingery's<sup>(5)</sup> oxygen diffusion coefficients were sensitive to impurities and structural effects. Above 1600°C, a two-order magnitude increase in the oxygen diffusion coefficient was reported for polycrystalline  $\text{Al}_2\text{O}_3$  (30μ grain size) vs. single crystal alumina. Below 1600°C (1450°C for polycrystals), it was suggested that diffusion was impurity and/or structurally controlled.<sup>(5)</sup> Paladino and Kingery's results<sup>(6)</sup> on aluminum-ion diffusion gave no evidence of enhanced grain-boundary diffusion. Creep and sintering rates<sup>(7-10)</sup> of fine (2μ) and coarse-grained (100μ)  $\text{Al}_2\text{O}_3$  occurred at a faster rate than possible for the lattice diffusion of oxygen to be rate-controlling. The calculated diffusion coefficients indicated that bulk aluminum ion-diffusion was rate-controlling. From the results of present and past studies, it is concluded that the enhanced grain-boundary diffusion of oxygen controls the oxidation rate of alloys forming  $\text{Al}_2\text{O}_3$  scales between the temperatures of 900 and 1300°C. An extrapolation of this mechanism to lower temperatures is not warranted.

The scales formed on both alloys at lower temperatures (900-1100°C) were similar. The selective oxidation rate of aluminum was decreased to an extent that  $\text{NiO}$  formed during the initial stages of the reaction. The subsequent reaction of  $\text{NiO}$  and  $\text{Al}_2\text{O}_3$  to form  $\text{NiAl}_2\text{O}_4$  did not occur uniformly over the sample surface. The adherent scales on  $\text{Ni}_3\text{Al}-0.5\% \text{Y}$  formed for two days at 1000°C (Fig. 18) showed grain boundary delineation by

$\text{NiAl}_2\text{O}_4$ . The grain boundary spinel appeared thicker than adjacent oxides within the grain, Fig. 16(b). At 1100°C, the spinel covered a larger portion of the surface, but appeared to progress laterally from the boundary into the center of the grain. With sufficient time, the entire surface would be covered with spinel. It is significant that the alloys were still in a "transient" mode of scale development after two days exposure. Samples of the base alloy,  $\text{Ni}_3\text{Al}$ , exhibited steady-state kinetic behavior sooner than those containing 0.5%Y. This indicated that more  $\text{NiO}$  was formed on  $\text{Ni}_3\text{Al}$ -0.5%Y at lower temperatures, and that transport through  $\text{Al}_2\text{O}_3$  governed the overall oxidation rate.

The early appearance of spinel in the grain boundaries is expected if the rate of forming a complete layer of  $\text{Al}_2\text{O}_3$  is slow. The alloy grain boundaries offer high diffusivity paths for aluminum;  $\text{Al}_2\text{O}_3$  formation is enhanced in the grain boundary surface. Wood and Chattopadhyay<sup>(11)</sup> have noticed this effect with Ni-Al alloys oxidized at 600°C. There is every reason to expect similar behavior at higher temperatures but with faster reaction rates.

The steady-state reaction rate constants are compared to Pettit's<sup>(12)</sup> results in the Arrhenius Plot of Fig. 28. The absence of an inversion in reaction rate for the alloys of this study (13.2% Al) clearly illustrates that 13.2% Al is above that required for internal oxidation at all temperatures. This agrees with Wood and Stott's<sup>(13)</sup> results on Ni-12.5% Al. The parabolic rate constants for  $\text{Al}_2\text{O}_3$  formation on Ni-13.2% Al-0.5%Y of this study are in excellent agreement with Pettit's<sup>(12)</sup> results for Ni-25% Al where  $\text{Al}_2\text{O}_3$  was the only oxide formed at all temperatures.

The filamentary protrusions growing from the outer alumina surface (Fig. 15) were approximately 5000Å wide at their base. The thickness was smaller than the microscope resolution, i.e., less than about 400Å. The average density was about  $10^6/\text{cm}^2$ . This amounted to a surface coverage of only 0.02%. The whiskers most likely grew by a cation diffusion mechanism. Fischmeister<sup>(14)</sup> has indicated that dislocation pipe-diffusion may be a likely mechanism. The overall kinetics might be affected by whisker growth if a phase-boundary reaction at the oxide/gas interface is rate-controlling. Numerous other mechanisms<sup>(15)</sup> have been proposed. It suffices to state

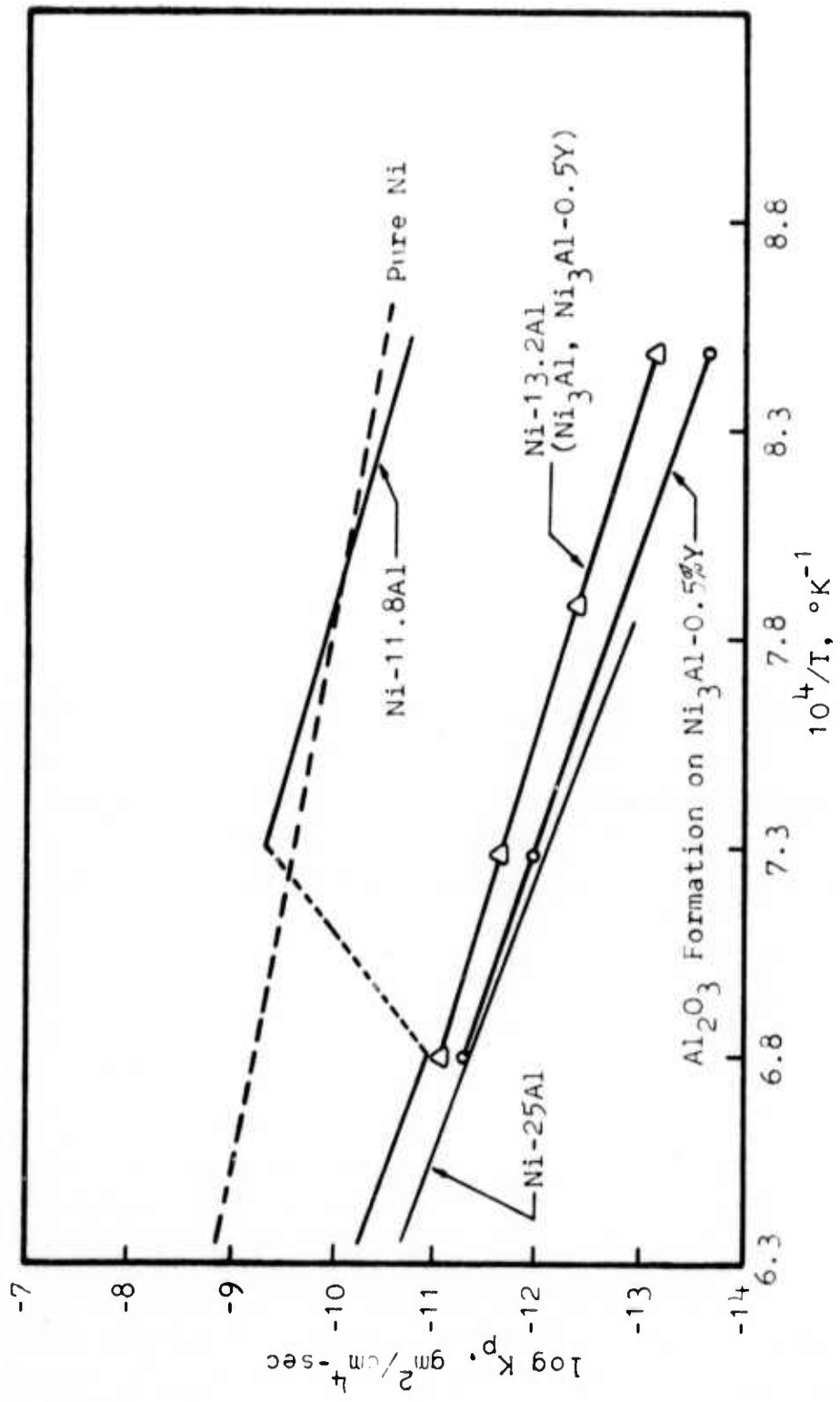


Figure 28 Arrhenius Plot Comparing the Oxidation Kinetics of Ni<sub>3</sub>Al with the Results of Pettit. (12)

that the growth of  $\text{Al}_2\text{O}_3$  filaments was an interesting side effect of the oxidation process and did not influence the overall reaction kinetics.

#### 4.2 Mechanisms of Spallation and Scale Adherence

The scales formed on  $\text{Ni}_3\text{Al}$  spalled extensively during cooling from the test temperatures. This effect was evident after minutes at 1200°C, while several days exposure at 900°C were required to produce the same behavior. In every instance, numerous voids were observed at the alloy/oxide interface. The voids were replicated in the underside of an  $\text{Al}_2\text{O}_3$  film formed for seven days at 1200°C.

A marked but short-term improvement in the scale adherence was observed with  $\text{Ni}_3\text{Al}$  containing 0.5%Y. Voids in the substrate were absent under all oxidizing conditions. Limited spallation was observed after four hours at 1200°C. At the same time, X-ray diffraction techniques revealed the presence of yttrium-aluminum garnet,  $\text{Y}_3\text{Al}_5\text{O}_{12}$  (YAG), in the surface layers. The localized regions of film failure, Fig. 19, were always associated with yttrium-rich particles and stringers. Extensive spallation occurred on samples oxidized for seven days at 1200°C. Numerous YAG particles were observed to protrude from the substrate.

Scale failure on  $\text{Ni}_3\text{Al}$  was characterized by the detachment of large flakes, whereas, the scale on  $\text{Ni}_3\text{Al}-0.5\%$ Y spalled in minute particles. These results indicated that the mechanisms of spallation were different on each alloy.

Dilatational strains during cooling produced failure on both alloys. An approximate magnitude of the stress generated in the  $\text{Al}_2\text{O}_3$  film may be calculated from<sup>(16)</sup>

$$\sigma_{\text{ox}} = \frac{E_{\text{ox}} \Delta T (\alpha_{\text{ox}} - \alpha_m)}{1 + 2 \frac{E_{\text{ox}}}{E_m} \left( \frac{t_{\text{ox}}}{t_m} \right)} \quad (1)$$

where,  $\sigma_{\text{ox}}$  = the stress in the oxide

$E_{\text{ox}}$  = elastic modulus of the scale

$E_m$  = elastic modulus of the metal

$t_{ox}$  = oxide thickness

$t_m$  = metal thickness

$\alpha_{ox}$  = oxide coefficient of thermal expansion

$\alpha_m$  = metal coefficient of thermal expansion

$\Delta T$  = temperature change

A compressive stress of about 350,000 psi is created on cooling from 1200°C. Data used in this calculation are found in Table 1. An upper limit for the ultimate compressive strength of bulk polycrystalline  $Al_2O_3$  is about 300,000 psi.<sup>(17)</sup> Douglass<sup>(16)</sup> has pointed out that a comparison of bulk oxide properties with those of thin films should be viewed with caution. Although some plastic flow in the substrate may reduce the dilational stress, the fact remains that the stresses generated during cooling are enormous. The fracture stress of thermally grown, thin  $Al_2O_3$  films is probably above 300,000 psi; the scales form on  $Ni_3Al-0.5\%Y$  did not spall until four hours exposure at 1200°C.

It is suggested that the voids observed in the  $Ni_3Al$  substrates acted as stress concentrators. On cooling, the stress was elevated above the adherence strength (adherence strength is used rather than fracture strength as there were no indications that fracture was initiated within the  $Al_2O_3$  films). Once the localized separation occurred at a void, the detachment of large oxide flakes resulted. The absence of voids in the  $Ni_3Al-0.5\%Y$  substrates indicated that the cause of separation was the large YAG particles. It is suggested that the physical size of the YAG particles act as stress concentrators within the  $Al_2O_3$  film. The YAG particles are the result of a series of solid-state reactions between  $Y_2O_3$  and  $Al_2O_3$ . The transition of states required to form the YAG is discussed in detail in Section 4.3. A crack initiated in either the YAG particle or in the adjacent  $Al_2O_3$  propagates along the alloy/oxide interface and through the  $Al_2O_3$  film. The combined process of shearing YAG particles and alloy/oxide detachment causes the scale to spall in small particles.

TABLE 1  
Miscellaneous Mechanical and Thermal Property Data

Elastic Modulus $10^6$ psi	Coefficient of Thermal Expansion $10^{-6} \text{ }^\circ\text{C}^{-1}$	Reference
$\text{Al}_2\text{O}_3$ , 50		17
$\text{Al}_2\text{O}_2$ , 9.0		31
YAG, 8.0-9.0		32
$\text{Ni}_3\text{Al}$ , 13.7		33

The various mechanisms that have been proposed for the increase in adherence are critically reviewed. The favored "key-on" effect<sup>(18-21)</sup> is not convincing. This mechanism cannot account for the absence of voids at the alloy/oxide interface. This study has shown that the rare earth particles protruding from the substrate actually can cause film spallation.

Thin layers of  $Y_2O_3$  or  $YAlO_3$ , etc., could not be detected under any conditions. It is difficult to conceive how such a layer could form. Yttrium is effectively localized in the matrix as Ni-Y intermetallics or as  $Y_2O_3$ . The low solubility and expected slow diffusion coefficients of yttrium in solution could not allow the formation of such a layer during the time when the adherence effects are noticed, i.e., 10 mins. at 1200°C.

Arguments based on increased  $Al_2O_3$  plasticity resulting from yttrium incorporation in the growing film are not adequate.<sup>(22)</sup> Alumina is strengthened by the presence of impurities. Radford and Pratt<sup>(23)</sup> doped  $Al_2O_3$  single crystals with 300 to 400 ppm Fe, Mg, Ti and Ni. The temperature for the onset of plasticity in pure  $Al_2O_3$  was about 1200°C. The flow stress was increased by a factor of three and up to a factor of about thirty for Fe and Mg dopants, respectively. The incorporation of yttrium in  $Al_2O_3$  should have the effect of retarding high temperature deformation processes. Furthermore, a lack of plasticity is indicated by the persistence of a very-fine grain structure at the outer side of the  $Al_2O_3$  film formed on both alloys. The grain size increased from  $0.3\mu$  to  $0.6\mu$  over a period of seven days at 1200°C.

The vacancy sink concept originally proposed by Stringer<sup>(24)</sup> is the only plausible mechanism for increasing scale adherence. Tien and Pettit<sup>(4)</sup> verified Stringer's proposal with FeCrAl alloys containing yttrium and scandium. The adherence effects appeared to occur at reactive metal concentration levels above and below the solubility limits in the matrix. It was proposed that the voids at the alloy/oxide interface were eliminated by two effects. The large reactive metal atoms in solution formed atom-vacancy complexes with excess vacancies and the internal "rare-earth" oxides provided vacancy sinks. They did not identify the source of vacancies that condensed to produce the voids. It was suggested that the excess vacancies were associated with the selective oxidation of aluminum.

The mechanism of transport through  $\text{Al}_2\text{O}_3$ , i.e., oxygen grain-boundary diffusion, cannot account for void formation in the substrate. A model is proposed to account for the creation of voids at the alloy/oxide interface. Two cases are considered:

1. Exclusive selective oxidation of aluminum,
2.  $\text{Al}_2\text{O}_3$  formation after  $\text{NiO}$  establishes a complete layer.

For the purposes of illustration, the original substrate interface will not be treated as a moving boundary.

Fig. 29 illustrates the diffusional processes occurring in the alloy during the selective oxidation of aluminum.  $N_{\text{Al}}^B$  and  $N_{\text{Ni}}^B$  refer to the bulk alloy compositions. The selective oxidation process results in aluminum depletion and nickel enrichment at the alloy/oxide interface, Fig. 29(b). The back diffusion of nickel occurs at a greater rate than the migration of aluminum to the surface, Fig. 29(d). A flux balance requires a net flow of vacancies to the surface, as in Fig. 29(e). The dislocation arrays in the matrix and grain boundaries may act as sinks for some of the vacancies.<sup>(25)</sup> If the degree of supersaturation is not relieved by an internal matrix sink mechanism, the vacancies coalesce and condense as small voids. These voids will serve as effective sinks for subsequent vacancy fluxes. The voids grow to a size where they become effective stress concentrators during athermal conditions.

Fig. 30 illustrates the manner in which voids form at lower temperatures, i.e., where the initial formation of  $\text{NiO}$  is followed by the development of an  $\text{Al}_2\text{O}_3$  layer. The formation of  $\text{NiO}$  results in nickel depletion and aluminum enrichment, Fig. 30(b). The final development of an  $\text{Al}_2\text{O}_3$  layer drastically alters the atom fluxes. Aluminum is being depleted while the nickel concentration is increasing at the alloy/oxide interface, Fig. 30(c). Voids will eventually develop after the vacancy flux exceeds the saturation limit.

It is expected that the voids will take longer to develop at the lower temperatures; the size and distribution should occur on a smaller scale than at high temperatures. These characteristics were observed in the present study.

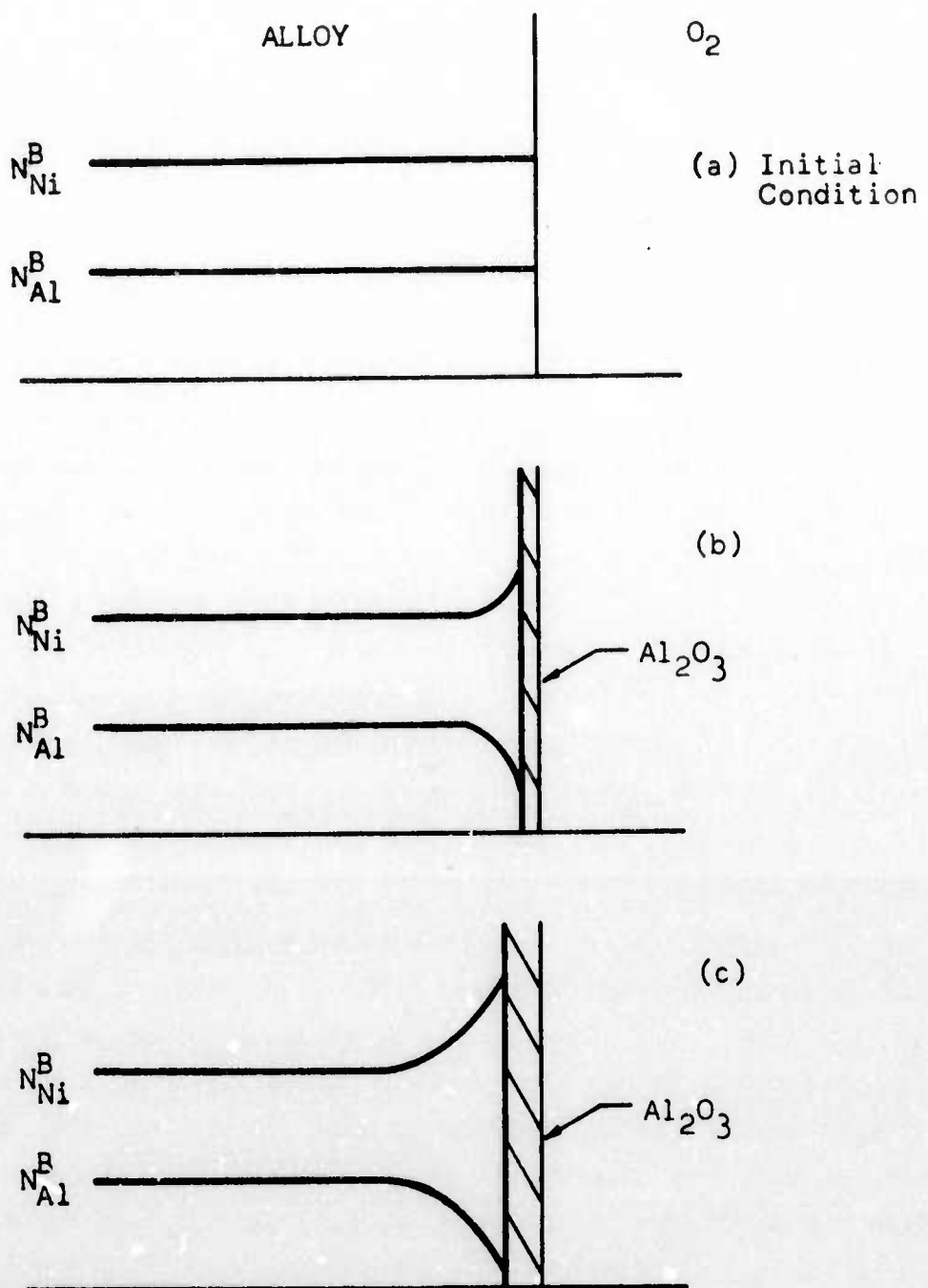


Figure 29 Diffusional Characteristics in  $\text{Ni}_3\text{Al}$  During the Selective Oxidation of Aluminum.

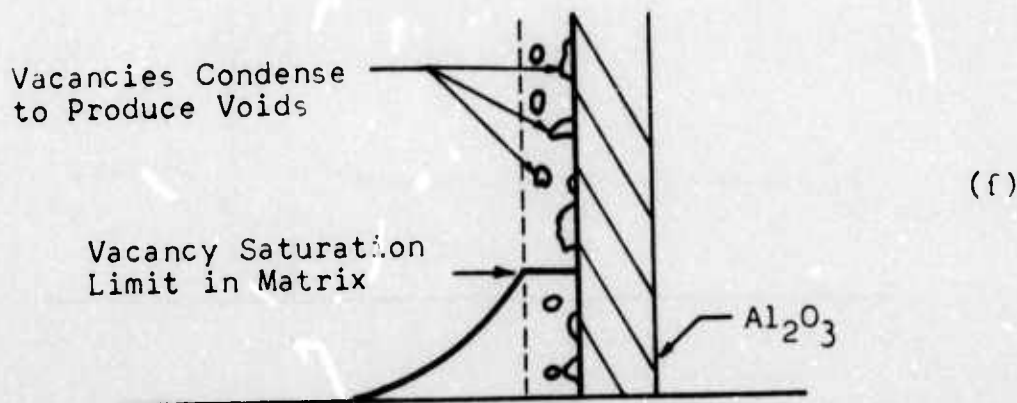
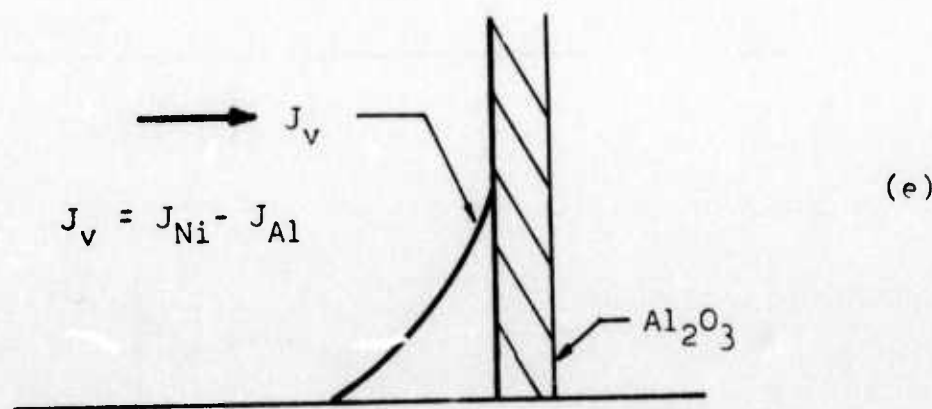
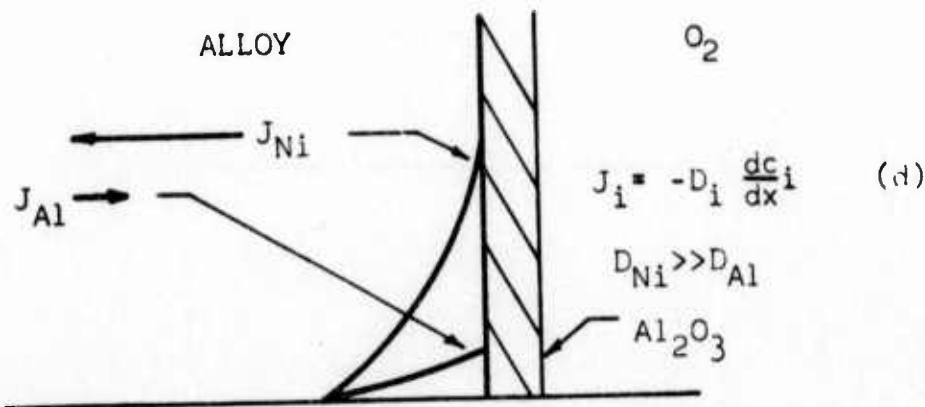


Figure 29 (continued).

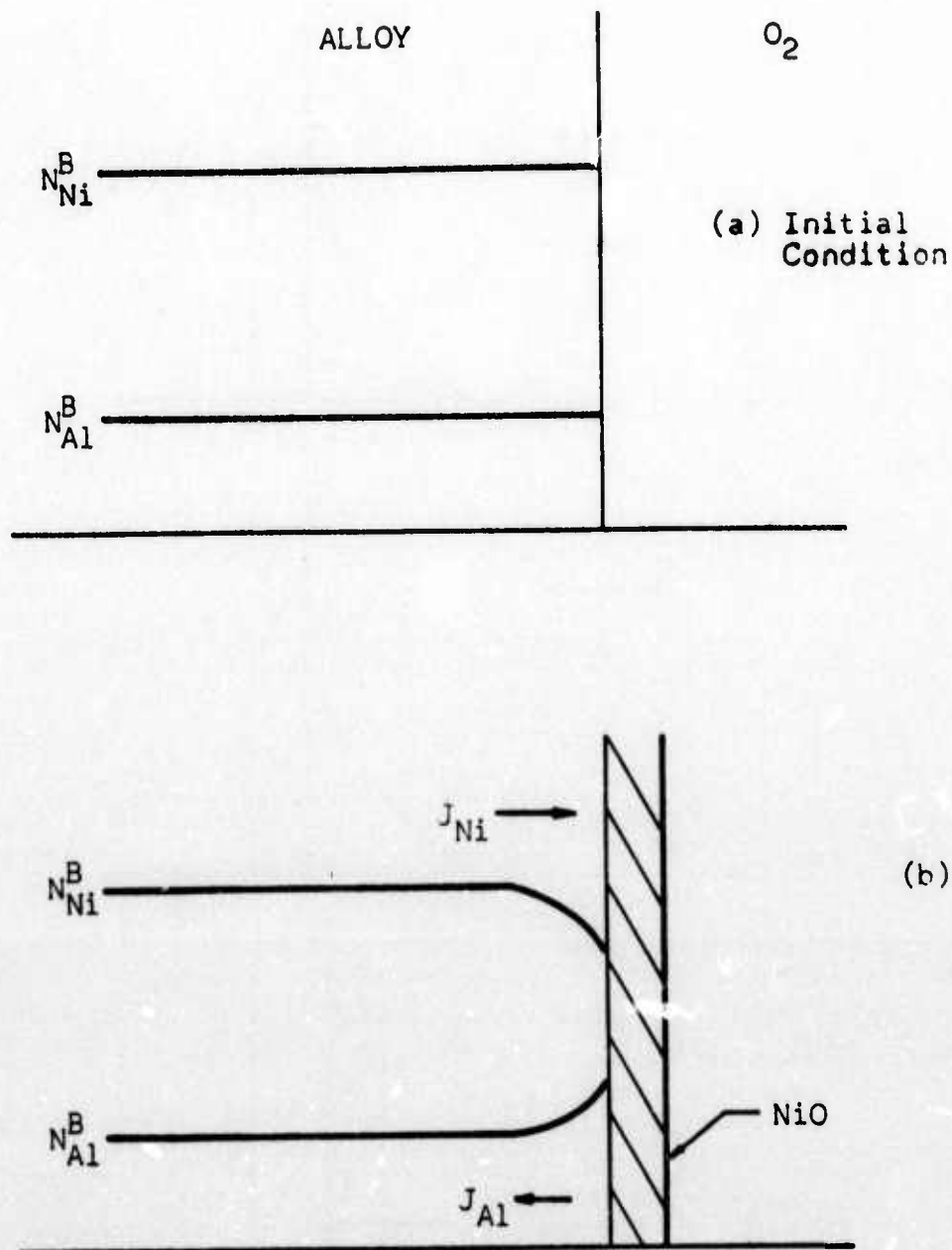


Figure 30 Mechanism of Void Production in  $Ni_3Al$  at Lower Temperatures.

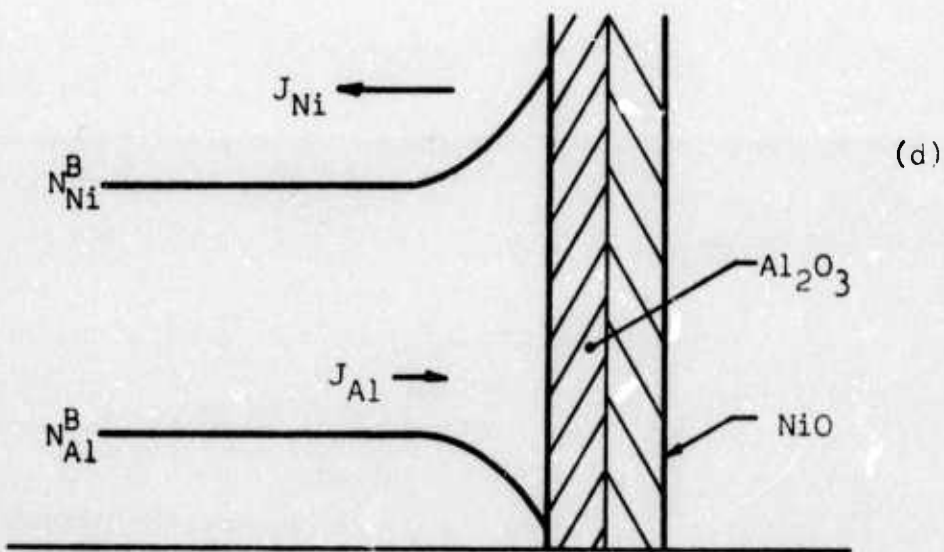
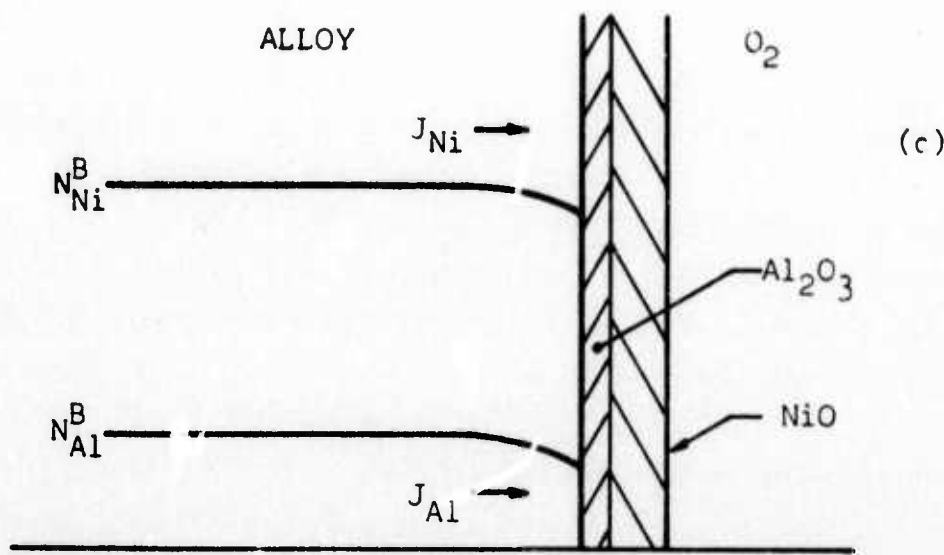
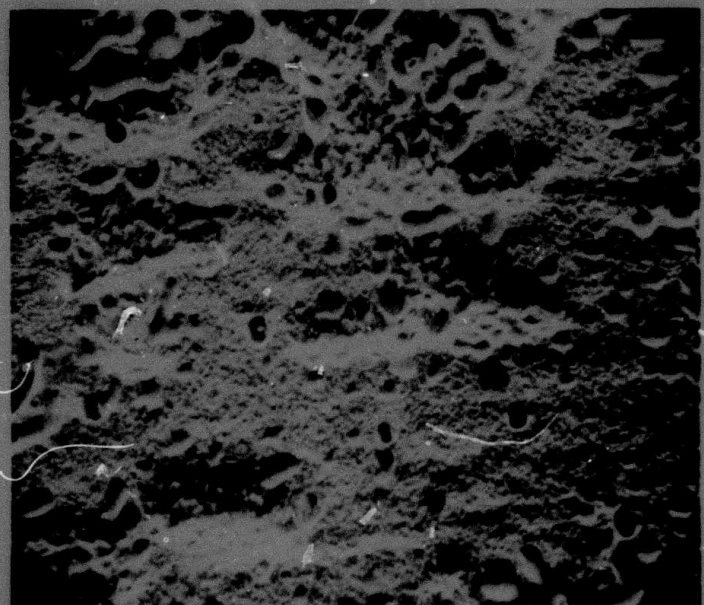


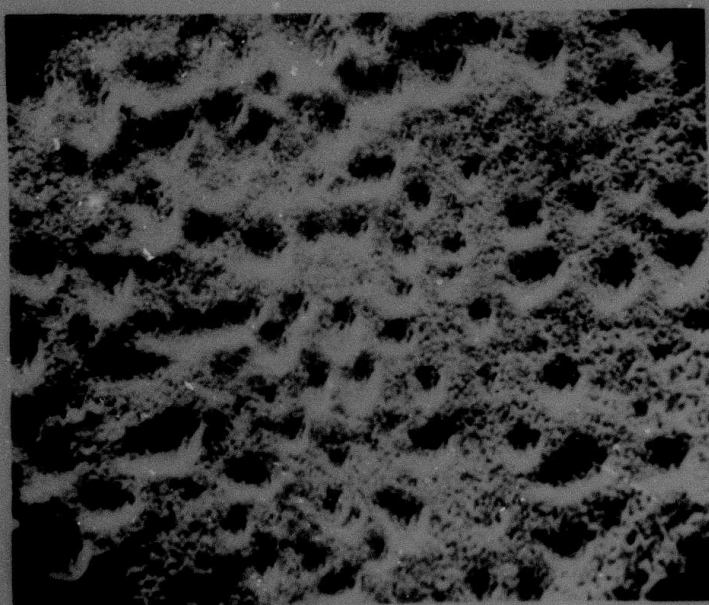
Figure 30 (continued).

The assumption of higher intrinsic nickel diffusivities is not without basis. Janssen and Reick<sup>(26)</sup> studied the behavior of numerous Ni-Al diffusion couples. Experiments with "inert" tungsten markers demonstrated a pronounced Kirkendall effect. The original interface of  $\text{Ni}_3\text{Al}$ -Ni diffusion couples was found at the boundary of the diffusion zone and pure nickel. Porosity was observed in pure nickel after the diffusion anneal. These results indicated that  $D_{\text{Al}}/D_{\text{Ni}}$  was approximately zero. The oxidation process which results in nickel enrichment and aluminum depletion in the  $\text{Ni}_3\text{Al}$  matrix is analogous to a  $\text{Ni}_3\text{Al}$ -Ni diffusion couple with one exception. The area enriched in nickel does not have semi-infinite slab geometry. Consequently, the excess vacancies will condense at or near the free surface and not in the external  $\text{Al}_2\text{O}_3$  layer.

A series of experiments were performed to verify the above model. A sample of the base alloy,  $\text{Ni}_3\text{Al}$ , was aluminized in order to produce an artificial concentration gradient in the surface layers. High-purity aluminum was vapor-deposited on one-half of the sample's side. A diffusion anneal was performed for six hours at 1200°C in ultra-high purity nitrogen. The sample was polished on 1μ diamond paste to remove all diffusion-affected zones except the  $\text{NiAl}(\delta)$  phase. The aluminum concentration at the surface was between 28 and 31%Al. The thickness of the  $\text{NiAl}(\delta)$  phase was approximately 8μ to 11μ. Cyclic oxidation was then performed at 1200°C. The sample was immersed for four hours during each cycle. No spalling was observed on the aluminized portion after two cycles, i.e., cooling after four and eight hours, respectively. The unaluminized area,  $\text{Ni}_3\text{Al}$ , spalled after each cycle. An additional four-hour cycle resulted in severe spalling of the aluminized section. Numerous voids were observed in the substrates of both areas. A valid comparison of the voids formed on each area would require continuous exposure where only  $\text{Al}_2\text{O}_3$  formed: cycling of the  $\text{Ni}_3\text{Al}$  area resulted in composite layer formation. A similar sample was exposed for 12 hours and cooled. The substrates were examined in the SEM. Fig. 31 reveals the nature of void formation in each area of the sample. Very small crystallites of nickel oxide nucleated during cooling. The voids formed on the  $\text{Ni}_3\text{Al}$  section, Fig. 31(a), were irregular in size and distribution. It is clearly demonstrated that



(a)



(b)

Figure 31 Void Formation in the Substrates of Alloys  
Oxidized for 12 Hours at 1200°C. (a)  $\text{Ni}_3\text{Al}$ ,  
500X, (b) Aluminized  $\text{Ni}_3\text{Al}$ , 2000X.

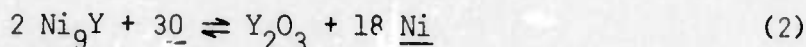
numerous voids penetrate into the substrate. The voids formed in the aluminized substrate were uniform in size and distribution, Fig. 31(b). Penetration into the substrate is not as pronounced as that observed with the unaluminized section. These results are consistent with the proposed model of void formation by the high vacancy flux directed towards the alloy surface.

The vacancy sink concept proposed by Stringer<sup>(24)</sup> can be understood now that the source of excess vacancies has been identified. A particle which has an incoherent boundary with respect to the matrix should be a potent sink for vacancies. The interface between particle and matrix is analogous to a high angle grain boundary. These regions will act as preferred sites for vacancy condensation. The excess vacancy flux to the surface is annihilated by condensation on these interfaces. The condition of vacancy supersaturation within the matrix is never reached, hence, voids cannot be formed near the alloy/oxide interface.

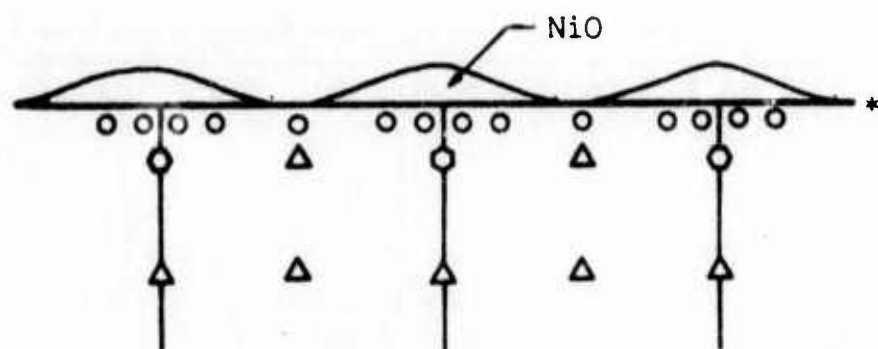
#### 4.3 Oxidation Mechanism of Ni<sub>3</sub>Al-0.5%Y

A mechanism is proposed to account for the differences in the high-temperature scaling behavior and spalling characteristics of the two alloys. Fig. 32 illustrates the development and breakdown of the protective Al<sub>2</sub>O<sub>3</sub> scale on Ni<sub>3</sub>Al-.5%Y at 1200°C.

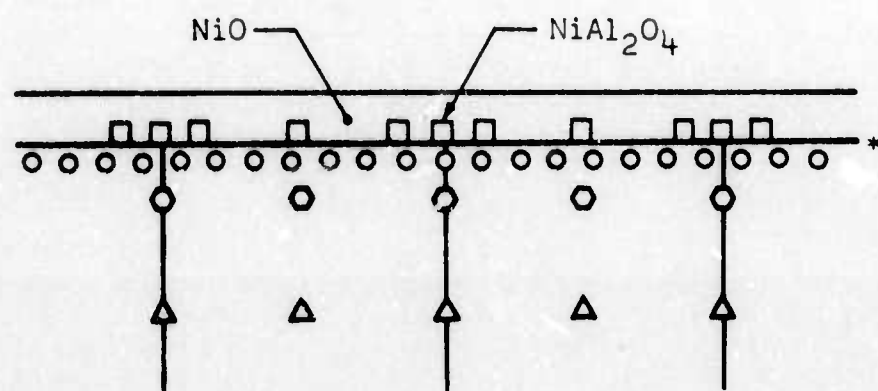
Upon exposure at temperature, no oxides may nucleate until the activity of oxygen in the substrate is raised above the respective oxides' dissociation pressure. In the base alloy, only Al<sub>2</sub>O<sub>3</sub> was formed at 1200°C. The Ni-Y intermetallics and aluminum compete for oxygen. Oxygen diffuses much faster into the alloy grain boundaries than in the matrix. Oxygen in the grain boundaries reacts with Ni<sub>9</sub>Y or Ni<sub>7</sub>Y<sub>2</sub> in the following manner



The nickel freed by this reaction cannot react with dissolved oxygen as the oxygen activity is too low to permit Ni<sub>0</sub>-O-Ni equilibrium. Nickel diffuses rapidly to the surface where it is converted to NiO, Fig. 32(a). The extremely rapid surface diffusion at high temperatures will have a



(a) Time = seconds



(b) Time = tens of seconds

$\triangle$   $\text{Ni}_9\text{Y}$  or  $\text{Ni}_7\text{Y}_2$

$\circ$   $\text{Y}_2\text{O}_3$

$\circ$   $\text{Al}_2\text{O}_3$

$\nabla$   $\text{YAlO}_3$

$\text{G}$   $\text{Y}_3\text{Al}_5\text{O}_12$

\* denotes original interface

Figure 32 Schematic Development of Oxides  
on  $\text{Ni}_3\text{Al}-0.5\% \text{Y}$ .

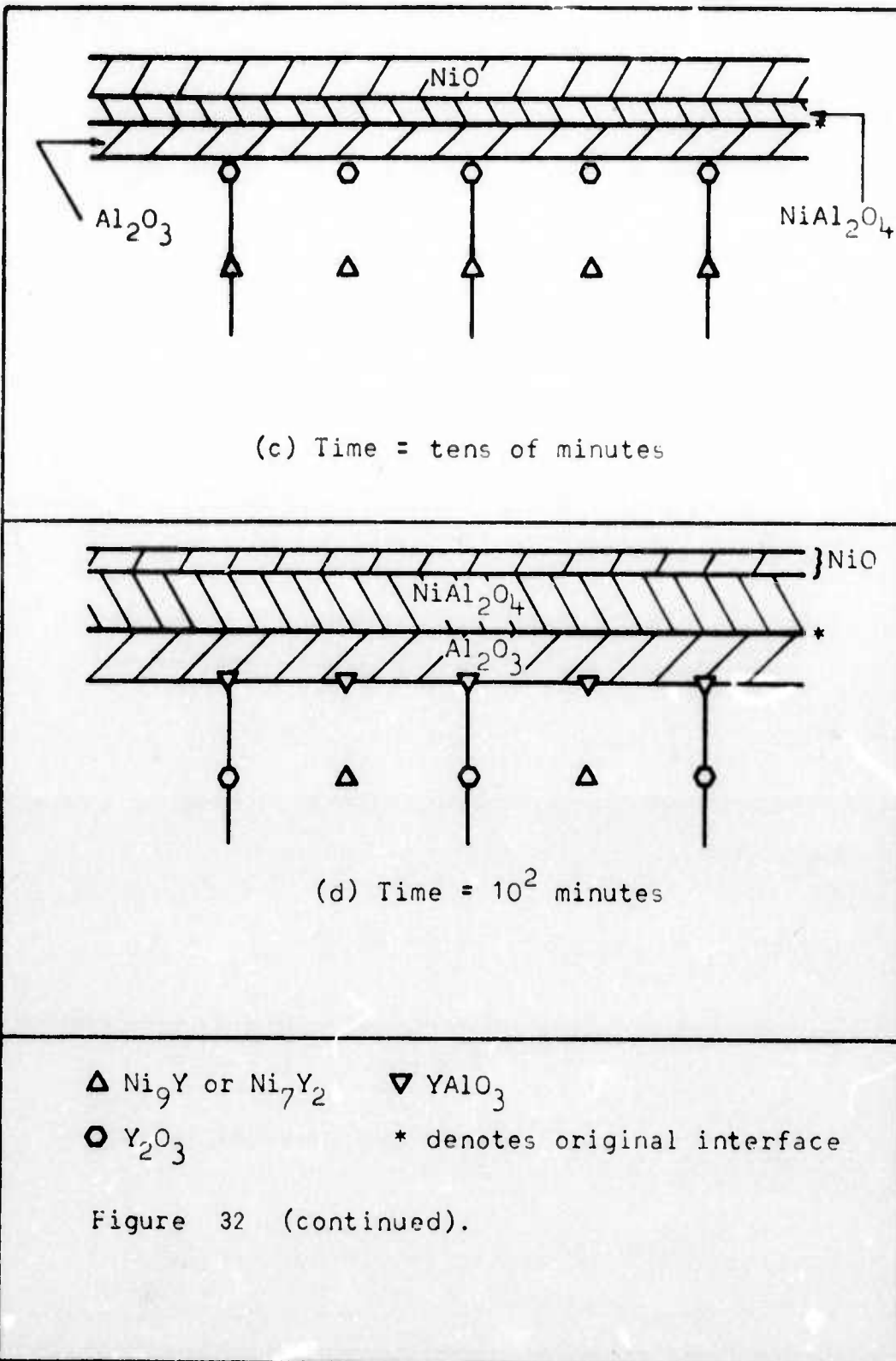
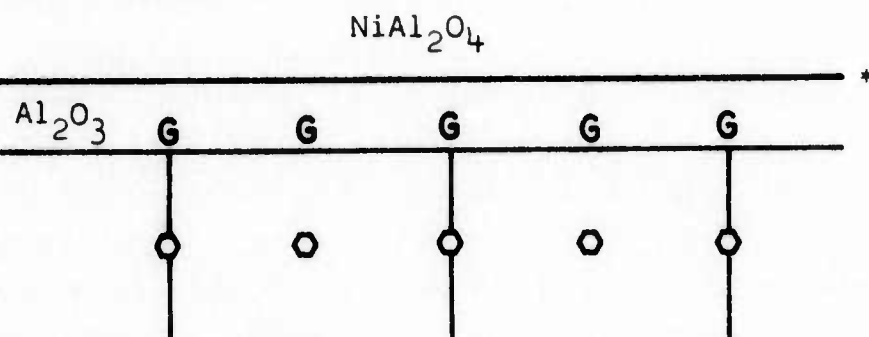
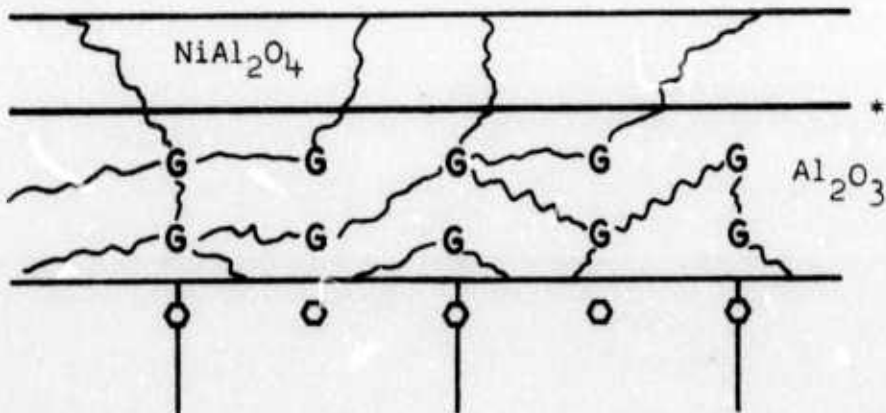


Figure 32 (continued).



(e) Time = Hours



(f) Time =  $10^2$  Hours

**G**  $\text{Y}_3\text{Al}_5\text{O}_{12}$

**O**  $\text{Y}_2\text{O}_3$

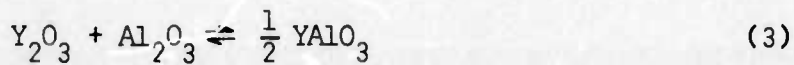
\* denotes original interface

cracks induced by YAG  
during cooling

Figure 32 (continued).

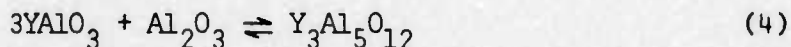
smoothing effect of the NiO accumulation above the grain boundaries. At lower temperatures, more NiO will be concentrated above the grain boundaries (cf. Figs. 16 and 18). Although some discrete nuclei of  $\text{Al}_2\text{O}_3$  have formed, the intermetallic decomposition has upset the local oxygen activity. Further  $\text{Al}_2\text{O}_3$  formation is momentarily retarded until the oxygen activity can be raised. In Fig. 32(b), NiO has coalesced to form a complete layer. A dense zone of  $\text{Al}_2\text{O}_3$  has formed and begun to coalesce. Oxygen is supplied to the alloy by NiO dissociation and oxygen transport through the NiO layer.  $\text{NiAl}_2\text{O}_4$  forms by the solid-state reaction of NiO and  $\text{Al}_2\text{O}_3$ . In Fig. 32(c),  $\text{Al}_2\text{O}_3$  has formed a complete layer. The growth of NiO is effectively halted.  $\text{Al}_2\text{O}_3$  continues to grow by the diffusion of oxygen down grain boundaries. The inward alumina growth has begun to incorporate the  $\text{Y}_2\text{O}_3$  particles. At this time, aluminum depletion and nickel enrichment cause the bulk alloy diffusional processes to produce a high vacancy flux directed at the alloy/ $\text{Al}_2\text{O}_3$  interface. Excess vacancies condense on the incoherent particle boundaries ( $\text{Y}_2\text{O}_3$  or Ni-Y intermetallics.)

During the approach to steady-state conditions, Fig. 32(d), yttria reacts within the  $\text{Al}_2\text{O}_3$  film to produce  $\text{YAlO}_3$  by the reaction



There is a negative volume change associated with the formation of  $\text{YAlO}_3$ . The specific volumes as calculated from the X-ray density are 53.1  $\text{cm}^3/\text{mole}$  ( $\text{Y}_2\text{O}_3$ ) and 30  $\text{cm}^3/\text{mole}$  for  $\text{YAlO}_3$ .<sup>(27)</sup>

The steady-state scaling mode is reached in Fig. 32(e). NiO has been completely converted to spinel. A further transformation has occurred within the alumina layer.  $\text{YAlO}_3$  reacts with alumina to produce the yttrio-garnet,  $\text{Y}_3\text{Al}_5\text{O}_{12}$  (YAG), according to



A positive volume change is associated with YAG formation. The specific volume of YAG is 130.5  $\text{cm}^3/\text{mole}$ .<sup>(27)</sup> The decrease in  $\text{YAlO}_3$  X-ray intensity and corresponding increase in that of YAG indicated that  $\text{YAlO}_3$  was in metastable equilibrium with respect to the YAG. Warshaw and Roy<sup>(28)</sup>

observed this metastable characteristic of  $\text{YAlO}_3$  in their study of the  $\text{Y}_2\text{O}_3\text{-Al}_2\text{O}_3$  phase diagram.

When the alloy is cooled after long exposure times, Fig. 32(f), the YAG particles concentrate the dilational stresses. Cracks initiate next to the YAG particles and propagate throughout the entire composite scale.

## 5. CONCLUSIONS

The addition of yttrium to  $\text{Ni}_3\text{Al}$  did not significantly alter the oxidation kinetics. The steady-state scaling rates of  $\text{Ni}_3\text{Al}$  and  $\text{Ni}_3\text{Al}$  containing 0.5%Y were identical. The presence of yttrium, however, allowed a disproportionate amount of  $\text{NiO}$  to form during the early stages of oxidation. The subsequent solid-state reaction of  $\text{NiO}$  with  $\text{Al}_2\text{O}_3$  resulted in a composite scale consisting of  $\text{NiAl}_2\text{O}_4$  and  $\text{Al}_2\text{O}_3$ .

A quantitative X-ray diffraction technique was used to determine the kinetics of growth of the  $\text{Al}_2\text{O}_3$  layer (one of several oxides formed). The alumina growth followed the parabolic rate law under all conditions studied. The rate-controlling transport process was the enhanced diffusion of oxygen down grain boundaries.

At  $1200^\circ\text{C}$ , only  $\text{Al}_2\text{O}_3$  formed on  $\text{Ni}_3\text{Al}$ ; whereas, a composite scale of alumina and spinel formed on  $\text{Ni}_3\text{Al}-0.5\%$ Y at  $1200^\circ\text{C}$ . A comparison of the steady-state scaling rates and the parabolic growth kinetics of  $\text{Al}_2\text{O}_3$  indicated that alumina was considerably more protective than  $\text{NiAl}_2\text{O}_4$ .

Scale adherence was greatly enhanced for short-times on the alloy containing yttrium. At longer times, however, adherence was lost. Yttrium was originally present in the matrix as nickel-rich intermetallics.  $\text{Y}_2\text{O}_3$  was formed by the reaction of Ni-Y intermetallics and dissolved oxygen. The subsequent incorporation of  $\text{Y}_2\text{O}_3$  into the growing  $\text{Al}_2\text{O}_3$  layer was followed by the formation of  $\text{Y}_3\text{Al}_5\text{O}_{12}$  (yttrium-aluminum garnet). The large YAG particles concentrated the stresses developed during cooling, and spalling was observed.

The cause of spallation from the base alloy,  $\text{Ni}_3\text{Al}$ , was the formation of numerous voids at the alloy/oxide interface. Voids were not observed in the substrates of the alloy containing yttrium. The short-time increase in scale adherence on  $\text{Ni}_3\text{Al}-0.5\%$ Y was attributed to the absence of these

voids. The mechanism of enhanced scale adherence was associated with a vacancy sink model. The previously reported mechanisms, i.e., "key-on" effect,  $YAlO_3$  or  $Y_2O_3$  layer formation, and increased  $Al_2O_3$  plasticity, are not valid. The source of excess vacancies required to form voids at the alloy/oxide interface was identified as that resulting from a "Kirkendall" effect associated with the selective oxidation of aluminum. The rapid diffusion of Ni into the matrix requires a counter-current vacancy flux directed towards the alloy/oxide interface. The vacancies accumulate near or at the substrate interface. When the matrix saturation level is exceeded, the vacancies coalesce and condense as voids. The yttrium-rich particles in the matrix dilute the vacancy flux by providing vacancy sinks.

The sink mechanism appeared to be independent of the chemical nature of the particle. It was suggested that the site of vacancy annihilation was the incoherent boundary between the particle and matrix, and not the particle itself.

## REFERENCES

1. Hessenbruck, W. Metallen und Legierungen für Hohle Temperaturen, Teil I, J. Springer, Berlin, 1940, pp. 31-37.
2. Douglass, D. L. and J. S. Armijo. "The Effect of Silicon and Manganese on the Oxidation Mechanism of Ni-20Cr," Oxidation of Metals, 2 (1970) 207-231.
3. Douglass, D. L. and J. S. Armijo. "The Influence of Manganese and Silicon on the Oxidation Behavior of Co-20Cr," Oxidation of Metals, 3 (1971) 185-202.
4. Tien, J. K. and F. S. Pettit. "Mechanism of Oxide Adherence on Fe-25Cr-4Al (Y or Sc) Alloys," Metallurgical Transactions, 3 (1972) 1537-1599.
5. Oishi, Y. and W. D. Kingery. "Self-Diffusion of Oxygen in Single-Crystal and Polycrystalline Aluminum Oxide," J. Chemical Physics, 33 (1960) 480-486.
6. Paladino, A. E. and W. D. Kingery. "Aluminum Ion Diffusion in Aluminum Oxide," J. Chemical Physics, 37 (1962) 957-962.
7. Paladino, A. E. and R. L. Coble. "Effect of Grain Boundaries on Diffusional-Controlled Processes in Aluminum Oxide," J. American Ceramic Society, 46 (1963) 133-136.
8. Coble, R. L. and Y. H. Guerard. "Creep of Polycrystalline Aluminum Oxide," J. American Ceramic Society, 46 (1963) 353-354.
9. Warshaw, S. I. and F. H. Norton. "Deformation Behavior of Polycrystalline Aluminum Oxide," J. American Ceramic Society, 45 (1962) 479-486.
10. Passmore, E. M. and T. Vasilos. "Creep of Dense, Pure Fine-Grained Aluminum Oxide," J. American Ceramic Society, 49 (1966) 166-168.
11. Wood, G. C. and B. Chattopadhyay. "Transient Oxidation of Ni-Base Alloys," Corrosion Science, 10 (1970) 471-480.
12. Pettit, F. S. "Oxidation Mechanisms for Nickel-Aluminum Alloys at Temperatures Between 900°C and 1300°C," Trans. AIME, 239 (1967) 1296-1305.

13. Wood, G. C. and F. H. Stott. "Establishment and Breakdown of  $\alpha$ - $\text{Al}_2\text{O}_3$  Scales on Ni-Al Alloys at High Temperatures," *British Corrosion Journal*, 6 (1971) 247-256.
14. Fischmeister, H. "Mechanism and Kinetic Effects of Oxide Growth, Part I: Whiskers," *Mémoires Scientifiques Revue Métallurgie*, 62 (1965) 211-215.
15. Gulbransen, E. A. "Model of Oxidation Processes Occurring in Oxide Whiskers and Platelets on Iron at 400°C to 500°C," *Mémoires Scientifiques Revue Métallurgie*, 62 (1965) 254-260.
16. Douglass, D. L. "The Role of Oxide Plasticity on the Oxidation Behavior of Metals: a Review," *Oxidation of Metals*, 1 (1969) 127-142.
17. Battelle Memorial Institute. Engineering Properties of Selected Ceramic Materials, American Ceramic Society, Columbus, Ohio, 1966.
18. Francis, J. M. and W. H. Whitlow. "The Effect of Yttrium on the High-Temperature Oxidation Resistance of Some Fe-Cr Base Alloys in Carbon Dioxide," *Corrosion Science*, 5 (1965) 701-710.
19. Francis, J. M. and J. A. Jutson. "High Temperature Oxidation of an Fe-Cr-Al-Y Alloy in  $\text{CO}_2$ ," *Corrosion Science*, 8 (1968) 445-449.
20. Wood, G. C. "Fundamental Factors Determining the Mode of Scaling of Heat-Resistant Alloys," *Werkstoffe und Korrosion*, 22 (1971) 491-503.
21. Kvernes, I. and P. Kofstad. "Studies on the Behavior of Nickel-Base Superalloys at High Temperatures," Air Force Materials Laboratory, Wright-Patterson Air Force Base, Dayton, Ohio, Technical Report AFML-TR-70-103, 1970.
22. Antill, J. E. and K. A. Peakall. "Influence of an Alloy Addition of Yttrium on the Oxidation Behavior of an Austenitic and a Ferritic Steel in Carbon Dioxide," *J. Iron Steel Institute*, 205 (1967) 1136-1142.
23. Radford, K. C. and P. L. Pratt. "The Mechanical Properties of Impurity-doped Alumina Single Crystals," *Proc. British Ceramic Society*, 15 (1970) 182-202.
24. Stringer, J. "The Effect of Alloying on Oxidation: Quantitative Treatments," *Metallurgical Reviews*, 11 (1966) 113-128.

## REFERENCES

1. Hessenbruck, W. Metallen und Legierungen für Hohe Temperaturen, Teil I, J. Springer, Berlin, 1940, pp. 31-37.
2. Douglass, D. L. and J. S. Armijo. "The Effect of Silicon and Manganese on the Oxidation Mechanism of Ni-20Cr," Oxidation of Metals, 2 (1970) 207-231.
3. Douglass, D. L. and J. S. Armijo. "The Influence of Manganese and Silicon on the Oxidation Behavior of Co-20Cr," Oxidation of Metals, 3 (1971) 185-202.
4. Tien, J. K. and F. S. Pettit. "Mechanism of Oxide Adherence on Fe-25Cr-4Al (Y or Sc) Alloys," Metallurgical Transactions, 3 (1972) 1587-1599.
5. Oishi, Y. and W. D. Kingery. "Self-Diffusion of Oxygen in Single-Crystal and Polycrystalline Aluminum Oxide," J. Chemical Physics, 33 (1960) 480-486.
6. Paladino, A. E. and W. D. Kingery. "Aluminum Ion Diffusion in Aluminum Oxide," J. Chemical Physics, 37 (1962) 957-962.
7. Paladino, A. E. and R. L. Coble. "Effect of Grain Boundaries on Diffusional-Controlled Processes in Aluminum Oxide," J. American Ceramic Society, 46 (1963) 133-136.
8. Coble, R. L. and Y. H. Guerard. "Creep of Polycrystalline Aluminum Oxide," J. American Ceramic Society, 46 (1963) 353-354.
9. Warshaw, S. I. and F. H. Norton. "Deformation Behavior of Polycrystalline Aluminum Oxide," J. American Ceramic Society, 45 (1962) 479-486.
10. Passmore, E. M. and T. Vasilos. "Creep of Dense, Pure Fine-Grained Aluminum Oxide," J. American Ceramic Society, 49 (1966) 166-168.
11. Wood, G. C. and B. Chattopadhyay. "Transient Oxidation of Ni-Base Alloys," Corrosion Science, 10 (1970) 471-480.
12. Pettit, F. S. "Oxidation Mechanisms for Nickel-Aluminum Alloys at Temperatures Between 900°C and 1300°C," Trans. AIME, 239 (1967) 1296-1305.

25. Kuhlmann-Wilsdorf, D., R. Maddin and H. G. Wilsdorf. "Point Defect Hardening in Face-Centered Cubic Metals," Strengthening Mechanisms in Solids, American Society for Metals, Metals Park, Ohio, (1962) 137-178.
26. Janssen, M. M. and G. D. Rieck. "Reaction Diffusion and Kirkendall-Effect in the Nickel-Aluminum System," Trans. AIME, 239 (1967) 1372-1385.
27. Wyckoff, R. W. G. Crystal Structures, Vols. 2 and 3, 2nd Edition, Interscience, New York, 1964, p. 5 395 (Vol. 2), pp. 222-225 (Vol. 3).
28. Marshaw, I. and R. Roy. "Stable and Metastable Equilibrium in the Systems:  $Y_2O_3$ - $Al_2O_3$  and  $Gd_2O_3$ - $Fe_2O_3$ ," J. American Ceramic Society, 42 (1959) 434-438.
29. Warren, B. E. X-Ray Diffraction, Addison-Wesley, Reading, Massachusetts, 1969, pp. 1-66.
30. Wagner, C.N.J. "Analysis of the Broadening and Changes in Position of Peaks in an X-Ray Power Pattern," Local Atomic Arrangements Studied by X-Ray Diffraction, Chicago, February 1965, Gordon and Breach, AIME, New York, 1966, Vol. 36, pp. 219-269.
31. Whittemore, Jr., O. J. and N. N. Ault. "Thermal Expansion of Various Ceramic Materials to 1500°C," J. American Ceramic Society, 39 (1956) 443-444.
32. Gupta, T. K. and J. Valentich. "Thermal Expansion of Yttrium Aluminum Garnet," J. American Ceramic Society, 54 (1971) 355-356.
33. Taylor, A. and R. W. Floyd. "The Constitution of Nickel-Rich Alloys of the Nickel-Titanium-Aluminum System," J. Institute of Metals, 81 (1952) 25-32.

## APPENDIX

The following method was used to calculate oxide thicknesses from X-ray intensity measurements:

Fig. 33 illustrates the sample geometry used in the diffractometer measurements. An incident X-ray beam strikes the surface of a sample having flat-plate geometry. The angle of incidence is at the Bragg angle,  $\theta_B$ , defined by Bragg's law as

$$\frac{2 \sin \theta_B}{\lambda} = \frac{1}{d_{hkl}} \quad (5)$$

where  $\lambda$  = wavelength of incident radiation

$d_{hkl}$  = interplanar spacing of diffracting planes having Miller indices  $h$ ,  $k$ , and  $l$ .

The diffracted intensity by a layer of length  $l$ , and thickness  $dx$ , located a distance  $x$  below the surface will be attenuated over the distance  $\overline{BC}$ . The incident beam is similarly attenuated over the path length  $\overline{AB}$ . Let  $\alpha$  equal the volume fraction of particles having the correct orientation for diffraction (the number of particles varies with preferred orientation), and let  $\beta$  be the fraction of incident power which is diffracted by the atoms per unit volume. Porosity will affect the magnitude of  $\beta$ . The differential of the diffracted power measured outside the sample may be expressed by<sup>(29)</sup>

$$dI_d = I_0 \alpha \beta l \exp[-\mu(\overline{AB} + \overline{BC})] dx \quad (6)$$

where  $I_0$  = power of incident X-ray beam

$\mu$  = linear absorption coefficient.

From the flat-plate geometry, it is seen that

$$l = \frac{1}{\sin \theta_B}, \quad \overline{AB} = \overline{BC} = \frac{x}{\sin \theta_B} \quad (7)$$

Substitution of Eq. (7) into Eq. (6) yields the following:

Preceding page blank

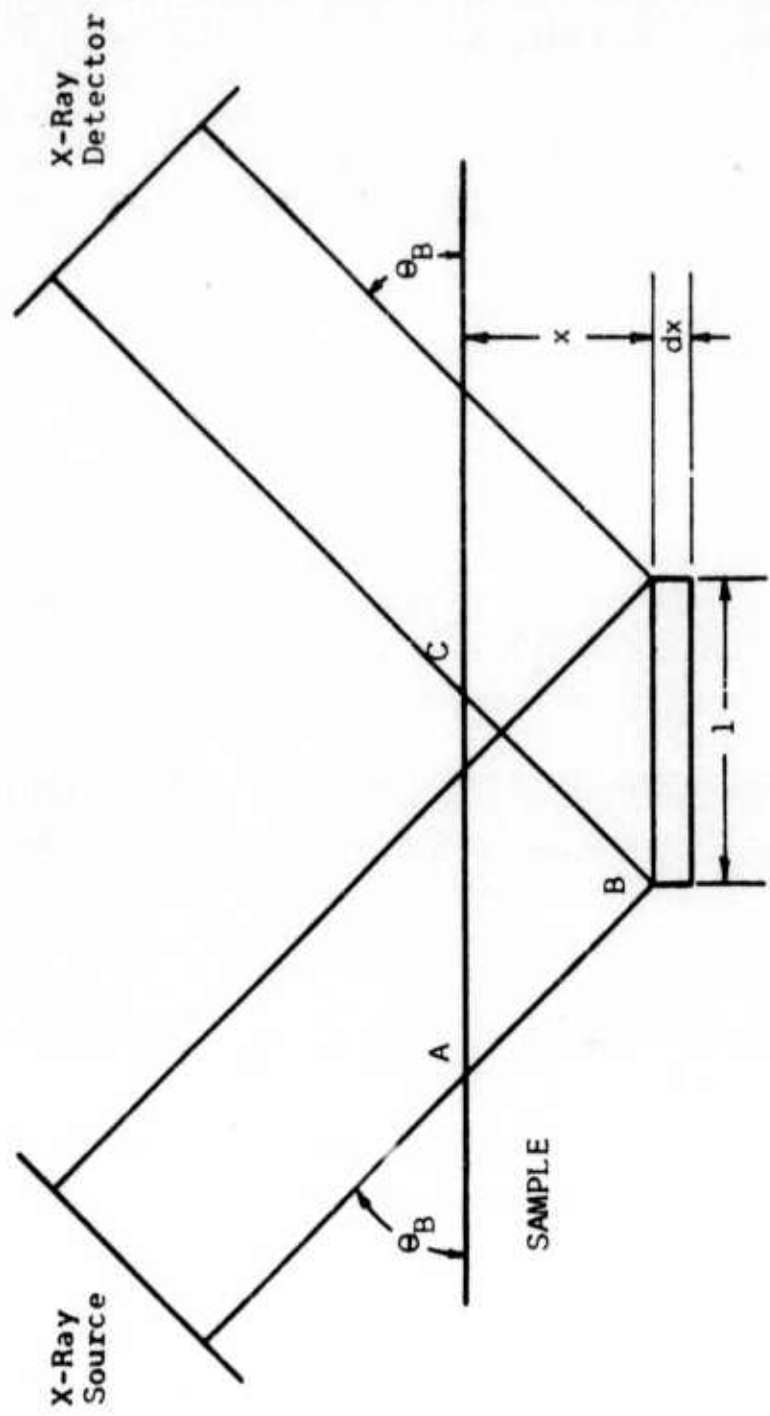


Figure 33 X-ray Diffractometer Sample Geometry.

$$dI_d = I_o \frac{\alpha\beta}{\sin \theta_B} \exp\left(-\frac{2\mu}{\sin \theta_B}\right) dx \quad (8)$$

Integration of Eq. (8) gives the diffracted intensity of a layer having thickness  $x$  as

$$I_d(x) = I_o \frac{(\alpha\beta)_x}{2\mu} \left(1 - e^{-\frac{2\mu x}{\sin \theta_B}}\right) \quad (9)$$

The diffracted intensity of a layer having "infinite" thickness is

$$I_d(\infty) = I_o \frac{(\alpha\beta)_\infty}{2\mu} \quad (10)$$

The ratio of these intensities may be used to calculate the thickness of a finite layer. Define this ratio as  $G(x)$ , given by

$$G(x) = \frac{I_d(x)}{I_d(\infty)} = \frac{(\alpha\beta)_x}{(\alpha\beta)_\infty} \left(1 - e^{-\frac{2\mu x}{\sin \theta_B}}\right) \quad (11)$$

The subscripts  $x$  and  $\infty$  are used on the  $\alpha\beta$  product as the orientation and density of the thermally grown oxide film ( $x$ ) may differ from the standard which has an effective infinite thickness ( $\infty$ ). Methods of correction will be discussed later.

The normalized integrated intensities of the standard and oxide film may differ due to particle size and strain-broadening effects. <sup>(30)</sup>

An integral breadth is defined as

$$B(2\theta) = \frac{\int_{2\theta_1}^{2\theta_2} I_d(2\theta) d(2\theta)}{I_p^{\text{Max}}(2\theta_B)} \quad (12)$$

where  $2\theta_1$  and  $2\theta_2$  are the diffractometer angles at which the "tails" of the diffraction peak are no longer distinguishable from the background intensity;  $I_p^{\text{Max}}(2\theta_B)$  is the maximum intensity recorded.

If the integral breadths of oxide film and standard are similar, i.e.,

$$B(2\theta)_x = B(2\theta)_{\infty} \quad (13)$$

then only peak intensities need be used.

The formation of composite layers requires additional corrections. If an alumina layer is covered by NiO, the intensity ratio function  $G(x)$  is corrected by

$$G(x)_{Al_2O_3} = \left[ \frac{(\alpha\beta)_x}{(\alpha\beta)_{\infty}} \right]_{Al_2O_3} \frac{\left( 1 - \frac{2\mu x}{\sin \theta_B} \right)_{Al_2O_3}}{\frac{1 - e^{-2(\mu x)_{NiO}}}{e^{-\frac{2\mu x}{\sin \theta_B}}}} \quad (14)$$

where  $(\mu x)_{NiO}$  refers to the absorption coefficient and thickness of NiO thickness of NiO.

Alumina consumed by the spinel reaction is calculated by analyzing the decrease in NiO intensity. This effect is important only at the higher temperatures.

Eq. (11) may be simplified for the case of thin,  $< 2\mu$ , oxides by using

$$1 - e^{-y} \approx y, \quad y \ll 1 \quad (15)$$

The simplified form of Eq. (11) is

$$G(x) = \frac{(\alpha\beta)_x}{(\alpha\beta)_{\infty}} \frac{2\mu}{\sin \theta_B} x \quad (16)$$

At constant diffraction angle, let

$$G(x) = \phi x \quad (17)$$

where

$$\phi = \frac{(\alpha\beta)_x}{(\alpha\beta)_{\infty}} \frac{2\mu}{\sin \theta_B} \quad (18)$$

A comparison of the square of Eq. (17) with the parabolic rate law,  $x^2 = Kpt$ , yields the following result

$$G^2(x) = \phi^2 Kpt \quad (19)$$

A log-log plot of  $G(x)$  vs.  $t$  should give a slope of one-half if the parabolic rate law is obeyed. Alternately, a plot of  $G^2(x)$  vs.  $t$  will give a straight line whose slope is  $\phi^2 K_p$  if parabolic kinetics prevail.

The factor  $\alpha$  for both oxide film and standard is evaluated by comparing the measured integrated intensity (peak/height was used since the breadth of all peaks remained unchanged) with the calculated or theoretical integrated intensity for a random powder sample. Warren<sup>(29)</sup> has outlined the detailed procedure for this calculation. Pronounced orientation effects are greatly reduced by averaging several diffraction peaks of both oxide and standard.

A correction for density is made through the factor  $\beta$  if the oxide scales or standards show porosity. Dense, >99%, bulk samples were used for the standards. Scanning electron micrographs indicated that the thermally grown oxides were comparable in density to the standards.

A self-consistent method was used to check the calculated composite layer thicknesses. The measured attenuation of the substrate reflections (always present) was compared to that expected from the calculated composite layer thicknesses.

The substrate attenuation is given by

$$\frac{I_D(t)}{I_D(t=0)} = \exp\left[-\frac{2}{\sin \theta_s} \sum_i \left(\frac{\mu}{\rho}\right)_i \rho_i t_i\right] \quad (20)$$

where  $I_D(t)$  = substrate intensity at time  $t$

$I_D(t=0)$  = substrate intensity prior to oxidation

$\theta_s$  = Bragg angle for the substrate reflection

$\left(\frac{\mu}{\rho}\right)_i$  = mass absorption coefficient of the  $i^{\text{th}}$  layer

$\rho_i$  = density of the  $i^{\text{th}}$  layer

$t_i$  = thickness of the  $i^{\text{th}}$  layer.

The substrate attenuation calculated by Eq. (20) agreed within 15% to that measured. This agreement was considered very good.